

PATTERNING OF Si SURFACE BY MEDIUM ENERGY ION BEAMS

By
SANDEEP KUMAR GARG
PHYS07200804004

INSTITUTE OF PHYSICS, BHUBANESWAR



A thesis submitted to the

Board of studies in physical sciences

In partial fulfillment of requirements

For the degree of

DOCTOR OF PHILOSOPHY

of

HOMI BHABHA NATIONAL INSTITUTE



November, 2014

Homi Bhabha National Institute

Recommendations of the Viva Voce Board

As members of the Viva Voce Board, we certify that we have read the dissertation prepared by Mr. Sandeep Kumar Garg, entitled "Patterning of Si surface by medium energy ion beams", and recommend that it may be accepted as fulfilling the dissertation requirement for the Degree of Doctor of Philosophy.

Date: 15/11/2014



Chairman - Prof. A.M. Jayannavar



Date: 15/11/2014

Guide / Convener - Prof. T. Som



Date: 15/11/2014

Member 1 - Prof. D. Datta



Date: 15/11/2014

Member 2 - Prof. S. Varma



Date: 15/11/2014

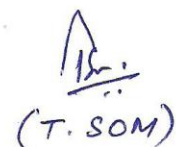
Member 3 - Prof. P.V. Satyam

Final approval and acceptance of this dissertation is contingent upon the candidate's submission of the final copies of the dissertation to HBNI.

I hereby certify that I have read this dissertation prepared under my direction and recommend that it may be accepted as fulfilling the dissertation requirement.

Date: 15-11-2014

Place: IOP, BHUBANESWAR


(T. SOM)

STATEMENT BY AUTHOR

This dissertation has been submitted in partial fulfillment of requirements for an advanced degree at Homi Bhabha National Institute (HBNI) and is deposited in the Library to be made available to borrowers under rules of the HBNI.

Brief quotations from this dissertation are allowable without special permission, provided that accurate acknowledgement of source is made. Requests for permission for extended quotation from or reproduction of this manuscript in whole or in part may be granted by the Competent Authority of HBNI when in his or her judgment the proposed use of the material is in the interests of scholarship. In all other instances, however, permission must be obtained from the author.

Sandeep Kumar Garg

DECLARATION

I, hereby declare that the investigation presented in the thesis has been carried out by me. The work is original and has not been submitted earlier as a whole or in part for a degree / diploma at this or any other Institution / University.

Sandeep Kumar Garg

To my mother

Acknowledgments

I take this opportunity to express my sincere gratitude to my advisor, Prof. T. Som, for his constant encouragement, support, and invaluable guidance throughout my research period. Prof. T. Som taught me the intuitive way of looking into the problem, perfectionism in work. It is a fact that without his help this dissertation would have not been possible. I sincerely thank him for his enormous time he had with me for my research and extend my sincere thank him and his family for taking care of me during the entire work of this thesis.

I am very grateful some of very senior members, Dr. D. Kanjilal, IUAC, New Delhi, Prof. S.R. Bhattacharya, SINP, Kolkata, and Prof. R. Cuerno, Universidad Carlos III de Madrid, Spain, for allowing me to work with them. I must thank for their hospitality, during my research stay at their home institutes. I would like to express my high regards for Dr. D. Kanjilal who always encouraged me, anywhere I got a chance to meet him. And whenever I required the beam time in IUAC to complete this dissertation, he made it possible.

I would like to thank Prof. S. Rath, DU, Delhi, Dr. S.R. Tripathy, IMRE, Singapore, Dr. Jay Ghatak, JNCASR, Bengaluru, Dr. S. Chatterjee, IMMT, Bhubaneswar, and Dr. P.K. Sahoo, NISER, Bhubaneswar for extending their lab facilities and precious time towards characterization of my research samples and relevant discussion.

I take the opportunity to thank my senior group members Dr. V. Venugopal, SIT, Tumkur, Dr. O.P Sinha, Amity University, Noida, and Dr. D.P. Datta for our valuable discussion and providing me a chance to work with them. My special thanks to Dr. D.P. Datta for spending long hours with me and for his constant effort towards finalizing this thesis. I have spent many enjoyable hours working with my fellow group members. I thank them all, both past and present, including Dr. J.K. Tripathi, Dr. S. Chnadramoham, Dr. S. Nandy, Dr. S. Hazara, Dr. A.K. Mahapatra, Mr. T. Basu, Mr. Mohit Kumar, and Mr. Jyoti Ranjan Mohanty. I acknowledge Mr. Lingraj for his dedicated service, given to the SUNAG lab.

I thank all my teachers who taught me in pre-doctoral course and all the experimental condensed matter group faculties of IOP, Bhubaneswar for their generous support. Special thanks to Prof. P.V. Satyam for his guidance during my pre-doctoral project in his guidance and Prof. B.R. Sheker, for allowing me to work with him. I also thank to scientific staff of IOP, especially Mr. S.K. Choudhury, Mr. A.K. Behera, and Dr. S.N. Sarangi, for making themselves available wherever their expertise was needed.

I gratefully acknowledge the LEIBF staff of IUAC, New Delhi, especially Dr. P. Kumar, and Mr. U.K. Rao who were available 24×7 for smoothly running the facility and had a direct interaction with me. I thank to Mr. Sunil Ojha for his generous support during my research problem.

It is the best time to remember all my friends at IOP, outside IOP, and from my personal domain whose constant support always remained with me. Some of them advised me, some stood with me, and few of them criticized me for a better cause in my both academic and personal lives. List is long but you all are the persons who kept me always cheerful.

I am indebted to the former directors: Prof. Y.P. Viyogi, Prof. A. Khare, Prof. A.M. Jayannavar, Prof. A.M. Srivastava, and the present director, Prof. S. Panda, Dean HBNI at IOP, Prof. A.M. Srivastava, members of my Doctoral committee: Prof. P.V. Satyam, Prof. S. Varma, and Prof. A.M. Jayannavar, and all the members (academic and non-academic) for their timely help, cooperation, and support whenever needed.

Finally, my sincere gratitude to my mother, wife, brother, and sister for their love, patience, unwavering support, and silent acceptance of my long absence from home. Not being physically but you all were always around me. You all are the reasons for where I am today.

Date: 15 Nov. 2014

Place: Bhubaneswar

Sandeep K. Garg

List of Publications

Published In Journal

- *1. Study of Initial wavelength selection of ripple formation at Si surface induced by medium energy Ar⁺ ions by **S.K. Garg**, D.P. Datta, R. Cuerno, D. Kanjilal, and T. Som, Journal of Physics: Condensed Matter (Communicated).
- *2. Medium energy Ar⁺-ion induced ripple formation: Role of ion energy in pattern formation by **S.K. Garg**, D.P. Datta, J. Ghatak, S.R. Tripathy, D. Kanjilal, and T. Som, Applied Surface Science, 317 (2014) 476.
- 3. 60 keV Ar⁺-ion induced modification of microstructural, compositional, and vibrational properties of InSb by D.P. Datta, **S.K. Garg**, B. Satpati, P.K. Sahoo, A. Kanjilal, S. Dhara, D. Kanjilal, and T. Som, Journal of Applied Physics, 116 (2014) 143502
- *4. 60 keV Ar⁺-ion induced pattern formation on Si surface: Role of sputter erosion and atomic redistribution by **S.K. Garg**, D.P. Datta, M. Kumar, D. Kanjilal, and T. Som, Applied Surface Science, 310 (2014) 147.
- 5. Temporal evolution of nanoporous layer in off-normally ion irradiated GaSb by D.P. Datta, A. Kanjilal, **S.K. Garg**, P.K. Sahoo, D. Kanjilal, and T. Som, Journal of Applied Physics, 115 (2014) 123515.
- 6. Evolution of porous network in GaSb under normally incident 60 keV Ar⁺ -ion irradiation by D.P. Datta, A. Kanjilal, **S.K. Garg**, P.K.Sahoo, B. Satpati, D. Kanjilal, and T. Som, Applied Surface Science, 310 (2014) 189.
- *7. Evolution of ripple morphology on Si(100) by 60 keV Ar ions by **S.K. Garg**, V. Venugopal, T. Basu, O.P. Sinha, S. Rath, D. Kanjilal, and T. Som, Applied Surface Science, 258 (2012) 4135.

8. Ion erosion induced nanostructured semiconductor surfaces by V. Venugopal, T. Basu, **S. Garg**, J.K. Tripathi, S. Chandramohan, P. Das, T.K. Chini, S.R. Bhattacharyya, D. Kanjilal, and T. Som, International Journal of Nanotechnology, 9-12 (2012) 1007.

9. Nanostructures on GaAs surfaces due to 60 keV Ar⁺-ion beam sputtering, V. Venugopal, **S.K. Garg**, T. Basu, O.P. Sinha, D. Kanjilal, S.R. Bhattacharyya, and T. Som, Applied Surface Science 258 (2012) 4144.

10. Investigation on structural, optical, morphological and electrical properties of thermally deposited lead selenide (PbSe) nanocrystalline thin films by T.S. Shyju, S. Anandhi, R. Sivakumar, **S.K. Garg**, R. Gopalakrishnan, J. Cryst. Growth 353 (2012) 47.

Conference Proceedings

1. Evolution of Surface Topography on GaAs(100) and GaAs(111) at Normal and Oblique Incidence of Ar⁺-Ions by V. Venugopal, P. Das, T. Basu, **S. Garg**, S. Majumdar, S.N. Sarangi, S.R. Bhattacharyya, T.K. Chini, and T. Som, AIP Conf. Proc. 1276 (2010) 50.

To be communicated

*1. Statistical analysis of ripple morphology on Si surfaces due to 60 keV Ar⁺-ions by **S.K. Garg**, D.P. Datta, V. Venugopal, T. Basu, M. Kumar, D. Kanjilal, and T. Som, Physical Review E.

*2. Wettability of 60 keV Ar⁺-ion irradiated rippled Si surfaces by **S.K. Garg**, D.P. Datta, T. Basu, I. Thakur, S.R. Tripathy, D. Kanjilal, and T. Som, Applied Surface Science.

(*) indicates papers on which this thesis is based.

Synopsis

Modern technology crucially depends upon development of materials with precisely controlled properties. In the context of synthesis and modification of materials, ion bombardment is a versatile, efficient, and widely used technique — both in fundamental research as well as in technological applications. It is a non-equilibrium processing route which allows deposition of energy in a target material, leading to modification of the target microstructure (i.e., radiation damage), introduction of foreign atoms in the target beyond thermodynamical limit (i.e. ion implantation), and also removal of materials from the target surface (sputtering) [1]. Such interactions of energetic ions with a target material not only result in modification of a range of materials properties but also lead to spontaneous formation of periodic nanoscale patterns on a target surface, namely one-dimensionally periodic ripples under oblique ion incidence [2] and two-dimensionally periodic dot patterns under normal incidence of the ion-beam [3]. Research interest in this self-organized processing of surface nanostructure has been stimulated by promising applications of ripple patterned surfaces as templates for deposition of functional thin films where magnetic or optical anisotropy can be introduced in the films through the morphological anisotropy of the periodically modulated underlying substrates [4,5].

Experimentally, the length scale of the ripple patterns is found to be dependent upon incident ion energy and varies from tens of nanometers in case of low energy (0.5-10 keV) ion irradiation to hundreds of nanometers in case of medium energy (10-100 keV) irradiation. In addition, the pattern evolution is also influenced by angle of incidence of ions, ion-flux, -fluence, as well as particular ion-target composition [6]. Theoretically, ion induced patterning is considered to be an outcome of competing processes, viz. roughening due to curvature dependent sputtering [2] or ion induced mass redistribution [7] and surface smoothing processes due to thermal diffusion [8], ion induced effective diffusion [9], or viscous flow

[10]. Further, a recent model by Castro *et al.* [11] explained surface patterning as a result of ion-induced stress dependent solid flow. In comparison to low energy case [3,12-14], less research efforts were devoted towards medium energy ion induced patterning [15-17] and thus, the understanding of the processes involved is still far from complete. For example, Datta *et al.* [16,18] showed the formation and coarsening of ripple patterns on Si under 30 and 60 keV Ar⁺-ion irradiation. Dependence of pattern formation on angle of ion incidence was also investigated by Datta *et al.* [18] for 30 keV Ar⁺-ion irradiation. However, the experimentally observed absence of pattern formation below 55° angle of incidence could not be explained by invoking curvature dependent sputtering theory. In fact, a systematic investigation on the influence of ion incidence angle on surface patterning, in conjunction with numerical estimation based on the theoretical models, is still lacking in case of medium energy ion irradiation, although this is essential towards identifying the physical mechanisms contributing to ripple formation, as shown in low energy cases. In addition, late stage dynamics of ripple patterns as observed by Chini *et al.* [19] was dominated by ion-beam shadowing, in addition to nonlinear effects. Consequently, the linear and nonlinear evolution of ripples in the medium energy regime, in absence of any coexistent contributing factor like shadowing, is yet to be demonstrated. Likewise, the very early stage of patterning under medium energy ion irradiation has not received any attention either. In fact, the length scale of medium energy ion induced patterns provides a unique experimental platform to correlate the early stage of pattern evolution in the framework of existing theoretical models. Further, in case of medium energy irradiation, the deviation in energy scaling of ripple wavelength, as reported by Biermanns *et al.* [17] from theoretically predicted nature remains unexplained. In addition to morphological aspects, the studies on the structural evolution under medium energy, namely 60 keV Ar⁺-ion irradiation on Si at 60°, revealed formation of an amorphous layer with a periodically modulated amorphous/crystalline (*a/c*) interface, parallel to the

ripple modulations on the top surface [20]. Recently, Kumar *et al.* [21,22] observed similar modulated (*a/c*) interface during 50 and 200 keV Ar-ion irradiation of Si at 60° and proposed that ripple formation starts from the (*a/c*) interface. Systematic structural and compositional analyses on ion-beam fabricated rippled surfaces can thus, provide important information on ripple formation and its temporal evolution in the medium ion energy regime. Moreover, the important question of whether the pattern evolution under medium energy ion irradiation can be understood within the same theoretical framework as applied to explain low energy ion induced pattern formation still remains an open question.

Thus, a systematic study of medium energy ion induced pattern evolution, with particular attention to the features which remains unexplored till now, as mentioned above, is extremely important for a complete understanding of patterning process towards engineering the surface topography for novel technological application(s). In this thesis, we present our experimental investigations on medium energy ion-beam induced morphological evolution of Si surface and related modifications in Si microstructure. In our studies, we have particularly addressed above mentioned important aspects of ion-beam patterning at this energy regime. In parallel to the experimental studies, we have carried out detail numerical estimations based upon current theoretical models of ion-bombarded surface evolutions using simulation packages, viz. SRIM, TRIDYN, and SDTrimSP [23-25]. Our studies reveal in-depth information on ripple pattern evolution in the medium energy regime as described below.

The experimental studies presented in this thesis focus on medium energy ion-beam induced morphological evolution on Si surface and related modification in Si microstructure. For this purpose, 60 keV Ar⁺ and Xe⁺-ion irradiation on crystalline Si wafers were carried out over a wide range of ion-fluence and -angle of incidence. To analyze the surface topography, microstructure, and composition of the targets, atomic force microscopy (AFM), cross-sectional transmission electron microscopy (XTEM), micro-Raman Spectroscopy, Rutherford

backscattering spectrometry (RBS), and energy dispersive X-ray spectrometry (EDS) were employed. Impurity-free implantations were confirmed by X-ray photoelectron spectroscopy (XPS). Parallely, simulations on the ion-solid interaction were performed using SRIM, TRIDYN, and a recently available versatile simulation code SDTrimSP codes. In-depth statistical analysis of surface topography was also carried out by using WSxM, Gwyddion, and SPIP [26-28] in order to determine the optimized conditions for ion-beam patterning. Finally, the wettability of patterned Si surfaces was investigated, which reveals a possible application of the medium energy ion-beam fabricated periodic surfaces.

In our studies we observed the formation of periodic ripple pattern in the angular range $45^\circ \leq \theta \leq 75^\circ$ whereas the Si surface remains stable (i.e. no pattern formation takes place) for $\theta < 45^\circ$. Our study further reveals hitherto unobserved aspects of ion-beam induced pattern evolution in the medium energy regime. In particular, a decreasing trend in the ripple wavelength (with ion fluence) is observed in the initial stage of morphological evolution for 60 keV Ar⁺-ion irradiation on Si where ripple amplitude increases exponentially. This is followed by coarsening of ripple wavelength in the later stage where ripple amplitude remains constant. In order to understand this behavior, we performed statistical analysis of our morphological data and demonstrate a symmetric to asymmetric transition in the ripple shape with increasing ion fluence. Based on this analysis, we could distinguish the linear and nonlinear regimes of pattern evolution in the present case. In addition, this analysis helped us to identify that decreasing ripple wavelength at the initial stage of pattern formation actually belongs to the linear regime. Our numerical calculations, based on the linear stability analysis within a continuum model, on ion bombarded surface evolution show that the initial decrease in the ripple wavelength is related to a change in ion induced surface tension.

We have also constructed a parametric phase diagram to provide an overview of medium energy ion induced pattern formation on Si surface. Through this phase diagram, we have

shown some striking similarities between ripple patterns in low and medium energy regimes and infer that at places similar mechanisms are responsible for pattern formation at both energy regimes. We have also numerically estimated the predictions of current theoretical models for 60 keV Ar⁺-ion irradiation in Si as a function of angle of incidence, where the required parameters are extracted from simulation of ion-solid interaction using the SDTrimSP code. Upon comparing our experimental results (in the linear regime) with our numerical estimations, we have shown that in contrast to the dominance of ion-induced atomic redistribution process in case of both low (as interpreted by Madi *et al.* [29]) and medium (as proposed by Carter and Vishnyakov [15]) energy ion-induced ripple evolution on Si, both curvature dependent sputter erosion and prompt atomic redistribution are operative for medium energy ion-induced ripple evolution.

Upon performing the structural analysis by using micro-Raman spectroscopy of ion irradiated Si samples, we observe a narrow peak at 521 cm⁻¹ and a broad peak at 480 cm⁻¹ to appear in the Raman spectra for all ion fluences which correspond to crystalline and amorphous Si, respectively. In fact, it is observed that the Raman signal corresponding to crystalline-Si increases with increasing incident angle of Ar-ion beam. This is consistent with the angle-dependent projected range of Ar-ions in Si. This indicates the presence of both amorphous- and crystalline-Si layers (within the probing depths of the chosen laser line). XTEM studies also confirm the formation of an amorphous layer with a higher thickness on the front slope of the ripples (facing the incident beam) compared to the back slopes. Further, TEM studies show the formation of bubbles which are populated in the near-surface region and the EDS measurements demonstrate that these bubbles contain argon (or xenon). The presence of argon (or xenon) atoms were also confirmed from RBS studies. Formation of the amorphous layer has been correlated with the nuclear energy loss under oblique ion incidence. Subsequently, we show that experimentally observed scaling of ripple wavelength (λ) with

ion energy complies with theoretical predictions if the nuclear energy loss is considered to be the sole contributing factor behind ripple formation instead of total energy of incident ions.

To further explore the homogeneity and anisotropy of the surface topography as functions of ion fluence and angle of incidence, we performed detail statistical analysis of AFM image of the patterned surfaces by using the SPIP software. Morphological parameters, viz. surface area ratio (*sdr*), texture direction index (*stdi*), texture aspect ratio (*str*), ratio of system correlation length to wavelength (ζ/λ), directional roughness exponents (α_x and α_y), and anisotropy ratio (γ) were calculated as a functions of ion incidence angle and fluence. From the fluence dependent study of these parameters, we find that ripple shapes are most regular for fluence 3×10^{18} ions cm^{-2} and ripples are unidirectional at the fluence of 2×10^{18} ions cm^{-2} . Similarly, from angle dependent studies, we observed that ripple patterns become optimized with increase in angles of ion incidence. We have also found that anisotropy of the rippled surface becomes more prominent as a function of incidence angle compared to ion fluence.

In order to have some possible application of such ripple-patterned Si surfaces, we performed wettability measurements of the Si sample irradiated by Ar^+ at $\theta=60^\circ$, as a function of ion fluence. It is observed that the hydrophilicity of Si surface increases with ion irradiation. Observed results indicates a connection between the wettability of patterned Si with the topography which we explain in light of Wenzel's law [30].

In summary, the thesis presents an extensive study of medium energy ion induced pattern evolution on Si surfaces. Analysis of the experimental observations in the framework of current theoretical models leads to the determination of physical mechanisms contributing to pattern formation in this energy regime. The related micro structural modifications are also investigated and a promising application of the patterning process in controlling the wettability of the surface has been pointed out.

References

1. M. Nastasi, J.W. Mayer, and J.K. Hirvonen, *Ion-solid interactions: Fundamentals and applications*. 1996: Cambridge University Press.
2. R.M. Bradley and J.M.E. Harper, *J. Vac. Sci. Technol. A* 6 (1988) 2390.
3. S. Facsko, T. Dekorsy, C. Koerdts, C. Trappe, H. Kurz, A. Vogt, and H.L. Hartnagel, *Science* 285 (1999) 1551.
4. J. Fassbender, T. Strache, M. Liedke, D. Marko, S. Wintz, K. Lenz, A. Keller, S. Facsko, I. Monch, and J. McCord, *New J. Phys.* 11 (2009) 125002.
5. M. Ranjan, T.W.H. Oates, and S. Facsko in *Nanofabrication by Ion-Beam Sputtering: Fundamentals and Applications*, Eds. T. Som and D. Kanjilal, 2012: Pan Stanford: Singapore, p. 297.
6. M.A. Makeev, R. Cuerno, and A.-L. Barabási, *Nucl. Instrum. Methods Phys. Res. B* 197 (2002) 185.
7. S.A. Norris, M.P. Brenner, and M.J. Aziz, *J. Phys. Condens. Matter* 21 (2009) 224017.
8. W.W. Mullins, *J. Appl. Phys.* 28 (1957) 333.
9. M.A. Makeev and A.-L. Barabási, *Appl. Phys. Lett.* 71 (1997) 2800.
10. C.C. Umbach, R.L. Headrick, and K.-C. Chang, *Phys. Rev. Lett.* 87 (2001) 246104.
11. M. Castro, R. Gago, L. Vázquez, J. Muñoz-García, and R. Cuerno, *Phys. Rev. B* 86 (2012) 214107.
12. C.S. Madi, B. Davidovitch, H.B. George, S.A. Norris, M.P. Brenner, and M.J. Aziz, *Phys. Rev. Lett.* 101 (2008) 246102.
13. T. Basu, J.R. Mohanty, and T. Som, *Appl. Surf. Sci.* 258 (2012) 9944.
14. T. Basu, D. Datta, and T. Som, *Nanoscale Res. Lett.* 8 (2013) 289.
15. G. Carter and V. Vishnyakov, *Phys. Rev. B* 54 (1996) 17647.

16. D.P. Datta and T.K. Chini, Phys. Rev. B 71 (2005) 235308.
17. A. Biermanns, U. Pietsch, J. Grenzer, A. Hanisch, S. Facsko, G. Carbone, and T.H. Metzger, J. Appl. Phys. 104 (2008) 044312.
18. D.P. Datta and T.K. Chini, Phys. Rev. B 76 (2007) 075323.
19. T.K. Chini, D.P. Datta, and S.R. Bhattacharyya, J. Phys.: Condens. Matter 21 (2009) 224004.
20. S. Hazra, T.K. Chini, M.K. Sanyal, J. Grenzer, and U. Pietsch, Phys. Rev. B 70 (2004) 121307.
21. T. Kumar, A. Kumar, D. Agarwal, N. Lalla, and D. Kanjilal, Nanoscale Res. Lett. 8 (2013) 336.
22. T. Kumar, U.B. Singh, M. Kumar, S. Ojha, and D. Kanjilal, Current Applied Physics 14 (2014) 312.
23. J.F. Ziegler, J.P. Biersack, and K. Littmark, *The stopping and Range of Ions in Matter*. 1985, Pergamon, New York. <http://www.srim.org/>
24. W. Möller and W. Eckstein, Nucl. Instrum. Methods Phys. Res. B 2 (1984) 814.
25. W. Eckstein, R. Dohmen, A. Mutzke, and R. Schneider, IPP Report 12 (2007).
26. Nanotec, *WSxM Software*. <http://www.nanotec.es/products/wsxm/>
27. D. Nečas and P. Klapetek, Central European Journal of Physics 10 (2012) 181.
28. A.S. Image Metrology. *SPIP Software*. Available from: www.imagemet.com
29. C.S. Madi, E. Anzenberg, K.F. Ludwig, Jr., and M.J. Aziz, Phys. Rev. Lett. 106 (2011) 066101.
30. R.N. Wenzel, Industrial & Engineering Chemistry 28 (1936) 988.

Table of Contents

Synopsis	x
List of Figures	xxii
<u>1 Introduction</u>	<u>1</u>
1.1 Preamble	1
1.2 Ion-Solid interaction	2
1.2.1 Basics	2
1.2.2 Ion stopping	4
1.2.3 Ion range and straggling	7
1.2.4 Sputtering	8
1.2.5 Numerical simulation of ion-solid interaction	10
1.3 Ion-beam induced pattern formation	11
1.4 Motivation for experimental studies presented in this thesis	13
1.5 Organization of the thesis	16
<u>2 Experimental</u>	<u>22</u>
2.1 Introduction	22
2.2 Ion Implantation	22
2.3 Ion Implanter	23
2.3.1 Low energy ion beam facility (LEIBF) at IUAC	24
2.3.2 Ion source	25

2.3.3 Analyzing-cum-switching magnet	25
2.3.4 Experimental station and accessories	26
2.4 Characterization Technique	26
2.4.1 Atomic force microscopy (AFM)	26
2.4.2 Transmission electron microscopy (TEM)	29
2.4.3 Energy dispersive X-ray spectrometry (EDS)	30
2.4.4 Rutherford backscattering spectrometry (RBS)	32
2.4.5 Micro-Raman spectroscopy	34
2.4.6 Contact angle measurement	36
<u>3 Theoretical Background</u>	<u>39</u>
3.1 Introduction	39
3.2 Statistical methods for characterization of surface	39
3.2.1 Average surface height	39
3.2.2 <i>rms</i> roughness	39
3.2.3 Roughness exponent (α)	40
3.2.4 Correlation functions and correlation length	40
3.2.5 Power spectrum	42
3.2.6 Gradient angle	42
3.2.7 Numerical simulation program	43
3.2.8 Statistical parameters for analysis of periodic morphology	44
3.3 Continuum description of ion bombarded surface evolution	45
3.3.1 Continuum theory	45
3.3.2 Relaxation: Process of surface smoothening	57

3.3.3 Hydrodynamic model	59
3.3.4 Shadowing effect	62
<u>4 Morphological evolution under medium energy ion irradiation</u>	66
4.1 Introduction	66
4.2 Experimental	68
4.3 Results	69
4.3.1 Temporal evolution of Si morphology	69
4.3.1.1 Topography in the low fluence regime: Initial wavelength selection	69
4.3.1.2 Topography evolution in the high fluence regime: Ripple coarsening	70
4.3.1.3 Absence of shadowing effect	72
4.3.1.4 Linear and nonlinear evolutions	73
4.3.1.5 Influence of ion mass on topography surface	77
4.3.2 Influence of ion angle of incidence on surface topography	78
4.3.2.1 Parametric (E - θ) Phase diagram	80
4.4 Discussion	81
4.4.1 Role of ion angle of incidence	81
4.4.2 Initial wavelength selection: Stability analysis	85
4.5 Conclusions	89
<u>5 Microstructural investigation of ripple-patterned surfaces</u>	94
5.1 Introduction	94
5.2 Experimental Details	95

5.3 Results	96
5.3.1 Micro-Raman spectroscopy	96
5.3.2 TEM & EDS study	98
5.3.3 RBS study	101
5.4 Discussion	101
5.4.1 Correlation of the amorphous layer with ripple wavelength	102
5.4.2 Energy scaling of ripple wavelength: Role of nuclear energy loss	105
5.5 Conclusion	109
<u>6 Statistical analysis of ripple morphology formed on Si surfaces</u>	<u>112</u>
6.1 Introduction	112
6.2 Experimental Details	113
6.3 Results	114
6.4 Summary	120
<u>7 Wettability of 60 keV Ar-ion irradiated rippled-Si surfaces</u>	<u>124</u>
7.1 Introduction	124
7.2 Experimental	125
7.3 Results and discussion	125
7.4 Conclusion	134
<u>8 Summary and future scope</u>	<u>137</u>

List of Figures

Figure 1.1: Schematic depiction of ion-solid interaction.....	3
Figure 1.2: Rate of energy deposition, dE/dx , for Ar^+ -ions in Si. Nuclear, electronic and total energy loss are plotted as a function of incident ion energy (E) and reduced energy (ϵ). The dotted green line corresponds to 60 keV Ar^+ -ions in Si. The energy losses are calculated using SRIM 2012 Monte Carlo simulation code [9].....	7
Figure 1.3: Schematic diagram showing the ion-range, spread, depth, longitudinal, and transverse projected range.....	8
Figure 2.1: Schematic layout of the ECR source based ion-beam facility at IUAC, New Delhi. Inset is a side view of the ion source. For our experiments, beam line at 90° was used (Courtesy [3,4]). ECRIS: Electron Cyclotron Resonance Ion Source, AS: Accelerating Section, SW: Switching Magnet, EQD(T): Electrostatic Quadrupole (Triplet). Similar facility ITN, Portugal was also used.	24
Figure 2.2: (a) A schematic diagram showing the working principle of AFM, (b) Van der Waals force as a function of tip to surface distance.....	27
Figure 2.3: (a) the AFM head, (b) Schematic diagram of the probe, (c) SEM image of the cantilever along with tip, and (d) base of the AFM.	28
Figure 2.4: (a) Schematic of RBS (b) Schematic presentation of collision of an energetic incident projectile with target atom.	32
Figure 2.5: A Schematic diagram showing Rutherford backscattering spectroscopy experimental setup. Preamplifier, amplifier, ADC- analog to digital converter, MCA- multi channel analyzer.....	34
Figure 2.6: Energy level diagram demonstrating elastic (Rayleigh) and inelastic (stokes and Anti-stokes) scattering of photons. Excitation light and scattered light are shown here by λ_e and λ_s , respectively.....	35

Figure 2.7: Schematic diagram of (a) Contact angle, δ and (b) its measurement technique. ...	36
Figure 3.1: Schematic demonstration of Gaussian energy deposition of an incoming ion inside a target.	46
Figure 3.2: Schematic illustration of the origin of surface instability induced by ion-beam erosion of non-planar surfaces. θ is the global angle of incidence and γ is the local angle of incidence.	48
Figure 3.3: Schematic diagram of the laboratory coordinate frame (x, z) along with the local coordinate frame (x', z') to represent the CV mechanism. The local normal to the surface is represented by the unit vector z' which is also one axis of the local coordinate frame.	55
Figure 3.4: Illustration of geometry of ion bombardment on a sinusoidal profile. (a) Total surface is exposed to the ion-beam and (b) faceting fully developed beyond the shadowing condition.	62
Figure 4.1: AFM images ($10 \times 10 \mu\text{m}^2$) of Si samples before and after exposure to Ar^+ -ions at an incident angle 60° : (a) Pristine-Si surface, (b)-(d) implanted Si surfaces at fluences 1×10^{18} , 2×10^{18} , and 3×10^{18} ions cm^{-2} , respectively. The corresponding height scales for (b)–(d) are 4.0, 15.9, and 45.4 nm, respectively. The autocorrelation images of the implanted samples are also shown as insets of the corresponding image. Line profiles (taken along the line shown on the autocorrelation images) are shown on the respective autocorrelation images. Arrows indicate the direction of incident ion-beam on the surfaces. (e) Radial 2D PSD calculated as a function of irradiation time. The vertical short line at the highest data point of each plot represents the characteristic wavelength of ripple pattern.	70
Figure 4.2: AFM image of Si (100) surface irradiated at $\theta=60^\circ$ for fluences: (a) 4×10^{18} ions cm^{-2} , (b) 6×10^{18} ions cm^{-2} , and (c) 8×10^{18} ions cm^{-2} . The corresponding height scales are 294.17, 332.13, and 281.2 nm, respectively. Black arrows on the images show direction of the incident ion-beam.	71

Figure 4.3: Ripple wavelength, λ , determined from the autocorrelation functions of the corresponding AFM images as a function ion fluence for $\theta=60^\circ$ 71

Figure 4.4: *rms* roughness of Si surface irradiated at $\theta=60^\circ$ as a function of ion fluence. The dashed vertical line shows the critical fluence for evolution of ripple patterns. The inset shows growth of ripple amplitude in the linear regime as a function of ion fluence. The solid line indicates an exponential fit to the experimental data. 71

Figure 4.5: Distribution of gradient angle over the ripple patterned surfaces (determined from AFM images) for fluences (a) $1-3 \times 10^{18}$ ions cm^{-2} at $\theta=60^\circ$, (b) $3-8 \times 10^{18}$ ions cm^{-2} at $\theta=60^\circ$ and (c) $2-3 \times 10^{18}$ ions cm^{-2} at $\theta=75^\circ$. The inset shows a 3-dimensional (3D) AFM image corresponding to the ion fluence of 8×10^{18} ions cm^{-2} . The white arrow shows direction of the ion-beam projected onto the surface. The red curved line at the crosssection of 3D image is drawn to emphasize the shape of the ripple pattern. 74

Figure 4.6: AFM image of 60 keV Xe^+ -ion irradiated Si as a function of fluence: (a) 1×10^{16} ions cm^{-2} , (b) 2×10^{16} ions cm^{-2} , (c) 5×10^{16} ions cm^{-2} , (d) 1×10^{17} ions cm^{-2} , (e) 2×10^{17} ions cm^{-2} , and (f) 5×10^{17} ions cm^{-2} . The corresponding height scales for (b)-(f) are 1.6, 1.0, 1.5, 5.5, 30.1, and 178.2 nm, respectively. Corresponding ripple heights and wavelengths are plotted in (g). 77

Figure 4.7: AFM images of Si(100): (a) Implanted with 60 keV Ar^+ -ions to the fluence of 2×10^{18} ions cm^{-2} at incident angles of 0° , (b) 30° , (c) 45° , (d) 54° , (e) 60° , (f) 75° , and (g)-(l) are auto correlation image of (a)-(f), respectively. Insets in (g)-(l) show line profiles, taken along the lines shown on the autocorrelation images. Line profiles taken along the line shown on (a) and (b) are numbered by (m), while (n) shows line profile taken along the line shown on (c), (d), (e) and (f). 78

Figure 4.8: Ripple wavelength, λ , determined from the AFM images as a function of angle of incidence θ for a fixed ion fluence of 2×10^{18} ions cm^{-2} 79

Figure 4.9: Parametric phase diagram showing inert gas ion-induced formation of ripple patterns in the medium energy regime (in the fluence range $\sim 10^{18}$ ions cm^{-2}). : Garg *et al.* [12], : Datta *et al.* [2], : Chini *et al.* [22], : Biermanns *et al.* [3], : Carter *et al.* [23], and : Kumar *et al.* [24].80

Figure 4.10: Vacancy distribution in Si due to 60 keV Ar⁺-ion irradiation as simulated by SDTrimSP 5.05: (a) in a direction parallel to the incident beam (*x*-direction), i.e., along depth, (b) along *y-z* directions (perpendicular to the ion-beam, i.e., parallel to the surface).83

Figure 4.11: Plots of the coefficients S_{BH_x} , S_{BH_y} , S_{CV_x} , and S_{CV_y} (as a function of angle of incidence, θ), expressing the contributions of curvature-dependent sputter erosion (BH mechanism) and ion-induced atomic redistribution (CV effect) along *x*- (parallel to the incident beam direction) and *y*-direction (perpendicular to *x*-direction), respectively. The total contributions of the BH mechanism and the CV effect along *x*- and *y*-direction are also shown in the form of S_x and S_y , respectively [40].84

Figure 4.12: Surface morphologies generated by numerical simulations. The images correspond to irradiation times: (a) 7,000, (b) 14,000, and (c) 21,000 s. (d) Corresponding power spectral densities, S_{q_x} . For each curve the position of the absolute maximum is shown by a black line. (e) Average surface height and ripple wavelength as functions of irradiation time. Error bars shown for average heights indicate the corresponding values of the roughness.87

Figure 5.1: Room temperature micro-Raman spectra of pristine and 60 keV Ar-ion irradiated (fluence 2×10^{18} ions cm^{-2}) of the silicon samples at different angles of incidence.96

Figure 5.2: The micro-Raman spectra of Ar⁺-ion irradiated Si samples as a function of ion fluence for (a) $\theta=60^\circ$ for excitation lines of 532 and 488 nm and (b) $\theta=75^\circ$ for excitation line of 488 nm.98

Figure 5.3: (a) and (b): XTEM images of a Si sample irradiated at $\theta=45^\circ$ for fluence 2×10^{18} ions cm^{-2} but taken at two different magnifications, (c) EDS analysis: Plot of Ar atomic percentage as a function of depth in the amorphous region shown in (b).99

Figure 5.4: (a) XTEM image of an irradiated Si sample at $\theta=60^\circ$ and to the fluence of 3×10^{18} ions cm^{-2} , (b) a zoomed view of the marked region in (a), (c) a zoomed view of the marked region in (b), (d) a zoomed XTEM image of the marked region in (c), (e)-(g) are SAED (selected area electron diffraction) images taken from the regions 1, 2, and 3 shown in (a) respectively.99

Figure 5.5: (a) XTEM image of irradiated Si irradiated at $\theta=75^\circ$ to the fluence of 3×10^{18} ions cm^{-2} , (b) XTEM image of the front slope of one ripple shows the presence of Ar bubbles, (c) high-magnification image of the (a/c) interface. 100

Figure 5.6: Experimental and simulated RBS spectra of irradiated Si samples to the fluence 3×10^{18} ions cm^{-2} at incident angles (a) 60° and (b) 75° 101

Figure 5.7: SRIM simulated depth of energy deposition a , straggling of deposited energy distribution σ , and projected ion range R_p at 0° incidence angle, as a function of ion energy. The black vertical line separates low and medium energy regimes..... 103

Figure 5.8: Forward mass distribution parameter δ and average depth of amorphous layer d , as simulated using SRIM, as a function of (a) Ar-ion incident energy E and (b) nuclear energy loss, E_n , of Ar-ions in Si. The black vertical line separates low and medium energy regime. Ripple wavelength is also plotted as a function of ion energy where the right Y-axis shows the value of wavelength [30]..... 107

Figure 5.9: Value of the parameter p as predicted by solid flow model (Eq. 5.8) when only the nuclear energy loss of ions is considered to be effective behind ripple formation..... 108

Figure 6.1: 3D image of ripple patterns on Si surface irradiated by 60 keV Ar^+ ions at $\theta=60^\circ$ to the fluence of 3×10^{18} ions cm^{-2} 114

Figure 6.2: Different texture parameters extracted from irradiated Si surface and plotted as a function of (a) angle of incidence, θ at a fixed fluence of 2×10^{18} ions cm^{-2} , (b) ion fluence, at fixed incidence angle $\theta=60^\circ$ 115

Figure 6.3: Lateral correlation lengths in x and y -direction, $\zeta_{x,y}$, system correlation length in the x -direction, ζ_x , ratio of ζ_x to ripple wavelength λ as a function of (a) incidence angle, θ at a fixed fluence of 2×10^{18} ions cm^{-2} , (b) ion fluence at a fixed incidence angle $\theta=60^\circ$. The dotted black line distinguishes linear and nonlinear regimes. 117

Figure 6.4: 1-dimensional roughness exponent (α_x, α_y where, x - and y -directions are parallel and perpendicular to the direction of incident ion-beam, respectively), anisotropy in roughness exponent (R.E.) and scaling anisotropy, γ are plotted as functions of (a) incident angle, θ , at a fixed fluence and (b) ion fluence at a fixed incident angle of 60° while the dashed vertical line was drawn to distinguish the linear and nonlinear regimes. 118

Figure 7.1: A typical sessile drop with the spherical cap on the pristine and 60 keV Ar^+ -ion irradiated Si surfaces at incident angles $\theta=0^\circ$ and 60° . Contact angles (δ) were measured for pristine and irradiated surfaces as a function of ion fluence. For ripple patterned surfaces, δ values were measured in two directions: (1) parallel and (2) perpendicular to the ripple wave-vector..... 126

Figure 7.2: Variation in δ and w versus ion fluence for 60 keV Ar^+ -ion irradiation of Si surface at $\theta=0^\circ$. The inset show AFM images of pristine and normally implanted Si (to the fluence of 3×10^{18} ions cm^{-2}) samples..... 127

Figure 7.3: Schematic diagram of water droplet on (a) an isotropic surface (2D top view) and (b) an anisotropic (rippled) surface generated at $\theta=60^\circ$ for fluence 3×10^{18} ions cm^{-2} (3D side view). Set of red lines ‘1’ and ‘2’ show the different contact positions (orthogonal to each other) of the water droplet with the surface. 130

Figure 7.4: Variations in the measured δ and w values as a function of ion fluence for 60 keV Ar-ion irradiated Si at an incident angle of 60° . For ripple patterned surface, δ were plotted for two directions [as described in Fig. 7.3]: (i) parallel and (ii) perpendicular to the direction of the ripple wave-vector. 131

Figure 7.5: XTEM image of ion-induced ripple pattern on Si surface, formed at an incident angle of 60° and fluence of 3×10^{18} ions cm^{-2} . Front slope of ripple has been encircled whereas white patches in the near-surface region of the amorphous layer indicate Ar-bubbles. 132

CHAPTER 1

1 Introduction

1.1 Preamble

Ion bombardment is a versatile, efficient, and widely used technique for synthesis, modification, and characterization of materials. Because of a good control over energy and spatial distribution of the ion species, this technique has found important applications both in basic research as well as in technological applications. For instance, ion implantation, i.e., introduction of foreign atoms in a matrix by bombardment of ions having energy from a few to tens of keV to a few MeV is under extensive use for decades for modification of various physical properties of materials such as electronic, magnetic, optical, or mechanical properties. Ion implantation is also routinely used in semiconductor industry for doping of materials. Ion-beam sputtering (removal of target atoms by ion bombardment) is employed for ion-beam polishing or deposition of thin films. Atoms sputtered out from the surface due to ion bombardment are also utilized to detect extremely low concentration of material in secondary ion mass spectrometry. On the other hand, techniques like Rutherford Backscattering spectrometry/Channeling utilize MeV energy ion-beam to analyze the compositional and crystalline aspects of materials.

In the context of ion-solid interaction, it is customary to classify the ion energy ranges. Ions having energy in the range 0.5–10 keV are called low energy ions, 10–500 keV are referred to as medium energy ions, and those with energy beyond 500 keV are known as high energy ions [1].

Wider application of ion bombardment has been stimulated by the development of advanced characterization tools to probe nanometer length scale. In particular, spontaneous formation

of periodic nanoscale patterns on solid surfaces under normally or obliquely incident ion bombardment has been a subject of recent interest [2]. The interest is further motivated by recent discovery of the potential of these nanoscale periodic features to tailor material properties. These patterned surfaces are found to be extremely useful as templates for depositing functional thin films where the film properties are greatly influenced by the periodicity of the underlying substrates. For instance, patterned substrates have been used to control the spin orientation and directionality in magnetic thin films [3,4]. Anisotropic plasmon absorption was shown by aligned Ag nanoparticle array over rippled surface [5]. Very recently, it has been shown that conformal Al-doped ZnO overlay as grown on nanofaceted silicon template, can reduce surface reflectance to a significant extent [6].

On the other hand, recent advancements in theoretical formulations of ion bombardment induced surface evolution have inspired experimental investigation of the same. The current theoretical models predict features of ion bombardment induced patterning such as linear and nonlinear modes of pattern evolution, influence of ion-beam shadowing, contributing factors like curvature-dependent sputtering, ion induced mass redistribution, or viscous flow. As will be discussed below, medium energy ion bombardment on solid surface provides an experimental platform to recognize the applicability of theoretical models or relevance of physical mechanisms in a particular experimental situation. This is extremely important for a complete theoretical understanding of the patterning process which is necessary to engineer the surface topography for novel technological applications.

1.2 Ion-Solid interaction

1.2.1 Basics

When a beam of energetic ion impinges on a target, most of the incident ions penetrate through the surface into the target. Inside the target, ions undergo a series of collisions with target atoms and electrons, thereby transferring their energy. This leads to a sequence of

events as illustrated in Fig. 1.1. We briefly describe the interactions of energetic ions and resulting processes with reference to Fig. 1.1.

- (1) A very small fraction of the incident ions, which undergoes large angle scattering in the collision events with target atoms, are reflected back.
- (2) Most of the incident ions penetrate through the surface and enters into the target. Inside the target, ions lose energy through elastic collisions with target atoms (called *nuclear energy loss*) and inelastic collisions with target electrons (called *electronic energy loss*). After their losing energy, the ions finally come to rest at a certain depth from the surface. This process of introducing foreign atoms in a target is known as ion implantation.

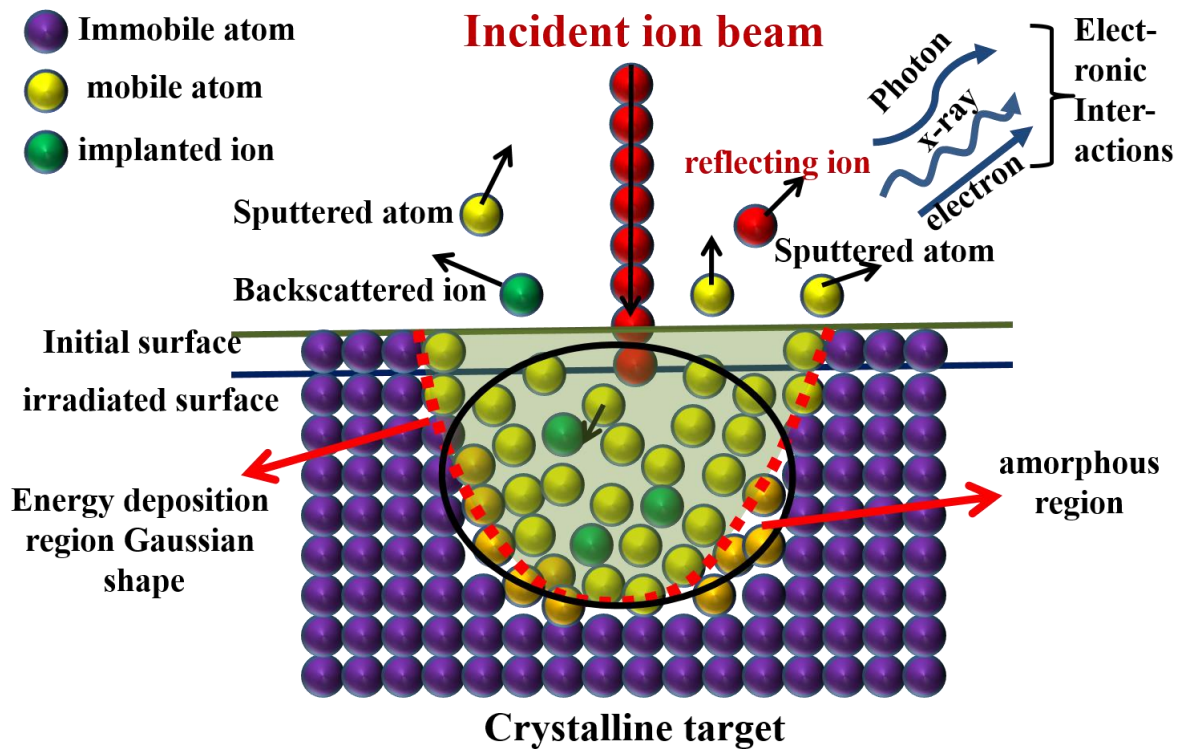


Figure 1.1: Schematic depiction of ion-solid interaction.

- (3) Due to the energy transfer in nuclear collisions (ion-target atom collision), the target atoms are displaced from their lattice sites and become mobile. The mobile atoms lose energy in similar collisions with stationary target atoms and target electrons, creating more numbers of mobile target atoms. The consecutive collision processes lead to formation of a

region inside target where most of the atoms are mobile. This region is called the collision cascade.

(4) If any mobile target atom near the surface has a component of velocity perpendicular to the surface and energy greater than the surface energy barrier, then the atom can be ejected from the target. This process is called *sputtering*. A solid target is eroded under ion bombardment due to sputtering.

(5) Energy loss to target electrons gives rise to ejection of electron from the target, or emission of visible or X-ray photon.

(6) The displacement of target atoms from lattice site creates highly disordered zones consisting of vacancies and interstitials. At sufficiently high ion fluence the individual disordered zones may overlap to lead to amorphization of the target.

1.2.2 Ion stopping

The rate of energy loss of ions inside a target is expressed through the stopping power dE/dx , where dE is the energy lost by the incident ions in traversing a distance dx measured from a reference frame parallel to the surface. The stopping power can be written as a summation of energy loss rates due to nuclear and electronic collisions as

$$\frac{dE}{dx} = \left(\frac{dE}{dx}\right)_n + \left(\frac{dE}{dx}\right)_e, \quad (1.1)$$

where $\left(\frac{dE}{dx}\right)_n$ and $\left(\frac{dE}{dx}\right)_e$ are the stopping powers due to nuclear and electronic energy loss, respectively. Energy loss rate is often expressed in terms of stopping crosssection $S(E)$ defined as

$$S(E) = \frac{1}{N} \frac{dE}{dx} = \frac{1}{N} \left(\frac{dE}{dx}\right)_n + \frac{1}{N} \left(\frac{dE}{dx}\right)_e = S_n(E) + S_e(E), \quad (1.2)$$

where N is the atomic density of the target [7].

Nuclear Stopping

The interaction between an energetic ion and target atoms can be expressed in terms of the potential $V(r)$ between them. $V(r)$ can be written as

$$V(r) = 0 \quad \text{for } r > r_0,$$

$$= \frac{Z_1 Z_2 e^2}{r^2} \chi(r) \quad \text{for } a_0 < r < r_0. \quad (1.3)$$

Here, r , r_0 , and a_0 are the distance of separation of the incident ion and target atom, equilibrium distance of atoms in a solid, and Bohr radius of hydrogen atom, respectively. Z_1 and Z_2 are the atomic number of incident ion and target atom, respectively and e is the electronic charge. $\chi(r)$ is a screening function which represents the electrostatic screening of nuclear charge by atomic electrons. In order to calculate the nuclear stopping, power law form of the interatomic potential $V(r) \sim r^{-1}$ can be assumed where the screening function $\chi(r)$ is approximated in power form as $\chi(r/a_{TF}) = (k_s/s)(a_{TF}/r)^{s-1}$, where $s=1,2 \dots k_s$, a numerical constant. a_{TF} is Thomas-Fermi screening radius defined as

$$a_{TF} = \frac{0.88534 a_0}{\left(Z_1^{1/2} + Z_2^{1/2}\right)^2}, \quad (1.4)$$

in this power law form of interatomic potential, the nuclear stopping is given by [7],

$$S_n(E) = \frac{C_m E^{1-2m}}{1-m} \left[\frac{4M_1 M_2}{(M_1 + M_2)^2} \right], \quad (1.5)$$

where,

$$C_m = \frac{\pi}{2} \lambda_m a_{TF}^2 \left(\frac{Z_1 Z_2 e^2}{a_{TF}} \right)^{2m} \left(\frac{M_1}{M_2} \right)^m. \quad (1.6)$$

Here, $m=1/s$ and λ_m is a fitting variable has the functional form

$$\lambda_m = 2m \left(\frac{k_s \Gamma(1/2) \Gamma(1/2+s)}{4\Gamma(s/2+1)} \right)^{2m}, \quad (1.7)$$

this stopping crosssection can be shown in more compact form by defining reduced energy (ε) and reduced length (ρ) as:

$$S_n(\varepsilon) = \frac{d\varepsilon}{d\rho_L} = \frac{\lambda_m}{2(1-m)} \varepsilon^{1-2m}, \quad (1.8)$$

$$\text{where } \varepsilon = \frac{M_2}{M_1+M_2} \cdot \frac{a_{TF}}{Z_1 Z_2 e^2} E \quad ; \quad \rho_L = 4\pi L N a_{TF}^2 \left[\frac{M_1 M_2}{(M_1+M_2)^2} \right], \quad (1.9)$$

the value of the exponent m depends upon the reduced energy (ε) as

$$\begin{aligned} m=1/3 & \quad \text{for } \varepsilon \leq 0.2 \\ m=1/2 & \quad \text{for } 0.08 \leq \varepsilon \leq 2 \\ m=1 & \quad \text{for } \varepsilon > 2, \end{aligned} \quad (1.10)$$

an approximation of screening function was given by Ziegler, Biersack and Littmark (ZBL) [8] for which the corresponding nuclear stopping is applicable to wider values of ε . Such higher values of ε corresponding to very high energy ion-beam are out of the scope of this thesis and not discussed here.

Electronic Stopping

This electronic energy loss of an energetic ion inside a solid is dependent on the velocity of the ions. For the ion velocity $v < v_0 Z_1^{2/3}$, where v_0 is the Bohr velocity of atomic electron, electronic stopping crosssection was derived by Lindhard and Scharff [7] as:

$$S_e(E) = 3.83 \frac{Z_1^{7/6} Z_2}{(Z_1^{2/3} + Z_2^{2/3})^{3/2}} \left(\frac{E}{M_1} \right)^{1/2} = K_L E^{1/2}, \quad (1.11)$$

the other terms except energy are included in the constant K_L . In terms of reduced energy (ε) and reduced length (ρ) the above formula becomes

$$S_e(\varepsilon) = \left(\frac{d\varepsilon}{d\rho} \right)_e = \frac{Z_1^{2/3} Z_2^{2/3} \left(1 + \frac{M_2}{M_1} \right)^{3/2}}{12.6 (Z_1^{2/3} + Z_2^{2/3})^{3/4} M_2^{1/2}} \varepsilon^{1/2} = k(\varepsilon)^{1/2}. \quad (1.12)$$

In the high energy range where ion velocity $v > v_0 Z_1^{2/3}$, the influence of the incident ion can be regarded as a sudden, small perturbation to the target electrons. This interaction of high energy ion-beam with target electrons is out of the scope of this thesis and not discussed here.

Fig. 1.2 shows a comparison of nuclear and electronic energy loss for Ar-ion irradiation in Si.

In the low energy range (0.5-10 keV) total energy deposition rate follows the nuclear energy loss curve. In the medium energy range (10-500 keV) total energy curve starts to deviate

from nuclear energy loss curve due to the increasing electronic energy loss of ions at higher energy. At high energy (above 1 MeV) where $\epsilon > 10$ (for nuclear energy loss) and $v > v_0 Z_1^{2/3}$, the electronic energy loss of ions become the dominant energy loss process.

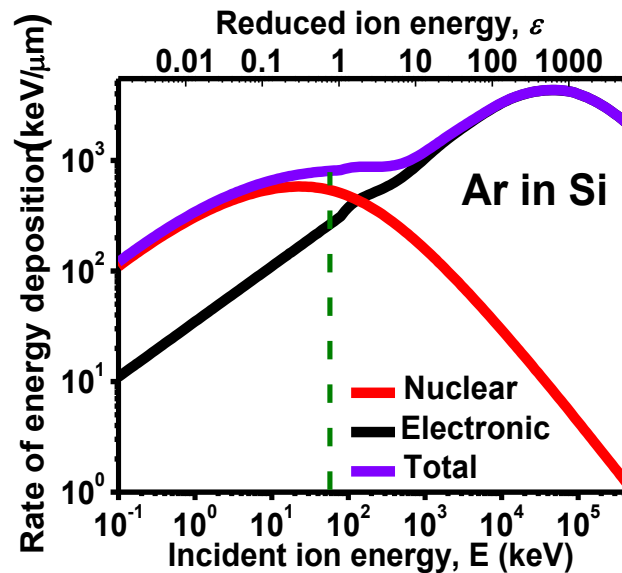


Figure 1.2: Rate of energy deposition, dE/dx , for Ar^+ -ions in Si. Nuclear, electronic and total energy loss are plotted as a function of incident ion energy (E) and reduced energy (ϵ). The dotted green line corresponds to 60 keV Ar^+ -ions in Si. The energy losses are calculated using SRIM 2012 Monte Carlo simulation code [9].

1.2.3 Ion range and straggling

When an energetic ion travels through a solid, its direction of motion keeps on changing due to collisions with the target atoms. The trajectory of the ions thus becomes a zigzag one instead of a straight line. A three-dimensional schematic presentation of the process is shown in Fig. 1.3. In this Figure, the origin of the coordinate system is taken at the surface of the solid target with Y and Z-axes parallel to the surface and positive X-axis normal to the surface pointing into the solid.

An incident ion (shown by the green arrow) hits the surface at the origin 'O'. The trajectory of the incident ion is considered to be in the X-Y plane. After entering the target, the ion follows the zigzag path shown by the yellow line and comes to rest at the point 'A' with coordinate (x', y', z') . The projection of point "A" at the sample surface is the point "B" with

coordinate $(0, y', z')$. The distance from the point of impact O to point B (OB) is known as ‘range spread’ and length AB is called the ‘penetration depth’. AA’ is a perpendicular line on green line from point “A” and this length is called as ‘transverse projected range’ and length ‘OA’ is known as ‘projected range’ (or more precisely ‘longitudinal projected range’). Due to the random nature of slowing down of ions inside a target, all the incident ions do not travel the same distance inside the target. In other words, the projected range of the incident ions follows a distribution which is generally Gaussian in nature. The width of this distribution is called the ‘range straggling’.

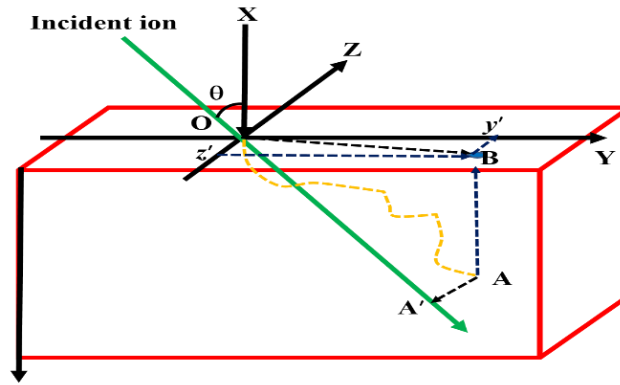


Figure 1.3: Schematic diagram showing the ion-range, spread, depth, longitudinal, and transverse projected range.

The average ion range (R) can be expressed in term of incident ion energy (E_0) [7] as:

$$R(E_0) = \left(\frac{1-m}{2m}\right) \frac{\gamma^{m-1}}{NC_m} E_0^{2m}, \quad (1.13)$$

Here, $\gamma = 4M_1M_2/(M_1 + M_2)^2$, C_m and m are defined in Eq. 1.6 and 1.10 respectively.

1.2.4 Sputtering

Sputtering is the removal of target atoms under ion bombardment. Sputtering is described quantitatively by the sputtering yield (Y), defined as [7]

$$Y = \frac{\text{Number of sputtered atoms}}{\text{Number of incident ions}} = \Lambda F_D = \frac{\alpha N S_n(E)}{E_B}. \quad (1.14)$$

Here, Λ is a constant which depends on the materials properties, F_D is the nuclear energy deposition per unit length, N and E_B are the target atomic density and surface binding energy,

respectively, and α is a correction factor that depends on the ratio of ion and solid atomic masses. Moreover, light-ion sputtering is independent of temperature, and heavy-ion sputtering is only influenced by temperature close to the target melting point [10]. The sputtering yield has its maximum value when the incident particle energy is somewhere in medium energy. At higher energies, the particle penetrates deeper into the target and fewer surface atoms are removed, lowering the sputtering yield. When the mass equals the target mass, sputtering yield is maximized.

The sputtering yield, Y_E , at incident ions energy E , can be approximated by an empirical formula

$$Y_E = 0.42 \frac{\alpha_s Q_s S_n(E)}{E_B [1 + 0.35 E_B S_e(\varepsilon)]} \chi^{2.8}, \quad (1.15)$$

where, $\chi = 1 - (E_{th}/E)^{0.5}$, α_s and Q_s are empirical parameters determined from experimental sputtering yield data, and E_{th} is the sputtering threshold.

The sputtering yield, in general, is an increasing function of ion angle of incidence, θ (with respect to surface normal), except at very high angles where the reflection of ions from the surface becomes the dominating factor. An approximate relationship of the sputtering yield, Y_θ , corresponding to ion angle of incidence θ , to sputtering yield Y_0 for normal ion incidence is given by

$$\frac{Y_\theta}{Y_0} = (\cos \theta)^{-f_s}, \quad (1.16)$$

f_s is a function of M_2/M_1 [7].

Experimentally obtained sputtering yield starts to deviate from the behavior predicted by Eq. 1.16 at higher incident angles. By carrying out a more detailed study, Yamamura *et al.* [11,12] put forward the following empirical relationship between Y_θ and Y_0

$$Y_\theta = Y_0 \left(\frac{1}{\cos \theta} \right)^f \exp \left(-\Sigma \left(\frac{1}{\cos \theta} - 1 \right) \right). \quad (1.17)$$

Where, f is the function of energy, $f = 1.85 \left(1 + 1.25 \left(\frac{1-\chi}{\chi} \right) \right)$, $\Sigma = f \cos \theta_{opt}$ where θ_{opt} is the angle at which sputtering yield found to be the maximum. Eq. 1.17 provides a more realistic description of sputtering yield compared to Eq. 1.16, especially at higher incident angles.

1.2.5 Numerical simulation of ion-solid interaction

Detailed simulation of ion-solid interactions over a large range of ion energies can be carried out using Monte-Carlo and molecular dynamics simulation codes available at present. These simulation codes offer a way of understanding the physical processes taking place in particular experimental situations by providing details of ion stopping, resulting radiation damage, sputtering, ion and recoil distributions, etc. For the present study, the necessary simulations were performed using SRIM [9,13,14], TRIDYN [15] and SDTrimSP [16] codes. SRIM: SRIM (Stopping and Range of Ions in Matter) is a simulation package based on the Monte Carlo code TRIM (Transport and Range of Ions in Matter) [9,13,14]. TRIM follows history or ion trajectories of a large number of individual ions or particles in a target. They all begin with a given energy, position, and direction. The particle is assumed to change direction as a result of binary nuclear collisions and moves in a straight path between two consecutive collisions. The energy of the particle is reduced as a result of nuclear and electronic (inelastic) collisions, and a trajectory is terminated either when the energy drops below a pre-specified value or when the particle position is outside the target. The target is considered amorphous with atoms at random locations and thus, the directional properties applicable for a crystalline material are ignored. This code calculates the final three-dimensional distribution of the ions and all kinetic phenomena associated with the ion's energy loss such as sputtering yield, target damage etc.

The applicability of TRIM is limited in the sense that the modification of the target composition due to ion implantation and erosion of the target surface due to sputtering is not

taken into account during simulation. Therefore, the simulated results such as the distribution of implanted species conforms to experimentally obtained data mostly in the limit of low implantation fluence [$\sim 10^{14}$ ions cm^{-2}] since significant compositional modification of the target occurs at high fluences.

TRIDYN: TRIDYN [15] use the same Monte Carlo method as TRIM to simulate the interaction of energetic ions and target atoms. However, TRIDYN includes the dynamic change in the target during ion bombardment. TRIDYN provides reliable values of sputtering yield, modified target composition or implantation distribution at high fluences. However, the information about the final three-dimensional distribution of ions and recoils/vacancies are not provided by TRIDYN.

SDTrimSP: The features of TRIM and TRIDYN have been incorporated in SDTrimSP [16] to provide a versatile platform for simulating monoatomic as well as compound targets, layered structures, fixed and variable composition target structures with a wide variety of projectiles, and target geometries. While SDTrimSP is a Monte Carlo code based on the same binary collision approximation such as TRIM and TRIDYN, it provides details like three-dimensional distribution of ions, recoil atoms, vacancies, variation in sputtering yield, angular distribution of sputtered particles etc. In fact, it provide much accurate values of various parameters like ion range, straggling, damage distributions, etc. Especially, the transverse straggling of ion energy distribution can be extracted much more reliably using SDTrimSP compare to TRIM.

1.3 Ion-beam induced pattern formation

The first observation of ion-beam induced self-organized patterning was reported by Navez *et al.* [17] back in 1962. In their work, ripple patterns were obtained on glass surface by using low energy argon ions. Even after more than fifty years since the discovery, the interest towards self-organized periodic surface patterning using energetic ion-beams is still growing

[18,19]. This is because of the recently discovered promising technological applications of the patterned surfaces as well as for the continuing development in the theoretical understanding of ion-beam patterning. A series of periodic patterns viz. nano-dots [20], -holes [21], -ripples, and facets [22,23], have been observed to evolve on wide variety of materials ranging from metals [24,25], semiconductors (elemental and compound) [26,27], oxides [28], to polymers [29]. The most important factor that determines the length scale of patterns is seen to be energy of the incident ions. At the same time, patterning is dependent upon experimental parameters like ion -incident angle, -mass, -current density, -fluence, -flux, composition of the substrate, and substrate temperature. In addition, the impurities present on the surface have been seen to drive pattern formation [30]. While the dependence of patterning on such a large range of parameters makes the theoretical understanding a challenging task, they also open up ways to tune the surface features for specific applications. Low energy ion-beam induced pattern formation has been studied by many investigators [2,20,23,31-33]. However, on many occasions, the experimental results are found to contradict the theoretical predictions [34]. The understanding of the processes involved are far from complete and calls for further experimental explorations as well as theoretical formulation.

While the periodic patterning of the surface is observed both for low energy as well as medium energy ion bombardment of solid surfaces, medium energy ion induced patterns have amplitudes tens of nanometers and periodicity of the order of hundreds of nanometers, respectively [35-39]. This is much higher compared to pattern dimensions generally observed at low energies, viz., pattern height are extended up to a few nanometers and pattern periodicity are of tens of nanometers. The feature dimensions at medium energy make it possible to study the aspects which are in general difficult for patterns induced by low energy ions.

1.4 Motivation for experimental studies presented in this thesis

Theoretically, ion induced patterning is considered to be an outcome of competing processes, viz. roughening due to curvature-dependent sputtering [34] or ion induced mass redistribution [40] and surface smoothening processes due to thermal diffusion [41], ion induced effective diffusion [42], or viscous flow [43]. Further, a recent model by Castro *et al.* [44] explained surface patterning as a result of ion-induced stress dependent solid flow. In comparison to low energy case [31], less research efforts were devoted towards medium energy ion induced patterning [37,45,46] and thus, the understanding of the processes involved is still far from complete. Moreover, as we discussed above, the length scale of medium energy ion induced surface patterns provides opportunity for studying some issues which are important but are yet to be explored. We briefly introduce the issues about medium energy ion-beam induced pattern evolution below.

Early stage of ripple formation: Most of the reported studies [37,46,47] involving medium energy ions focused on pattern evolution at high fluences ($> 10^{18}$ ions cm^{-2}) where the phenomena like shadowing starts to influence the morphological evolution. On the other hand, dynamics of evolution at the very early stage of irradiation has not been investigated yet. The understanding of the early stage of dynamics is important not only for tuning the patterning at medium energies but also to establish the similarity of patterning at low and medium energies, which will confirm the feasibility of understanding the patterning under low and medium energy ion bombardment in light of a common theoretical framework. In fact, the length scale of medium energy ion induced patterns provides a unique experimental platform to correlate the early stage of pattern evolution in the framework of existing theoretical models.

Role of ion fluence and ion angle of incidence: Datta *et al.* [48] showed the formation and coarsening of ripple patterns on Si under 30 and 60 keV Ar^+ -ion irradiation. Dependence of

pattern formation on angle of ion incidence was also investigated by Datta *et al.* [48] for 30 keV Ar⁺-ions. However, the observed absence of pattern formation below $\theta=55^\circ$ could not be explained by invoking curvature-dependent sputtering theory. In fact, a systematic investigation on the influence of ion incidence angle on surface patterning, in conjunction with numerical estimation based on the theoretical models, is still lacking in case of medium energy ion irradiation, although this is essential towards identifying the physical mechanisms contributing to ripple formation, as shown in low energy cases. In addition, late stage dynamics of ripple patterns as observed by Chini *et al.* [49] was dominated by ion-beam shadowing, in addition to nonlinear effects. Consequently, the linear and nonlinear evolution of ripples in the medium energy regime, in absence of any coexistent contributing factor like shadowing, is yet to be demonstrated. Further, in case of medium energy irradiation, the deviation in energy scaling of ripple wavelength, as reported by Biermanns *et al.* [37] from theoretical prediction remains unexplained.

Influence of structural and compositional change on pattern formation: Ion irradiation introduce structural damage in targets, leading to structural phase transformation of the irradiated layer from a single crystalline to polycrystalline or amorphous one at high enough ion fluences. Especially for semiconductors such as Si, experimental studies revealed that amorphization take place in the fluence range of 10^{14} - 10^{15} ions cm^{-2} [50,51] under heavy ion bombardment. As the critical ion fluence for the formation of surface patterns is around $\sim 10^{17}$ ions cm^{-2} , the target damage is expected to play a key role in the pattern formation process. In fact, recently it has been conjectured that the patterning of surface starts from the amorphous/crystalline interface created by ion irradiation and grows towards the surface [52]. Further, high fluence ion irradiation results in compositional modification of the surface layer due to implantation of ions in the sub-surface layer likewise, preferential sputtering of one element in case of compound targets also plays a key role in pattern formation. Systematic

structural and compositional analyses on ion-beam fabricated rippled surfaces can thus, provide important information on ripple formation and its temporal evolution in the medium ion energy regime.

Statistical characterization of patterned substrates: The texture of ion-irradiated patterned surface plays a key role in technological applications of the same [53-56]. Thus, statistical analysis of surface patterns is an important requirement to decide on the applicability of patterned substrates towards specific applications. However, in-depth statistical analysis of ripple patterns is still lacking, both for medium as well as low energy cases.

Thus, a systematic study of medium energy ion induced pattern evolution, with particular attention to the features which remains unexplored till now, as mentioned above, is extremely important for a complete understanding of patterning process towards engineering the surface topography for novel technological application(s). In this thesis, we present our experimental investigations on medium energy ion-beam induced morphological evolution of Si surface and related microstructural changes. In our studies, we have particularly addressed above-mentioned important aspects of ion-beam patterning at this energy regime. Besides the experimental studies, we have also carried out detail numerical estimations based upon current theoretical models of ion-bombarded surface evolutions using simulation packages, viz. SRIM, TRIDYN, and SDTrimSP. Our studies reveal in-depth information on ripple pattern evolution in the medium energy regime over a large angular window and ion fluences.

Importance of Si as a target: Silicon was selected as the target material for the present study because it is a mono-elemental target whose physical properties are well-known and is easily amorphized by ion irradiation. Thus, it deserves to be an ideal platform for exploring morphological evolution in conjunction with the theoretical models which are directly applicable to amorphous elemental target. Noble gas ions such as Argon and Xenon were chosen as these noble gas are inert in nature and leaves the irradiated sample as ideal

amorphous monoatomic system for theoretical models. Further, the interaction of noble gas ions with Si is considered to be of fundamental interest in the field of ion implantation and related applications.

1.5 Organization of the thesis

This thesis presents studies on temporal evolution of surface morphology in case of Si under medium energy ion bombardment and associated structural and compositional modifications. We attempt to understand our experimental observations in the framework of existing theoretical models and selectively compare it with low energy ion induced pattern formation. The thesis is organized in the following manner:

Chapter 1: This chapter gives a brief introduction to ion-solid interaction as related to the issues covered in the studies presented in the thesis. The introductory description of ion irradiation induced surface patterning and the motivation behind our study are also given.

Chapter 2: This chapter describes the experimental techniques employed for carrying out the studies presented in this thesis.

Chapter 3: In this chapter, we first describe the statistical methods for classification and analysis of surfaces. Afterwards, we briefly outline the theoretical models developed to describe surface morphological evolution on amorphous solid surfaces. A brief description of the simulation methods used in our work is also given.

Chapter 4: This chapter describes the results of our detail experimental investigations on self-organized ripple pattern formation on Si surface under 60 keV Ar and Xe ion-beams. Here, we have explored the effect of role of ion angle of incidence, θ , in a large range of 0° to 75° at this energy and the evolution of surface morphology with ion fluence for angle of incidence $\theta=60^\circ$ and 75° . For the first time we have created a parametric ion energy-angle (E - θ) phase diagram to summarize the pattern formation in the medium energy range. With

the help of these phase diagram we discussed our experimental results in light of the existing theoretical models introduced in chapter 3.

Chapter 5: Here we present the structural and compositional modification of the rippled surface layers by ion irradiation. Subsequently, we discuss the role of ion energy deposition in pattern evolution.

Chapter 6: This chapter presents comprehensive statistical analysis of the patterned surfaces as a function of ion fluences and incident angle, which generate under medium energy ion irradiation.

Chapter 7: In this chapter, as a possible application of the ripple patterned Si surfaces, we present the wettability of the patterned surfaces generated under medium energy Ar-ion irradiation at room temperature.

Chapter 8: In this chapter, we have summarized our studies presented in this thesis. Further, we have outlined the future scope of experimental studies based on our results and their importance towards deeper understanding of the ion induced pattern formation and possible applications of generated patterns.

Bibliography

1. L. Hanley and S.B. Sinnott, *Surf Sci.* 500 (2002) 500.
2. T. Som and D. Kanjilal, *Nanofabrication by Ion-Beam Sputtering: Fundamentals and Applications*. 2012, Singapore: Pan Stanford.
3. L. Gridneva, A. Persson, M. Niño, J. Camarero, J. de Miguel, R. Miranda, C. Hofer, C. Teichert, T. Bobek, and A. Locatelli, *Phys. Rev. B* 77 (2008) 104425.
4. F. Bisio, R. Moroni, F.B. de Mongeot, M. Canepa, and L. Mattera, *Phys. Rev. Lett.* 96 (2006) 057204.
5. T. Oates, A. Keller, S. Facsko, and A. Mucklich, *Plasmonics* 2 (2007) 47.
6. T. Basu, M. Kumar, P.K. Sahoo, A. Kanjilal, and T. Som, *Nanoscale Res. Lett.* 9 (2014) 1.
7. M. Nastasi, J.W. Mayer, and J.K. Hirvonen, *Ion-solid interactions: Fundamentals and applications*. 1996: Cambridge University Press.
8. J.F. Ziegler and J.P. Biersack, *The stopping and range of ions in matter*. 1985: Springer.
9. J.F. Ziegler, J.P. Biersack, and K. Littmark, *The stopping and Range of Ions in Matter*. 1985, Pergamon, New York. p. See also "<http://www.srim.org/>".
10. R. Behrisch and H.H. Andersen, *Sputtering by particle bombardment*. Vol. 1. 1981: Springer.
11. Y. Yamamura, Y. Itikawa, and N. Itoh, Report IPPJ-AM-26, Institute of Plasma Physics, Nagoya University (1983).
12. Y. Yamamura, C. Mössner, and H. Oechsner, *Radiat. Eff.* 103 (1987) 25.
13. J. Biersack and L. Haggmark, *Nucl. Instrum. Methods* 174 (1980) 257.
14. J. Biersack and W. Eckstein, *Appl. Phys. A* 34 (1984) 73.
15. W. Möller and W. Eckstein, *Nucl. Instrum. Methods Phys. Res. B* 2 (1984) 814.

16. W. Eckstein, R. Dohmen, A. Mutzke, and R. Schneider, IPP Report 12 (2007).
17. M. Navez, D. Chaperot, and C. Sella, CR Hebd. Seances Acad. Sci 254 (1962) 240.
18. M.J. Nobes, J.S. Colligon, and G. Carter, J. Mater. Sci. 4 (1969) 730.
19. G. Carter, M. Nobes, F. Paton, J. Williams, and J. Whitton, Radiat. Eff. 33 (1977) 65.
20. S. Facsko, T. Dekorsy, C. Koerdt, C. Trappe, H. Kurz, A. Vogt, and H.L. Hartnagel, Science 285 (1999) 1551.
21. V. Venugopal, S.K. Garg, T. Basu, O.P. Sinha, D. Kanjilal, S.R. Bhattacharyya, and T. Som, Appl. Surf. Sci. 258 (2012) 4144.
22. B. Ziberi, F. Frost, T. Höche, and B. Rauschenbach, Phys. Rev. B 72 (2005) 235310.
23. T. Basu, J.R. Mohanty, and T. Som, Appl. Surf. Sci. 258 (2012) 9944.
24. U. Valbusa, C. Boragno, and F.B.d. Mongeot, J. Phys.: Condens. Matter 14 (2002) 8153.
25. G. Debabrata, J. Phys.: Condens. Matter 21 (2009) 224001.
26. T. Som, T.K. Chini, Y.S. Katharia, S. Tripathy, and D. Kanjilal, Appl. Surf. Sci. 256 (2009) 562.
27. R. Gago, L. Vázquez, R. Cuerno, M. Varela, C. Ballesteros, and J.M. Albella, Appl. Phys. Lett. 78 (2001) 3316.
28. M. Lu, X.J. Yang, S.S. Perry, and J.W. Rabalais, Appl. Phys. Lett. 80 (2002) 2096.
29. Q. Wei, J. Lian, S. Zhu, W. Li, K. Sun, and L. Wang, Chem. Phys. Lett. 452 (2008) 124.
30. A. Redondo-Cubero, R. Gago, F. Palomares, A. Mücklich, M. Vinnichenko, and L. Vázquez, Phys. Rev. B 86 (2012) 085436.
31. C.S. Madi, B. Davidovitch, H.B. George, S.A. Norris, M.P. Brenner, and M.J. Aziz, Phys. Rev. Lett. 101 (2008) 246102.

32. R. Gago, L. Vázquez, R. Cuerno, M. Varela, C. Ballesteros, and J. Albella, *Nanotechnology* 13 (2002) 304.
33. B. Ziberi, F. Frost, T. Höche, and B. Rauschenbach, *Vacuum* 81 (2006) 155.
34. R.M. Bradley and J.M.E. Harper, *J. Vac. Sci. Technol. A* 6 (1988) 2390.
35. G. Carter, V. Vishnyakov, Y.V. Martynenko, and M.J. Nobes, *J. Appl. Phys.* 78 (1995) 3559.
36. T.K. Chini, M.K. Sanyal, and S.R. Bhattacharyya, *Phys. Rev. B* 66 (2002) 153404.
37. A. Biermanns, U. Pietsch, J. Grenzer, A. Hanisch, S. Facsko, G. Carbone, and T.H. Metzger, *J. Appl. Phys.* 104 (2008) 044312.
38. H. Antje, B. Andreas, G. Jörg, F. Stefan, and P. Ullrich, *J. Phys. D: Appl. Phys.* 43 (2010) 112001.
39. S.K. Garg, V. Venugopal, T. Basu, O.P. Sinha, S. Rath, D. Kanjilal, and T. Som, *Appl. Surf. Sci.* 258 (2012) 4135.
40. S.A. Norris, M.P. Brenner, and M.J. Aziz, *J. Phys.: Condens. Matter* 21 (2009) 224017.
41. W.W. Mullins, *J. Appl. Phys.* 28 (1957) 333.
42. M.A. Makeev and A.-L. Barabási, *Appl. Phys. Lett.* 71 (1997) 2800.
43. C.C. Umbach, R.L. Headrick, and K.-C. Chang, *Phys. Rev. Lett.* 87 (2001) 246104.
44. M. Castro, R. Gago, L. Vázquez, J. Muñoz-García, and R. Cuerno, *Phys. Rev. B* 86 (2012) 214107.
45. G. Carter and V. Vishnyakov, *Phys. Rev. B* 54 (1996) 17647.
46. D.P. Datta and T.K. Chini, *Phys. Rev. B* 69 (2004) 235313.
47. G. Carter and V. Vishnyakov, *Surf. Interface Anal.* 23 (1995) 514.
48. D.P. Datta and T.K. Chini, *Phys. Rev. B* 76 (2007) 075323.

49. T.K. Chini, D.P. Datta, and S.R. Bhattacharyya, *J. Phys.: Condens. Matter* 21 (2009) 224004.
50. H. Gnaser. *Low-energy ion irradiation of solid surfaces*. in *Low-energy ion irradiation of solid surfaces/Hubert Gnaser*. Berlin; New York: Springer, c1999. 1999.
51. P.J. Schultz, C. Jagadish, M. Ridgway, R. Elliman, and J. Williams, *Phys. Rev. B* 44 (1991) 9118.
52. T. Kumar, A. Kumar, and D. Kanjilal, *Appl. Phys. Lett.* 103 (2013) 131604.
53. P. Campbell and M.A. Green, *J. Appl. Phys.* 62 (1987) 243.
54. K. Bum Sung, L. Don Hee, K. Sun Hee, A. Guk-Hwan, L. Kun-Jae, V.M. Nosang, and C. Yong-Ho, *J. Am. Ceram. Soc.* 92 (2009) 2415.
55. J.S. Yoo, I.O. Parm, U. Gangopadhyay, K. Kim, S.K. Dhungel, D. Mangalaraj, and J. Yi, *Sol. Energy Mat. Sol. C.* 90 (2006) 3085.
56. J. Zhao, A. Wang, M.A. Green, and F. Ferrazza, *Appl. Phys. Lett.* 73 (1998) 1991.

CHAPTER 2

2 Experimental

2.1 Introduction

The experimental studies presented in this thesis covers ion irradiation induced morphological evolution of Si surface and corresponding microstructural changes. Ion irradiation experiments were carried out in an electron cyclotron resonance (ECR) ion source based ion beam facilities [1] installed at Inter-University Accelerator Centre (IUAC), New Delhi and at ITN, Portugal. The topography of the ion-bombarded samples was probed by atomic force microscopy (AFM). Corresponding changes in microstructural, compositional, and vibrational properties of Si were investigated by using crosssectional transmission electron microscopy (XTEM), energy dispersive x-ray spectroscopy (EDS), Rutherford Backscattering Spectrometry (RBS) and micro-Raman spectroscopy. In this chapter, we briefly introduce the basic principles of these experimental techniques and describe the instruments.

2.2 Ion Implantation

Ion-beam processing of materials results from the introduction of atoms into the surface layer of a solid substrate by bombardment of the solid with ions in the electron-volt to mega-electron-volt energy range. The solid state aspects are particularly broad because of the range of physical properties that are sensitive to the presence of a trace amount of foreign atoms. Mechanical (strain/stress), electrical, optical, and magnetic properties are all affected and, indeed, may even be dominated by the presence of such foreign atoms. Moreover, process like ion-beam mixing, ion induced phase transformation, and ion-beam assisted deposition

trigger the synthesis of novel materials for potential applications. Ion implantation is routinely used in semiconductor industry for doping and making large number of devices in very large scale integrated (VLSI) technology.

2.3 Ion Implanter

Experimental studies on the interaction of energetic particles with materials need a steady supply of well-focused contamination-free ion-beam. The requirements over type of ion-species, -current, and -energy range depend upon specific applications and vary over a wide range. A class of ion accelerators has evolved to meet such range of requirements on the ion current or ion energy which is in general referred to as ion implanters. The design of the components of implanters varies with the energy range of operation and producible ion current. However, all the implanters consists of some basic components: (a) an ion source to provide a steady supply of ion-beam of desired species, (b) high voltage electrodes which extract the ions from the ion source and accelerate in accelerating tube to desired energy, (c) a magnetic analyzer to separate the contaminants as well as isotopes present in the extracted ion-beam from the required ion species, and (d) a target chamber with arrangements for target manipulation [2] apparatus to measure the beam current.

Apart from these four primary components, electric or magnetic quadrupole lenses are also parts of an implanter system which ensure focusing of the ion-beam on the target. In addition, for homogenous bombardment of ions over a large area (compared to beam size), implanters are equipped with magnetic or electrostatic scanning arrangement to sweep the beam over the sample in two mutually perpendicular directions. High vacuum throughout the beam line is another important pre-requisite to have a stable and contamination-free ion-beam. Therefore, different pumps like rotary pump (to achieve the vacuum of order 10^{-2} mbar) and turbo molecular pumps (to achieve the vacuum of order 10^{-8} mbar) are employed in the beam line as well as the experimental chamber.

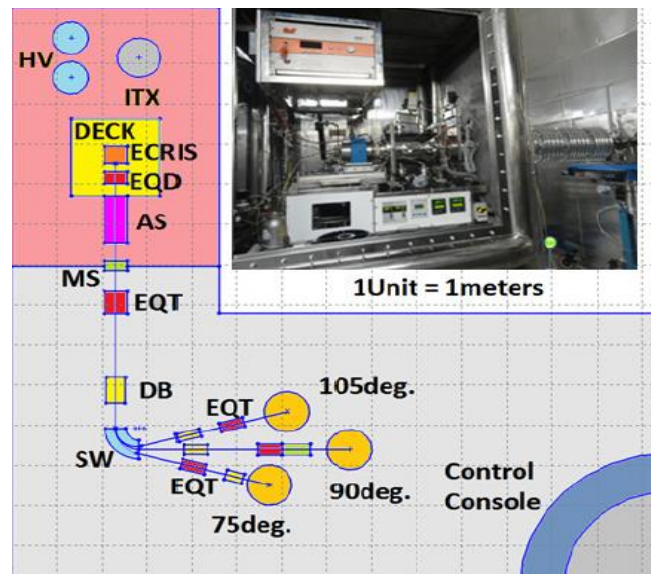
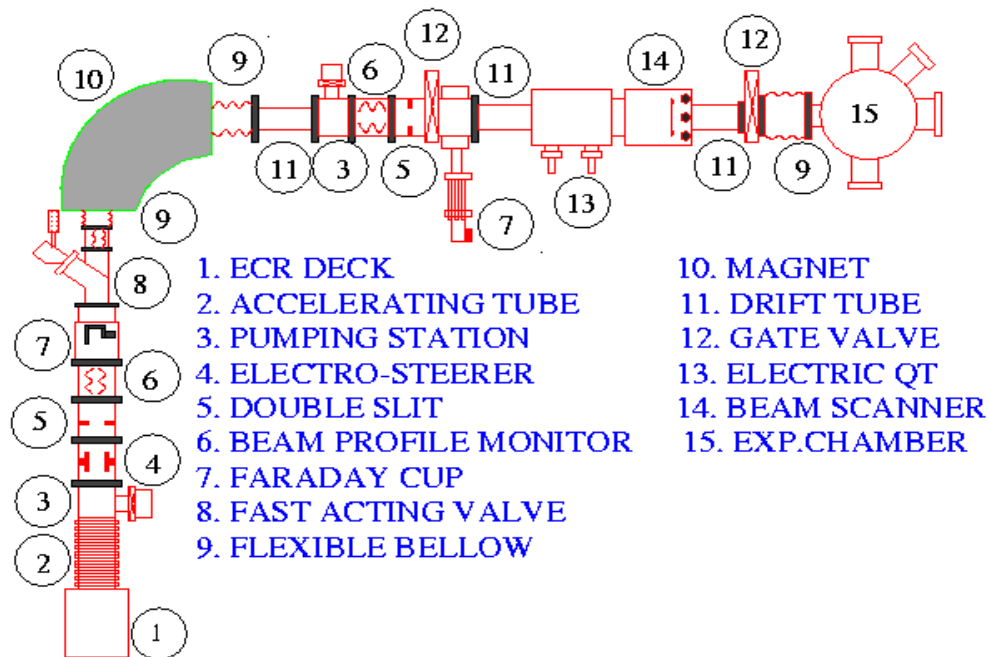


Figure 2.1: Schematic layout of the ECR source based ion-beam facility at IUAC, New Delhi. Inset is a side view of the ion source. For our experiments, beam line at 90° was used (Courtesy [3,4]). ECRIS: Electron Cyclotron Resonance Ion Source, AS: Accelerating Section, SW: Switching Magnet, EQD(T): Electrostatic Quadrupole (Triplet). Similar facility ITN, Portugal was also used.

2.3.1 Low energy ion beam facility (LEIBF) at IUAC

The LEIBF facility at IUAC is specially designed for producing 15 keV to 400 keV ion beams (for singly charged ions) with ion current in the range of 0.1-20 micro-ampere (μA). A schematic diagram of LEIBF in IUAC is shown in Fig. 2.1. The facility consists of an

Electron Cyclotron Resonance ion source (ECRIS), 400 kV accelerating column and an analyzing-cum-switching magnet with three beamline at 75°, 90° and 105°. The ions from the ECR source are typically extracted at 15 kV which are further accelerated to 400 kV by the accelerating column (AC). The analyzing cum switching magnet has been designed for mass separation and to throw the beam into a particular beam line. The beam is further focused on the sample surface using electrostatic quadrupole triplet [3]. This accelerator produces ion beams of gaseous ions. Irradiation of Si samples to low ion fluences (up to 10^{18} ions cm^{-2}) was performed in this implanter, in the 90° beamline. However, irradiation of the sample to higher fluences ($\geq 10^{18}$ ions cm^{-2}) were carried out using the similar setup of ITN, Portugal. Parts of LEIBF are briefly described below.

2.3.2 Ion source

The ion source at both places is a Nanogan type ECR ion source (from Panteknik, France). It is based on a permanent magnet (NdFeB) based design for radial and axial confinement of the plasma [4]. The power from a 10 GHz ultra high frequency (UHF) travelling wave tube (TWT) amplifier is transmitted to the source through a rectangular wave guide which is coupled to the plasma using co-axial coupling. The ECR ion source, along with all its peripheral electronics, UHF transmitter and vacuum components placed on a 400 kV high voltage (HV) platform, provides multiply charged positive ions with energies ranging from a few keV to a few MeV.

2.3.3 Analyzing-cum-switching magnet

The analyzing magnet has been specially designed for mass and isotope analysis of the accelerated beam and switching the ion-beam to one of the three beam lines at 75°, 90° and 105° with respect to the beam entering port to the analyzing magnet. The object point of the magnet is ~5.0 meters away from the source. To transport multiply charged beams over such a long distance from the source, electrostatic doublet (EQD) and triplet (EQT) focusing

magnets have been used before and after the accelerating column. The magnet can provide maximum magnetic field of 1.5 T and has a bending radius of 529 mm, entrance angle 29.1°, and exit angle 30.6°. The entrance and exit edge angles for the three beam lines were optimized to obtain double focus in all beam lines.

2.3.4 Experimental station and accessories

A Faraday cup and a beam profile monitor (BPM) are placed before the target chamber to measure the beam current and the beam profile, respectively. A two-dimensional scanner before the chamber scans the beam along horizontal and vertical directions (x,y -plane). Two kind of sample mounting ladders were used for the experimental studies presented in this thesis: (i) a stainless steel ladder with four faces for sample mounting and (ii) a copper ladder with two sides for sample mounting which is specially designed for oblique ion irradiation. At a time 4 to 5 samples were mounted on each faces of ladder one. Using the vertical movement of the ladder, samples were brought to the beam scan area for irradiation. In our experiments, we have used sacrificial Si wafers belonging to the same lot as the sample to avoid any impurity from any other source like the sample holder.

The sample ladder was placed in the middle of a cylindrical suppressor. Suppression voltages (dc) from 0-300V dc were applied to suppress the secondary electrons which comes out from the sample during irradiation. There was also a provision to measure the beam current at the sample ladder through a connection to the current integrator.

2.4 Characterization Technique

2.4.1 Atomic force microscopy (AFM)

AFM is a microscopic technique which is applicable to all types of materials– insulators, semiconductors as well as conductors. This technique measures nanoscale variation in the surface topography by measuring the deflection of a tip (10-20 nm in diameter) attached to the end of a cantilever, as the tip is brought to a close proximity of the surface to be probed.

A schematic diagram of the working principle of AFM is shown in Fig. 2.2(a). A laser beam is focused on the tip of a highly reflective cantilever head such that the laser beam is reflected on to the surface of a position-sensitive photo-detector. The sample is scanned underneath the tip via a piezoelectric scanner made of PZT (Lead Zirconium Titanate). A feedback loop is used to maintain either a constant deflection (contact mode) or oscillatory amplitude (tapping mode) of the cantilever, as the tip is scanned over the sample surface. The force associated with the tip and the sample during scanning is the inter-atomic Van der Waals force. The dependence of this Van der Waals force upon the distance between the tip and the sample is shown in Fig. 2.2(b), where three regimes of tip-surface distance are labeled: the contact regime, the non-contact regime, and the tapping regime.

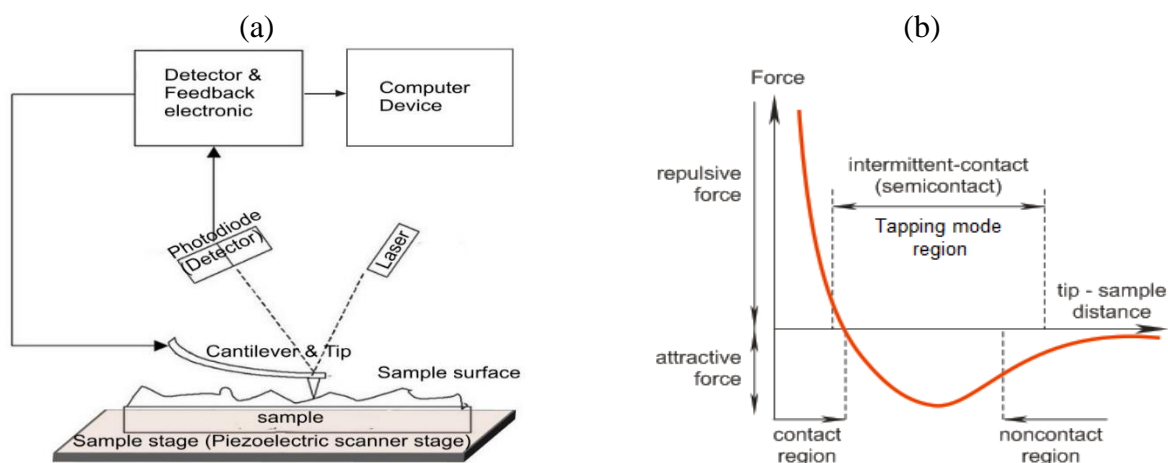


Figure 2.2: (a) A schematic diagram showing the working principle of AFM, (b) Van der Waals force as a function of tip to surface distance.

(i) Contact or repulsive mode: In contact-AFM mode, also known as repulsive mode (due to the repulsive nature of the force in this regime), an AFM tip makes soft ‘physical contact’ with the sample by bringing the tip very close to a surface (a few angstroms). The tip is attached to the end of a cantilever with a low spring constant. As the scanner gently traces the tip across the sample (or the sample under the tip), the contact force causes the cantilever to bend to accommodate changes in the topography. This mode is usually used for hard crystalline surface because strong force involved may cause deformation of soft surfaces.

(ii) Non-contact or attractive mode: Non-contact mode AFM is one of several vibrating cantilever techniques in which an AFM cantilever vibrates near the surface of the sample keeping the tip-to-surface distance in the range of tens to hundreds of angstroms. The major advantage of the non-contact mode AFM is its truly non-invasive character.

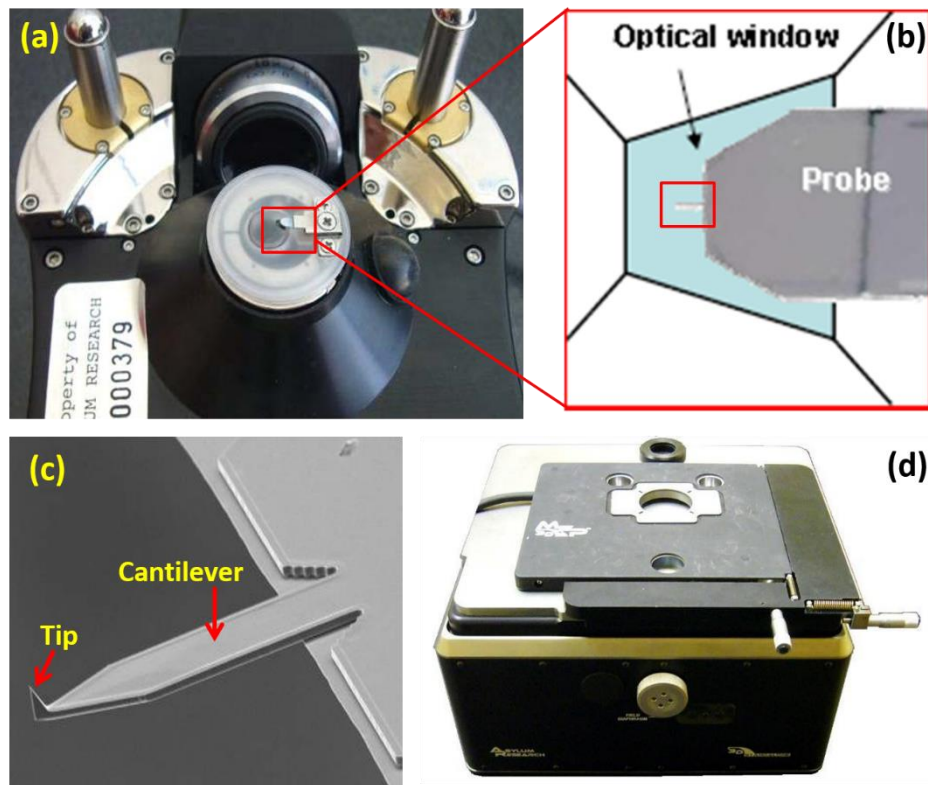


Figure 2.3: (a) the AFM head, (b) Schematic diagram of the probe, (c) SEM image of the cantilever along with tip, and (d) base of the AFM.

(iii) Tapping Mode: This mode is also known as intermittent-contact mode. In this case the vibrating cantilever is brought closer to the sample surface so that it just barely hits or ‘taps’ the sample. This mode is a compromise between the contact and the non-contact mode where the cantilever is made to oscillate with or near to the resonant frequency using a piezoelectric crystal so that the tip remains very close to the sample for a short time and then goes far away for a short time. As the oscillating cantilever begins to contact the surface intermittently, the cantilever oscillation necessarily reduces due to energy loss caused by the tip in contacting the surface. The reduction in the oscillation amplitude is used to identify and measure the surface features. This mode allows one to scan soft adsorbates on a substrate with better

resolution than in the non-contact mode but with a small interaction (and consequently less modification of the samples) between the tip and adsorbate as in the non-contact mode. Thus, this tapping mode overcomes certain problems associated with conventional AFM scanning method viz. friction, adhesion, electrostatic forces, and other difficulties.

AFM System and measurements

All images in this thesis were acquired with the help of an MFP-3D AFM from Asylum Research, USA in the tapping mode by using silicon nitride tip. This AFM is installed at the SUNAG Laboratory at Institute of Physics, Bhubaneswar. Among many advantages of this AFM, an important one is its large area-high precision facility because of which we could scan areas up to $90 \times 90 \mu\text{m}^2$ with very high accuracy. Fig. 2.3 shows different parts of AFM. Fig. 2.3(a) shows the cantilever head. The middle part of this head is zoomed in Fig. 2.3(b) and shows the probe assembly in the optical window. An SEM image of the tip is shown in Fig. 2.3(c). In Fig. 2.3(d) the base part of the AFM shown on which the head of AFM is placed. Initially, the head is used to manually bring the tip near the surface. In the next stage, close approach to the surface (separation between tip to sample remain 80 nm) is controlled by software to prevent the damage of tip. A xy motorized sample stage attached with the AFM which helps in precise positioning of a sample and checking large scale uniformity in surface morphology.

2.4.2 Transmission electron microscopy (TEM)

TEM observation can produce magnified images of the sample down to the atomic scale. For this purpose, a high energy (hundreds of keV) electron beam is allowed to pass through a very thin sample specimen. Electrons accelerated to hundreds of keV have wavelengths lower than average inter-atomic separation. At an energy of 200 keV, for instance, electrons have a wavelength of 0.025 Å. However, the resolution of a TEM is limited, by the aberrations inherent in electromagnetic lenses, to about 1 to 2 Å and hence can reveal detail down to

atomic scale. In addition, a TEM also produces diffraction patterns which reveal the crystalline nature of the specimen. Electron diffraction from a crystalline lattice can be described as a kinematic scattering process that meets the wave reinforcement and interference condition given in the Bragg equation. The patterns are formed by diffraction of an electron beam transmitted through the thin specimen. The electron diffraction yields spot patterns from single crystal, ring patterns from randomly oriented crystallites, and superimposed ring and spot patterns from larger-grain polycrystalline films.

Sample preparation for TEM

Due to the strong interaction between electrons with matter, the specimens have to be rather thin (< 100 nm) for TEM investigations. Thus, bulk materials have to be thinned to make them transparent to the electron beam. This is done either by simply crushing them and subsequently depositing some fragments on a Cu grid coated with carbon foil or by mechanical grinding and ion milling [5]. The following steps like disc cutting, mechanical polishing, dimple grinding, and ion-beam etching were adopted sequentially for all cross-sectional TEM sample preparation in the present studies.

2.4.3 Energy dispersive X-ray spectrometry (EDS)

Energy-dispersive X-ray spectroscopy (EDS or EDX) is an analytical technique used for the elemental analysis or chemical characterization of a sample through detection of characteristic x-rays emitted from the sample. When energetic electrons hit any material, ejection of an electron from it due to interaction with the incident electron results in an ion in the excited state. The de-excitation of the excited ion can take place in most cases in a series of transformations in each of which an electron from an outer shell transits into a vacancy in the inner shell. Each such “drop” results in loss of a specific amount of energy. This energy is given up in the form of X-rays in case of high energy transition involving inner shells. The energy of such X-ray radiation is a characteristic of a particular element from which it comes.

For this reason, this X-radiation is called characteristic X-rays. The characteristic X-ray lines are named after the electron shells associated with the transition corresponding to the X-ray line. If an electron vacancy occurs in the K-shell (most inner shell) and an electron from the L-shell (second most inner shell) fills the vacancy the emitted radiation due to this transition is called K_{α} x-ray. X-ray line associated with M-shell (third most inner shell) to K-shell is called K_{β} , N-shell (outer shell or fourth most inner shell) to K-shell is called K_{γ} and so on. Because of the complexity of electronic structure, the nomenclature becomes more complex when the initial vacancy occurs in higher energy shells. Microanalysis of samples is generally concerned with K, L, and M series X-rays. Apart from the characteristic X-ray lines, the deceleration of primary electron by the coulomb field of the atomic nucleus causes the emission of energy lost by the electrons in the form of X-ray. This radiation is called Bremsstrahlung. The primary electrons may lose any amount of energy in the interaction, and thus, the energy distribution of emitted X-ray is continuous. To stimulate the emission of characteristic X-rays from a specimen, a high-energy beam of charged particles such as electrons is focused into the sample being studied and sample release an X-ray. Unique atomic structure for each element emits a unique set of peaks on its X-ray spectrum. As the energy of the X-rays are characteristic of the difference in energy between the two shells and of the atomic structure of the element from which they were emitted, this allows the elemental composition of the specimen to be measured. The number and energy of the X-rays emitted from the specimen can be measured by an energy-dispersive spectrometer.

In our studies we used the EDS system attached to a 200 kV TEM. A high energy electron beam (of spot size 20 nm at specimen) hits the specimen and the resulting elemental X-ray spectra were obtained by using a external detector [Lithium drifted Si detector Si(Li)]. Several peaks in the spectra revealed the elemental composition of the target. Area under the peak provides the percentage of an element at that region of specimen.

2.4.4 Rutherford backscattering spectrometry (RBS)

RBS is one of the most important analytical technique which uses energetic ion-beam. RBS is an attractive option to determine concentration depth distribution of elements in a solid target in a non-destructive way. In the best situation this can be done with a precision of ~5%. RBS is based on collisions between atomic nuclei. It involves measuring the number and energy of ions after being backscattered from the target. With these information, it is possible to determine atomic mass and elemental concentration as a function of depth below the surface [6]. The damage in crystal structure can also be known under special probing geometry. RBS is ideally suited for accurate quantitative analysis of composition, thickness of thin films and for depth profiling of a heavy element in a light substrate in a non-destructive manner. It offers a sensitivity of 10^{11} - 10^{15} at. cm^{-2} and a depth resolution is an average of 5 nm.

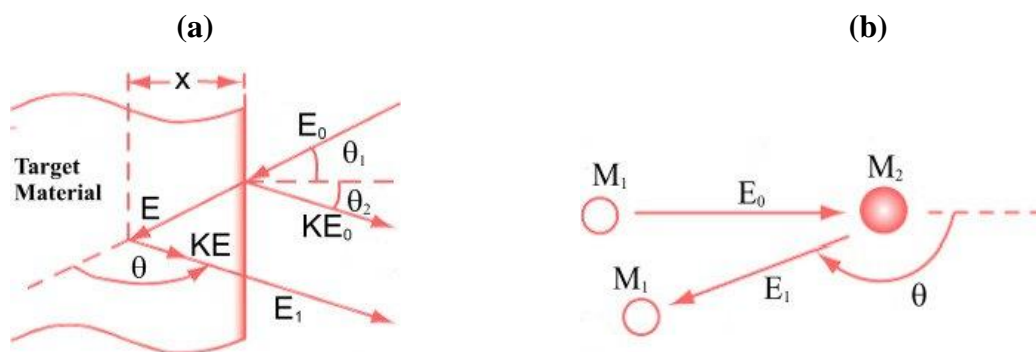


Figure 2.4: (a) Schematic of RBS (b) Schematic presentation of collision of an energetic incident projectile with target atom.

When a solid target is bombarded with a beam of high energy light particle (e.g. a few $\text{keV} < E < \text{few MeV}$), the interaction between the projectile and target atoms can be modeled accurately as an elastic collision using classical physics. A typical MeV ion travelling through a solid will go through many low energy transfer collision with the atoms until it loses its kinetic energy and come to rest of the order of $10 \mu\text{m}$ below the surface. However, a small number of ions will experience nuclear collision and backscatter out of the sample. A schematic of RBS is shown in Fig. 2.4(a). Here, energetic light particles (He^+) with energy E_0 and mass M_1 hit the target at an angle θ_1 with respect to the normal of target surface. The

projectile is backscattered at an angle θ_2 with reduced energy KE_0 . Schematic diagram in Fig. 2.4(b) shows a projectile of energy E_0 and mass M_1 undergoing an elastic collision with a stationary atom of mass M_2 ($M_2 > M_1$) in a target. The relation between energy of the projectile backscattered from the surface with an incident energy is $E_1 = KE_0$. Where, K is the kinematic factor.

$$k = \frac{E_1}{E_0} = \left[\frac{M_1 \cos \theta + (M_2^2 - M_1^2 \sin^2 \theta)^{1/2}}{M_1 + M_2} \right]^2. \quad (2.1)$$

Scattering crosssection is the relative number of projectiles scattered from a target atom into a given solid angle for a given number of incident projectiles. If Q and dQ are the total number of projectiles that hit the target and backscattered projectiles detected by the detector at a solid angle Ω , respectively, the differential scattering crosssection for an elastic collision between two atoms (in the laboratory frame) is given by Rutherford's formula:

$$\frac{d\sigma}{d\Omega} = \left[\frac{Z_1 Z_2 e^2}{4E_0} \right]^2 \frac{4}{\sin^4 \theta} \frac{\left[\left[1 - \left(\frac{M_1}{M_2} \sin \theta \right)^2 \right]^{1/2} + \cos \theta \right]^2}{\left[1 - \left(\frac{M_1}{M_2} \sin \theta \right)^2 \right]^{1/2}}, \quad (2.2)$$

where, Z_1 and Z_2 are the atomic numbers of the projectile and target atom, respectively. The scattering crosssection is roughly proportional to the atomic number of the target atom, as seen in Eq. 2.2. This means RBS has a much greater sensitivity detecting heavy elements than lighter elements. However, the ability of RBS to distinguish between elements with similar atomic mass is much greater for light elements than for heavy elements. Due to these sensitivity concerns, RBS is better suited to analyze certain combination of elements than others. Based on these above two equations, many simulation packages or algorithms are available to interpret experimental data. In this work, we have used RUMP software [7] to simulate the experimental RBS spectra and know the composition as a function of depth. A comparative study was performed for Si sample exposed to Ar-ions at different fluence.

RBS setup

The instrumentation for RBS experiments can be broadly divided into three parts: accelerator, energy analyzer, and target chamber as shown in Fig. 2.5. Helium ions were accelerated using an accelerator up to energy 1-3 MeV. A collimated beam of He^+ -ions falls on the sample. In the target chamber, a surface barrier detector (SBD) is kept at a very high angle ($\geq 150^\circ$), which is used to detect the backscattered particles. The samples were connected with a current integrator to collect the total number of incident ions that fall on the target. To get the energy related output, signal goes from SBD to energy analyzer. Energy analyzer consists of preamplifier, amplifier, analog-to-digital converter (ADC), and multi-channel analyzer (MCA). Finally the output of MCA is fed to a computer to store the spectrum, which contains channel number along x -axis and number of backscattered particle (yield) per channel along y -axis. The channel numbers are calibrated to the energy values (of backscattered particles) using calibration samples.

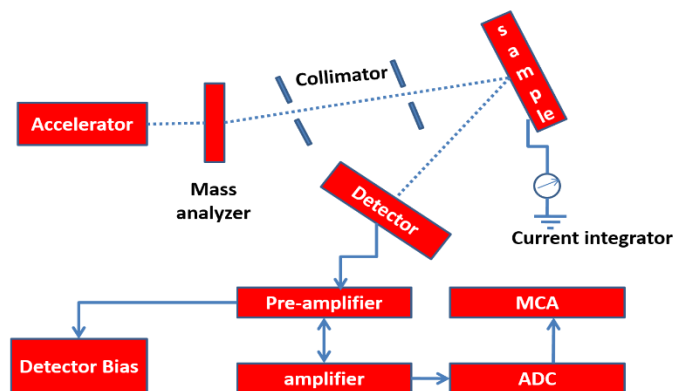


Figure 2.5: A Schematic diagram showing Rutherford backscattering spectroscopy experimental setup. Preamplifier, amplifier, ADC- analog to digital converter, MCA- multi channel analyzer.

2.4.5 Micro-Raman spectroscopy

Raman spectroscopy is a versatile, convenient, non-destructive characterization tool widely used in the field of semiconductors. Since it probes lattice vibrations, which are sensitive to internal and external perturbations such as the changes in the vibrational frequencies induced by the microstructures and/or by the strain in the lattice, it can be used to study the

compositional and microstructural analysis. Micro-Raman spectroscopy, where the light of the exciting laser is focused on the sample through a microscope, is especially very useful for microelectronics devices with small dimensions as it allows investigations with micron-order spatial resolution.

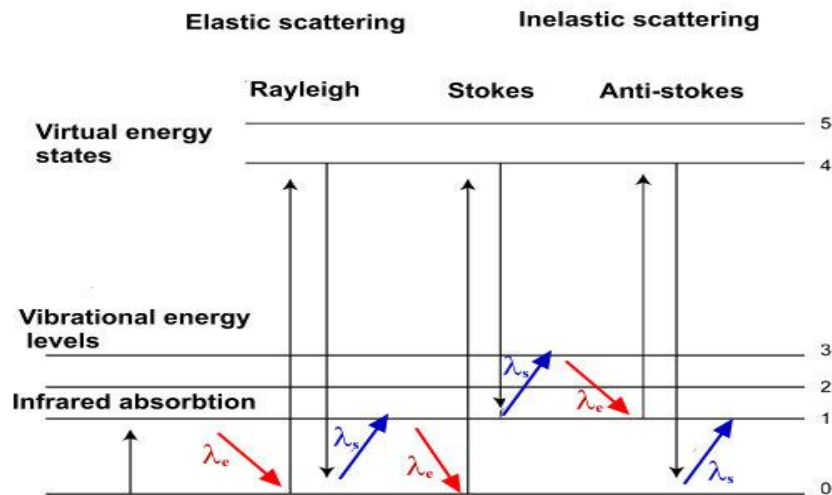


Figure 2.6: Energy level diagram demonstrating elastic (Rayleigh) and inelastic (Stokes and Anti-stokes) scattering of photons. Excitation light and scattered light are shown here by λ_e and λ_s , respectively.

Fig. 2.6 shows the vibration energy level diagram of molecules where process of generation of elastically and inelastically scattered photon has been shown. Incident photons of wavelength (λ_e) excite a ground level electron to a virtual energy level. If this electron relaxes back to its initial level by scattering a photon of wavelength (λ_s), it is an example of elastic (Rayleigh) scattering. If, instead, the electron decays back to a higher level compared to ground level, the scattering is called as inelastic scattering. Inelastic scattering is used to probe the internal structure of molecules and crystals in Raman spectroscopy [8]. Majority of scattered photons have the same frequency as incident photons (Rayleigh scattering electrons). A very small fraction of photons (approximately 1 in 10^7 of incident photons) has their frequencies shifted from the incident photons by energies of molecular vibrations, and the shift is known as a Raman Shift. This Raman shift is an intrinsic property of the sample as the magnitude of the shift is independent of the excitation frequency. Most of the inelastically

scattered photons are shifted to longer wavelengths (known as Stokes shift) because of higher density of electrons at the lowest energy level at room temperature. As a result, small portion of inelastically scattered photons are shifted to lower wavelengths (known as Anti-stokes shift). Both of these Stokes and anti-stokes shift have equal distance from the Rayleigh scattered photons. Stokes shift is taken into consideration in Raman spectroscopy because of their high intensity.

In our studies presented in this thesis, micro-Raman scattering measurements were performed in the backscattering geometry (180°) at room temperature by using an in-Via Renishaw micro-Raman spectrometer. The excitation sources were lasers of wavelengths 325 nm, 488 nm, 514.5 nm, 532 nm, and 785 nm, respectively, and the detection system was a Peltier cooled charged coupled (CCD) device [9].

2.4.6 Contact angle measurement

The contact angle, δ , is the angle between a tangent drawn on the drop's surface at the resting or contact point and a tangent to the supporting surface. Contact angles describe the shape of a liquid drop on a solid surface. The shape of the drop informs about the nature of chemical bonding between the liquid and the surface. This bonding determines the wettability and adhesion. The contact angle is the best wettability measurement method when pure fluids and artificial cores are used because there is no possibility of surfactants or other compounds altering the wettability.

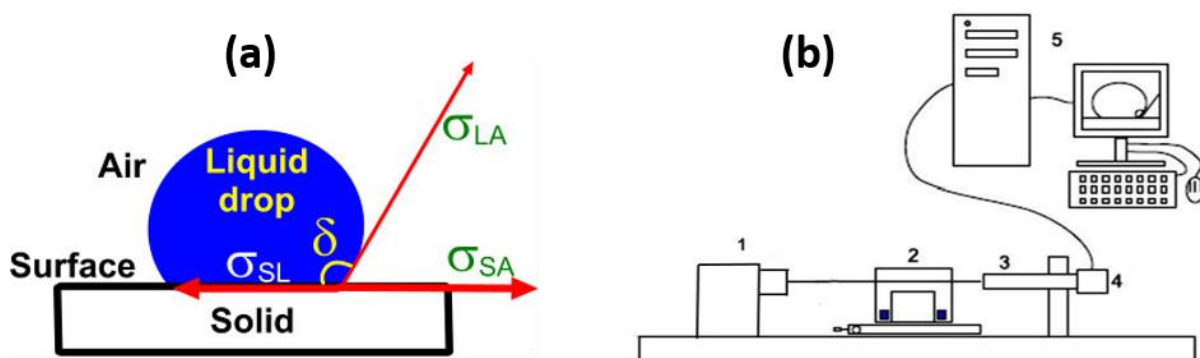


Figure 2.7: Schematic diagram of (a) Contact angle, δ and (b) its measurement technique.

Contact angle, δ , is defined geometrically as the angle formed by a liquid at the three phase boundary where a liquid, gas and solid surfaces intersect, as shown above. The static contact angle between a liquid drop and a smooth solid surface is given by the Young's [10] Equation (Eq. 2.3) which, essentially, describes the balance between the interfacial tensions at the solid-liquid-air interface.

$$\sigma_{LA} \cos \delta = \sigma_{SA} - \sigma_{SL} . \quad (2.3)$$

Here, σ_{LA} = Interfacial energy between liquid and air, σ_{SA} = Interfacial energy between solid and air, σ_{SL} = Interfacial energy between solid and liquid, and δ is the measured contact angle. If $\delta < 90^\circ$, the liquid is said to wet the solid, with a contact angle of zero representing complete wetting. If the liquid is water, the solid surface is called hydrophilic. If $\delta > 90^\circ$ it is said to be non-wetting, and in case of water, the surface is known as hydrophobic.

A schematic diagram of the instrument used to measure the contact angle is shown in Fig. 2.7(b). The instrument consists of a source of illumination (labeled '1' Fig. 2.7(b)), the stage to place the drops ('2' in Fig. 2.7(b)) and a microscope coupled to CCD camera ('4' in Fig. 2.7(b)). Köhler illumination is used in contact angle measurement as it provides a beam of light of equal intensity. This helps in producing drop images with a good contrast between the drop and the background. The stage consists of an X-Y translation stage on which a labjack is mounted which enables X-Y-Z movement. A long distance microscope ('3' in Fig. 2.7(b)) is coupled to a CCD camera. The camera is connected to computer ('5' in Fig. 2.7(b)) and the images are captured using SCA, a software that measures the contact angle. Contact angles reported in this thesis were measured by using the system "OCA 15 EC" (Dataphysics). This system is equipped with a control syringe by which one can put a liquid drop of desired volume on a sample.

Bibliography

1. P. Kumar, G. Rodrigues, U. Rao, C. Safvan, D. Kanjilal, and A. Roy, *Pramana* 59 (2002) 805.
2. D.P. Datta, *Modification of Silicon Surface under medium energy heavy ion bombardment*. 2008, Saha Institute of Nuclear Physics: Kolkata.
3. A. Mandal, D. Kanjilal, S. Kumar, and G.O. Rodrigues. *ION OPTICAL DESIGN OF LOW ENERGY ION BEAM FACILITY AT IUAC*.
4. D. Kanjilal, G. Rodrigues, U. Rao, C. Safvan, P. Kumar, A. Roy, and G. Mehta. *Ecr Ion Source Based Low Energy Ion Beam Facility*.
5. B. Satpati, *Ion irradiation effect in nanostructures grown on semiconductor surfaces*. 2005, Institute of Physics: Bhubaneswar, India.
6. W.-K. Chu, J.W. Mayer, and M.A. Nicolet, *Backscattering spectrometry*. 1978: Academic Press.
7. CGS, *RUMP: A simulation package for backscattering spectra for ion beam analysis with MeV ions*, J.W. Mayer, et al., Editors.: Cornell University.
8. I.R. Lewis and H. Edwards, *Handbook of Raman spectroscopy: from the research laboratory to the process line*. 2001: CRC Press.
9. J.R. Janesick, *Scientific Charge-coupled Devices*. 2001: Society of Photo Optical.
10. T. Young, *Philos. Trans. R. Soc. London* 95 (1805) 65.

CHAPTER 3

3 Theoretical Background

3.1 Introduction

Ion irradiation can lead to smoothening or roughening as well as formation of patterns on target surface depending upon the experimental conditions. The roughness or smoothness of surface is theoretically described by fluctuations in surface height. In this chapter, we will first briefly introduce statistical methods used for characterization of surfaces. Afterwards, we will outline the theoretical models developed for understanding surface evolution under ion bombardment.

3.2 Statistical methods for characterization of surface

In a continuum description, a surface can be described by a height function, $h(r) \equiv h(x,y)$ where the height is measured from a fixed reference frame and $r = (x,y)$ is any point on the surface. The statistical quantities which are used to characterize the surface is defined through the variation of $h(r)$ over the surface as described below.

3.2.1 Average surface height

The average or mean surface height, \bar{h} , is the simplest characterization of a surface. It is defined as

$$\bar{h} = \frac{1}{L^2} \int_{-L/2}^{L/2} \int_{-L/2}^{L/2} h(x,y) dx dy, \quad (3.1)$$

where the surface height is measured over a surface area of dimension $L \times L$.

3.2.2 *rms* roughness

This quantity determines the fluctuation in surface height with respect to the mean height. It is defined as

$$w = \frac{1}{L} \left[\int_{-L/2}^{L/2} \int_{-L/2}^{L/2} [h(x, y) - \bar{h}]^2 dx dy \right]^{\frac{1}{2}}. \quad (3.2)$$

3.2.3 Roughness exponent (α)

The *rms* roughness w in general depends upon the length scale of observation L . The dependence of w on L can be quantified as

$$\begin{aligned} w(L) &\sim L^\alpha \text{ for } L < L_x, \\ &\sim w_{sat} \text{ for } L \gg L_x, \\ w_{sat}(L, t) &\sim L^\alpha \text{ for } t \gg t_x, \end{aligned} \quad (3.3)$$

The exponent α is termed as roughness exponent and w_{sat} is a constant. L_x defines the length scale above which w becomes independent of L .

3.2.4 Correlation functions and correlation length

The connection or correlation of spatially separated surface points can be determined by the autocorrelation or height-height correlation function. The correlation length expresses the distance up to which height of two surface points can be considered to be correlated

I. Auto correlation: The auto-correlation function, $R(r)$ is defined as

$$R(r) = \frac{1}{w^2} \frac{1}{L^2} \int_{-L/2}^{L/2} \int_{-L/2}^{L/2} [\{h(x, y) - \bar{h}\} \{h(x + x', y + y') - \bar{h}\}] dx dy, \quad (3.4)$$

where r is the spatial separation between two arbitrary surface points, $r_1=(x,y)$ and $r_2=(x+x',y+y')$. For a truly random rough surface, $R(r)$ decays to zero with increasing r .

The decay rate depends on the randomness of the surface. The lateral correlation length, ξ , is defined as a length scale over which the magnitude of $R(r)$ decreases to $1/e$ of its value at $r=0$, i.e, $R(\xi)=(1/e) R(0)$ spatial length over the surface at which this autocorrelation function drops down to $1/e$. If the distance r between two surface points is within lateral correlation length $r < \xi$, the heights at these two points can be considered to be correlated. If the distance r between two points is greater than ξ the height at these two points is considered to be independent of each other.

II. Height-height correlation: Height-height correlation function, $G(r)$, is defined as

$$G(r) = \frac{1}{L^2} \int_{-L/2}^{L/2} \int_{-L/2}^{L/2} [h(x+x', y+y') - h(x, y)]^2 dx dy. \quad (3.5)$$

For a random rough surface, the height-height correlation function has the form:

$$\begin{aligned} G(r) &\sim r^{2\alpha} \text{ for } r \ll \xi, \\ &\sim 2w^2 \text{ for } r \gg \xi. \end{aligned} \quad (3.6)$$

$R(r)$ and $G(r)$ are related by

$$G(r) = 2w^2[1 - R(r)]. \quad (3.7)$$

Here, α is the roughness exponent (described in the next section).

III. System correlation length: A periodically varying surface is characterized by the wavelength, l , of the periodic patterns. The system correlation length, ζ , shows the regularity in the distribution of the patterns over the surfaces. When the surface patterns are regularly arranged over a surface area of lateral dimension much higher than the length scale of pattern separation l , the system correlation length ζ is much higher than l . On the other hand, ζ is comparable to l when patterns are confined within surface area comparable to l . If, $\zeta \gg l$, $G(r)$ and $R(r)$ exhibit regular periodic oscillations at a length scale $r \gg \zeta$. However, when ζ is comparable to l , the oscillations become irregular and $G(r)$ approaches the form of Eq. 3.6. Height-height correlation function for a mounded surface with system correlation length ζ is proposed by Zhao *et al.* [1]:

$$\begin{aligned} G(r) &= 2w^2 \left[1 - e^{-\left(\frac{r}{\zeta}\right)^{2\alpha}} \cos\left(\frac{2\pi r}{l}\right) \right] \quad \text{for } 1 + 1 \text{ dimension,} \\ &= 2w^2 \left[1 - e^{-\left(\frac{r}{\zeta}\right)^{2\alpha}} J_0\left(\frac{2\pi r}{l}\right) \right] \quad \text{for } 2 + 1 \text{ dimension.} \end{aligned} \quad (3.8)$$

Here, $J_0(r)$ is the zeroth-order Bessel Function. Autocorrelation function in the form of system correlation length may be extracted by using Eqs. 3.7 and 3.8.

3.2.5 Power spectrum

So far we have discussed the statistical properties of a rough surface in real space. Equivalent to real space characterization, a surface can also be characterized in the reciprocal space by a function called the power spectrum or structure factor of the surface. Power spectrum, $S(k)$, is the square of the Fourier transformation of the surface height profile $h(x,y)$ and expressed as

$$S(k) = \frac{1}{L^2} \left| \int_{-L/2}^{L/2} \int_{-L/2}^{L/2} [h(x+x', y+y') - h(x,y)] e^{-i(k_x x + k_y y)} dx dy \right|^2. \quad (3.9)$$

If the surface height fluctuation is periodic with a repetition length, l , the periodicity will be reflected in the power spectrum $S(k)$ as a peak at the wave number $k = 2\pi/l$.

3.2.6 Gradient angle

A distribution of the gradient angles of a surface gives a quantitative measurement of surface slopes. It is particularly useful for analysis of patterned surfaces. The gradient angles are usually calculated along a particular direction on the surface. In case of ripple patterned surfaces, for instance, gradient angles can be defined as

$$f(\alpha) = \tan^{-1} \left(\frac{dh}{dx} \right). \quad (3.10)$$

Where, the x direction can be parallel or perpendicular to the ripple patterns.

In our studies presented in this thesis, AFM images of 512×512 pixels and acquired over an area of $10 \times 10 \mu\text{m}^2$, were used to analyze the distribution of gradient angles in a direction parallel to the direction of projection of the incident beam onto the surface (which is perpendicular to ripple patterns observed in our studies).

Measurement of ripple wavelength from AFM images

For our ripple patterned Si samples, the ripple wavelengths were determined from the autocorrelation of the AFM images. The autocorrelation image is the 2-dimensional autocorrelation function as defined in Eq. 3.4. For the ripple patterned surfaces, the autocorrelation images show the bright strips on the two sides of a central line. The distance

of the nearest bright region from the central bright region gives the wavelength of the ripple pattern.

3.2.7 Numerical simulation program

The MATLAB (Matrix Laboratory) [2] software was used for numerical calculations based upon present theoretical models of ion-induced pattern evolution and for simulation of experimentally observed pattern formation under ion irradiation. For simulation of the temporal evolution of surfaces during erosion/growth described by the continuum equations (Eq. 3.23) the “RDCalculate” program in MATLAB uses a simple finite difference method in an Euler scheme with cyclic boundary conditions [3]. After converting the continuum equation into a difference equation using equidistant spatial and temporal discretizations, the equation can be integrated effectively by matrix multiplications. By using the “sparse” matrices in MATLAB the matrix multiplications are performed very fast and no further sophisticated algorithms are needed [4].

In the Euler scheme, the temporal ($\partial h/\partial t$) and spatial ($\partial^n h/\partial r^n$) differentials are substituted by differences $\Delta h/\Delta t$ and $(\Delta h)^n/(\Delta r)^n$, respectively. In this way, the partial differential equation turns into a difference equation, which can easily be integrated:

$$h_{i+1} = h_i + \Delta t \sum_{k=1}^n \left(a_k \frac{(\Delta h)^k}{(\Delta x)^k} + b_k \frac{(\Delta h)^k}{(\Delta y)^k} \right) + \sum_{l,m} c_{lm} \left(\frac{\Delta h}{\Delta x} \right)^l \left(\frac{\Delta h}{\Delta x} \right)^m. \quad (3.11)$$

In MATLAB, the sum on the right-hand side can be calculated very effectively in a matrix formalism where the differentiations are matrix multiplications. In addition, the cyclic boundary conditions are incorporated by including the corresponding matrix elements. For instance, the first spatial derivatives, $\partial h/\partial x$ and $\partial h/\partial y$, are replaced by $(h_{i+1} - h_i)/\Delta x$ and $(h_{i+1} - h_i)/\Delta y$, respectively and implemented by multiplications with

$$grad = \begin{bmatrix} -1 & 1 & 0 & 0 & 0 \\ 0 & -1 & 1 & 0 & 0 \\ 0 & 0 & -1 & 1 & 0 \\ 0 & 0 & 0 & -1 & 1 \\ 1 & 0 & 0 & 0 & -1 \end{bmatrix}. \quad (3.12)$$

By using the “sparse” matrices in MATLAB, the integration becomes very fast, because most of the matrix elements are zero. Using this method the spatial derivatives in the x - and y -directions are implemented as multiplications with the $grad$ matrix from left, $grad \cdot h$, and from right, $h \cdot grad$, respectively. For the second spatial derivative, a symmetric matrix is used which is equivalent to $grad \cdot grad$ shifted with one index to the left:

$$delta = \begin{bmatrix} -2 & 1 & 0 & 0 & 1 \\ 1 & -2 & 1 & 0 & 0 \\ 0 & 1 & -2 & 1 & 0 \\ 0 & 0 & 1 & -2 & 1 \\ 1 & 0 & 0 & 1 & -2 \end{bmatrix}. \quad (3.13)$$

3.2.8 Statistical parameters for analysis of periodic morphology

In order to understand the nature of the ion-induced surface textures in detail, extensive analysis of AFM images of the ion-patterned surfaces were carried out using the SPIP software [5]. The parameters which we have extracted using SPIP are briefly described below.

(1) Surface texture aspect ratio (*Str*): This is used to identify texture strength. It is defined as the ratio of spatial length of the fastest to slowest decay to correlation (1/e)% of the autocorrelation function, respectively. In principle, the texture aspect ratio has a value between 0 and 1.

(2) Surface texture direction index (*Stdi*): It is a measure of how dominant a direction is. To calculate this parameter, 2-dimensional (2D) AFM image were divided into equal angular subsections in the range from 0° (corresponding to positive x -axis) via 90° (corresponding to y -axis) to 180° (corresponding to negative x -axis) and Fourier’s spectrum of these equal angular subsections of image were calculated. If M is the total number of subsection and A_i is the amplitude sum of corresponding subsection, M_i (where $i= 1,2,\dots,\pi/M$), then *Stdi* is defined as

$$Stdi = \frac{\sum_i A_i}{M \times \text{Max}(A_i)}, \quad (3.14)$$

Stdi varies from 0 to 1, where, a value of *Stdi* close to 1 correspond to isotropic surface and value close to 0 is associated with a directional textured surface.

(3) Surface developed interfacial area ratio (*Sdr*): It expresses the increment of the interfacial surface area relative to the area of projected (flat) 2D plane.

$$Sdr = \frac{\text{texture surface area}-\text{Projected plain area}}{\text{Projected plain area}} \times 100\%, \quad (3.15)$$

The notations used above to describe the quantity are the standard notation in 3D surface metrology and come under the “ISO 25178” [6,7].

3.3 Continuum description of ion bombarded surface evolution

Continuum models describe the surface at a length scale much larger than the atomic scale. The solid surface is assumed to be a continuum of points, described by a surface height function $h(x, y, t)$ measured from laboratory coordinate whose x, y axis are parallel to the initial flat surface and z axis normal to the surface. The first breakthrough on the understanding of development of periodic pattern on ion bombarded surface was due to Bradley and Harper (BH) [8] who used Sigmund’s [9] theory of ion sputtering of an amorphous solid surface. For a slowly undulating surface, BH demonstrated the dependence of sputtering yield on local surface curvature which makes the surface unstable against development of sinusoidal modulations. Competition of the curvature dependent sputter erosion process with the relaxation processes which tend to smooth out the surface results in growth of a range of sinusoidal perturbations on the surface. The fastest growing mode from these sinusoidal perturbations dominates over the other modes and is observed as ripple patterns on the bombarded surface. In the following, we introduce the continuum theories which describe ion-induced surface evolution.

3.3.1 Continuum theory

BH theory assumes that the surface slope is small and use Sigmund theory of sputtering to drive a linear partial differential equation which describes the evolution of surface height h under ion bombardment. Here, we first describe the Sigmund sputtering theory and then briefly introduce the main results of BH theory.

A. Sigmund's theory of sputtering

Sigmund [9] showed that, for energy range where the nuclear stopping of the ions is the dominating energy loss process, the spatial distribution of the energy deposited by an ion inside an amorphous solid can be approximated by a Gaussian distribution. The situation is shown in Fig. 3.1. The average energy deposited by the ion incident at the point P' in Fig. 3.1 due to nuclear collision in the bulk of the target is given by

$$E(r) = \frac{\epsilon}{(2\pi)^{3/2}\sigma\mu^2} \exp\left[-\frac{(z'+a)^2}{2\sigma^2} - \frac{x'^2+y'^2}{2\mu^2}\right], \quad (3.16)$$

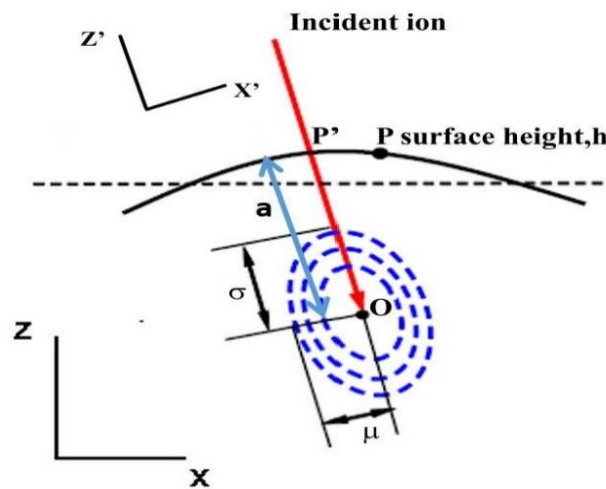


Figure 3.1: Schematic demonstration of Gaussian energy deposition of an incoming ion inside a target.

where the origin of the coordinate system $r' = (x', y', z')$ is placed at the impact point, P' of the ion and ϵ is the total energy deposited by the ion with a as the average depth of energy deposition. Here z' is measured along the direction of the incident ion trajectory and x' and y' are measured perpendicular to the z' direction. The maximum energy deposition occurs at point O, at a distance a below the surface and σ and μ are the widths of the Gaussian

distribution in the direction parallel and perpendicular to the ion trajectory, as shown in Fig. 3.1. The rate of sputtering of atoms at any surface point P is expressed in terms of recession velocity v of the surface at P which is proportional to the total energy deposited at point P by all ions incident on the surface.

$$V_o = p \int_{\mathcal{R}} dr' \phi(r') E(r'). \quad (3.17)$$

The integral extends over the region \mathcal{R} within which the impact of ions contributes significantly to the total energy deposited at P. $\phi(r')$ is the ion flux corrected for the difference between local angle of incidence γ and angle of incidence θ with respect to flat surface normal (z direction) as shown in Fig. 3.1. The proportionality constant p is the characteristic of the substrate and depends on the atomic density of the substrate N , surface binding energy U_0 and a constant C_0 related to the square of radius of the effective potential of interaction between the incident ion and target atom. p is expressed as

$$p = \frac{3}{4\pi^2} \frac{1}{NU_0C_0}. \quad (3.18)$$

B. Bradley and Harper (BH) Theory

Using Eq. 3.17, Bradley and Harper (BH) derived a linear partial differential equation to describe the dynamics of a slowly undulating surface for which the radius of curvature R at any surface point is much larger compared to the mean depth of energy deposition a . This small slope assumption allows to approximate the height of the surface in the neighborhood of the point P in Fig. 3.1 in the laboratory coordinate system (x, z) as

$$h(x) = -\frac{1}{2} \left(\frac{x^2}{R} \right), \quad (3.19)$$

here R is the radius of curvature of the surface. Based on this small slope approximation, the curvature-dependent sputter erosion rate, evaluated from Eq. 3.17, is given by

$$v(\theta, R) \cong \frac{pEfa}{\sqrt{2\pi\sigma\mu}} B_1^{-\frac{1}{2}} \exp \left(-\frac{a^2}{2\sigma^2} + \frac{A^2}{2B_1} \right) \left[\cos \theta + \Gamma_1(\theta) \frac{a}{R} \right], \quad (3.20)$$

The parameters A , B_1 , and Γ_1 are function of angle of incidence θ , incident ion flux f , a , σ , and μ . Let us now consider the limit of a flat surface, $R=\infty$. The sputtering yield in this case is $Y_0(\theta)=Nv(\theta,R=\infty)/f*\cos\theta$, where N is the number of atoms per unit volume in the amorphous solid. From Eq. 3.20 we can write that

$$Y_0(\theta) \cong \frac{pEfa}{\sqrt{2\pi\sigma\mu}} B_1^{-\frac{1}{2}} \exp\left(-\frac{a^2}{2\sigma^2}\right) \exp\left(\frac{A^2}{2B_1}\right). \quad (3.21)$$

For $\sigma>\mu$, A and B_1 is known to be an increasing function of the angle of incidence θ , meaning $Y_0(\theta)$ is also an increasing function of angle of incidence θ . In reality, however, sputtering yield begins to decrease after a critical angle θ when reflection of ions becomes important.

Using Eq. 3.21, Eq. 3.20 can be simplified to

$$v(\theta, R) \cong \frac{f}{N} Y_0(\theta) \left[\cos\theta + \Gamma_1(\theta) \frac{a}{R} \right], \quad (3.22)$$

In Eq. 3.22 the term $\Gamma_1(\theta)a/R$ contains the curvature dependence of erosion velocity. The parameter $\Gamma_1(\theta)$ is negative for normally incident ions ($\theta=0$).

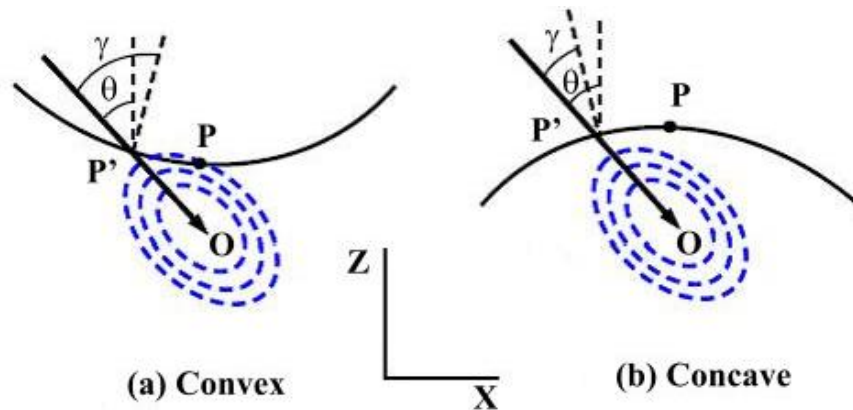


Figure 3.2: Schematic illustration of the origin of surface instability induced by ion-beam erosion of non-planar surfaces. θ is the global angle of incidence and γ is the local angle of incidence.

The radius of curvature R is negative in a trough and positive in a crest. According to Eq. 3.22, therefore, velocity of erosion is greater in surface troughs than the crests, meaning the valleys of any surface perturbation will be eroded faster than the peaks under ion bombardment. Thus sputtering increases the amplitude of the perturbation and so leads to an

instability. This reason of enhanced sputtering at troughs compared to crests discussed above is shown in the schematic diagrams of Fig. 3.2. The Gaussian distribution of the energy deposited by the incident ion is centered at point O for both the convex (Fig 3.2a) and the concave (Fig 3.2b) surfaces. Due to the geometry of convex and concave surfaces, the distance OP is smaller in the case of convex surface compared to concave surface. Therefore, the energy deposited at point P is greater for the convex (Fig 3.2a) surface, leading to a greater erosion of the valleys compared to the hills.

In BH theory, this curvature-dependent erosion rate induced surface roughening competes with the surface smoothing processes, leading to the formation of periodically modulated structures like ripples. Based on these processes, a partial differential equation for rate change of two-dimensional height profile $h(x,y)$ is presented [8].

$$\frac{\partial h}{\partial t} = -v_0(\theta) + v_0'(\theta) \frac{\partial h}{\partial x} + \left[v_x \frac{\partial^2 h}{\partial x^2} + v_y \frac{\partial^2 h}{\partial y^2} \right] - D^T \nabla^4 h. \quad (3.23)$$

The $-v_0$ term in Eq. 3.23 gives the average recession velocity of a flat surface which is not significant in pattern formation mechanism. It can be omitted by transformation to a coordinate system parallel to the surface moving with a velocity $-v_0$. The term $v_0'(\theta)$ represents a drift velocity of the surface patterns in x -direction. $v_x = \frac{fa}{N} Y_0(\theta) \Gamma_1(\theta)$ and v_y terms contain the curvature dependence of sputtering yield and is the reason for growth of sinusoidal perturbations on the surface. The only surface smoothing process considered in BH model is thermally activated surface relaxation term, $D^T \nabla^4 h$, introduced by Mullins and Herring (discussed in the following section). Any perturbation to the planar surface at $t=0$ can be considered as a superposition of periodic height modulations. Since Eq. 3.23 is linear, for small times, each of these periodic contributions to h will evolve independently. Under such conditions, it is sufficient to study the time evolution of a periodic perturbation $h(x,y,0)=Aexp[i(q_x x + q_y y)]$. Putting $h(x,y,t)=Aexp[i(q_x x + q_y y - \omega t) + rt]$ in Eq. 3.23 we obtain

$$\omega = -v_0'(\theta)q_x,$$

$$r = -(v_x q_x^2 + v_y q_y^2 + \kappa(q_x^4 + q_y^4)). \quad (3.24)$$

Here, κ represents the surface relaxation processes such as surface diffusion. The wavelength and orientation of observed ripple patterns on the surface correspond to the value of $q_{x,y}$ (wave number $q=2\pi/l$) for which the growth rate r is the maximum. The wavelength for this mode from Eq. 3.24 is given by

$$l(\theta) = 2\pi \left[\frac{2N\kappa}{f a Y_0(\theta) |\Gamma(\theta)|} \right]^{1/2}, \quad (3.25)$$

where $\Gamma(\theta)$ is smaller one between $\Gamma_x(\theta)$ and $\Gamma_y(\theta)$ and must be negative. For normally incident ions, $\theta=0^\circ$, $\Gamma_x(0)=\Gamma_y(0)$. Therefore, according to Eq. 3.20, an interlocking grid of hillocks and depressions are expected to develop on the surface. For small angles of incidence θ , $\Gamma_x(\theta) < \Gamma_y(\theta)$ and so ripples are oriented perpendicular to x -direction, the projection of the ion-beam onto the surface. The wave vector selected in this case is $q = q_x \hat{x}$ (\hat{x} is unit vector in x -direction) where $q_x = 2\pi/l_x(\theta)$ with $l(\theta) = 2\pi \left[\frac{2ND^T}{f a Y_0(\theta) |\Gamma_x(\theta)|} \right]^{1/2}$. With increasing θ , magnitude of $\Gamma_y(\theta)$ decreases and beyond a critical angle, θ_c , $\Gamma_y(\theta)$ becomes less than $\Gamma_x(\theta)$. In this condition, ripples are oriented parallel to the projection of ion-beam on the surface. For angle of incidence of the ion-beam is close to a grazing one, however, the reflection of the ion-beam becomes an important factor and BH model becomes inappropriate to describe surface morphology.

C. Non-linear extension to BH theory

BH theory is applicable to a slowly undulating surface, i.e. when the surface slope is small (as described above), the amplitude of periodic ripple patterns grows exponentially under ion bombardment and therefore, the increased surface slope becomes an important factor in the morphological evolution. Makeev, Cuerno, and Barabasi (MCB) [10] extended the BH theory

to incorporate the effect of increasing surface slope. Considering higher order terms in the Taylor series expansion of surface height, MCB derived the equation of surface height evolution as:

$$\begin{aligned} \frac{\partial h}{\partial t} \cong & -v_0 + \gamma \frac{\partial h}{\partial x} + v_x \frac{\partial^2 h}{\partial x^2} + v_y \frac{\partial^2 h}{\partial y^2} - D^T \nabla^4 h - D_{xx} \frac{\partial^4 h}{\partial x^4} - D_{yy} \frac{\partial^4 h}{\partial y^4} + \\ & \frac{\lambda_x}{2} \left(\frac{\partial h}{\partial x} \right)^2 + \frac{\lambda_y}{2} \left(\frac{\partial h}{\partial y} \right)^2 + \eta(x, y, t). \end{aligned} \quad (3.26)$$

In Eq. 3.26, $\lambda_x \left(\frac{\partial h}{\partial x} \right)^2$, $\lambda_y \left(\frac{\partial h}{\partial y} \right)^2$ are slope dependent non-linear terms. D_{xx} and D_{yy} are ion induced effective surface diffusion terms, and $\eta(x, y, t)$ is the noise term which mimics the random arrival of ions on the surface. All the coefficients except the thermal diffusion term $D^T \nabla^4 h$ and the noise term η are functions of ion energy (ε), angle of incidence (θ), ion flux (J), as well as a , σ , and μ as given below:

$$v_0 = Fc,$$

$$\gamma = F \frac{S}{f^2} [a_\sigma^2 a_\mu^2 c^2 (a_\sigma^2 - 1) - a_\sigma^4 s^2],$$

$$v_x = Fa \frac{a_\sigma^2}{2f^3} [2a_\sigma^2 s^4 - a_\sigma^4 a_\mu^2 c^2 s^2 + a_\sigma^2 a_\mu^2 c^2 s^2 - a_\mu^4 c^4],$$

$$v_y = -Fa \frac{c^2 a_\sigma^2}{2f},$$

$$\begin{aligned} D_{xx} = F \frac{a^3}{24f^5} [& -4(3a_\sigma^2 s^2 f + a_\sigma^6 s^4) f^2 + a_\sigma^2 c^2 (3f^2 + 6a_\sigma^4 s^2 f + a_\sigma^8 s^2) f \\ & + 2(a_\sigma^2 - a_\mu^2) c^2 (15a_\sigma^2 f^2 s^2 + 10a_\sigma^6 s^2 f + a_\sigma^{10} s^2)], \end{aligned}$$

$$D_{yy} = F \frac{a^3}{24f^5} \frac{3a_\sigma^2}{a_\mu^2} (f^4 c^2),$$

$$\begin{aligned} \lambda_x = F \frac{c^2}{2f^4} [& a_\sigma^8 a_\mu^2 s^4 (3 + 2c^2) + 4a_\sigma^6 a_\mu^4 c^4 s^2 - a_\sigma^4 a_\mu^6 c^4 (1 + 2s^2) \\ & - f^2 (2a_\sigma^2 s^2 - a_\sigma^2 a_\mu^2 (1 + 2s^2)) - a_\sigma^8 a_\mu^4 c^2 s^2 - f^4], \end{aligned}$$

$$\lambda_y = \frac{c}{2f^2} [a_\sigma^4 s^2 - a_\sigma^2 a_\mu^2 c^2 - f^2],$$

Where,

$$F = \frac{J\epsilon p a}{\sigma\mu\sqrt{2\pi f}} e^{-a_\sigma^2 a_\mu^2 c^2 / 2f},$$

$$a_\sigma = a/\sigma, \quad a_\mu = a/\mu, \quad f = a_\sigma^2 s^2 + a_\mu^2 c^2, \quad s = \sin \theta, \quad c = \cos \theta. \quad (3.27)$$

The significant difference between BH equation, Eq. 3.23, and MCB equation, Eq. 3.26, is the presence of non-linear terms for which deriving an analytical solution of the equation is not possible. By numerical integration of this anisotropic Kuramoto-Shivasinsky (AKS) [11,12] type equation, Park *et al.* [13] demonstrated the existence of a crossover time, t_c , below which the non-linear terms do not affect the morphological evolution and thus, the evolution is completely described by the linear terms. Beyond t_c , the non-linear term determines the surface topography and the evolution of the surface can thus, be classified into two regimes: (a) below t_c , which is called the linear regime and (b) above t_c which is termed as non-linear regime.

Linear regime: Below t_c

The linear part of MCB equation is equivalent to BH equation except the existence of ion induced effective diffusion term and the noise. Following the same analytical method as in BH theory, the wavelength of the ripples, developed under off-normal incidence of the ion-beam, can be expressed as

$$l_i = 2\pi \left(\frac{2\kappa}{|v_i|} \right)^{1/2}, \quad (3.28)$$

where, $|v_i|$ is the larger of $|v_x|$ and $|v_y|$. If $|v_x| > |v_y|$, then $l_i = l_x$ and ripples are oriented perpendicular to the x -direction, i.e., projection of the incident ion-beam onto the surface. If $|v_x| < |v_y|$, then $l_i = l_y$ and ripples are oriented parallel to the x -direction. Analytic solution of

Eq. 3.23, obtained by using Fourier transformation, provides the following equation for growth of ripple mode h_q :

$$h_q \sim e^{r_q t}, \quad (3.29)$$

with the growth factor, $r_q = -(v_i q^2 + \kappa_i q^4)$. That is amplitude of ripple with wavelength $l_i \propto 2\pi/q$ grows exponentially with irradiation time t . The surface relaxation term includes the contribution both the thermal and as well as ion induced effective diffusion so that $\kappa_i = D^T + D^I$.

Nonlinear regime: Beyond t_c

The crossover time t_c can be estimated from a comparison of strength of linear and nonlinear terms [13]. The surface width, w , (defined in Eq. 3.2) is proportional to ripple amplitude and thus, increases exponentially as $w_0 \sim \exp(vt/l^2)$ for sputtering time t below t_c . Let the typical surface height at $t=t_c$ be $w_0 = \sqrt{w^2(L, t_c)}$. Then, according to the linear part of Eq. 3.26, we obtain

$$w_0 \sim \exp(vt/l^2), \quad (3.30)$$

while from $\partial_t h = \lambda w_0^2/l^2$ we can estimate

$$\frac{w_0}{t_c} \sim \frac{\lambda w_0^2}{l^2}, \quad (3.31)$$

Combining Eqs. 3.30 and 3.31 we obtain

$$t_c \sim \frac{\kappa}{v^2} \ln \frac{v}{\lambda}, \quad (3.32)$$

In the above expression v , λ , and κ refer to direction perpendicular to the ripple orientation. The result of the numerical integration of Eq. 3.26 shows that in the nonlinear regime, evolution of surface with sputtering time is dependent upon the sign of the product of coefficients of nonlinear terms λ_x and λ_y as described below.

$\lambda_x \lambda_y > 0$: In this case, as a consequence of the nonlinear effects, the *rms* roughness w of the ion induced rippled surface stabilizes abruptly. Furthermore, the ripple pattern generated in the linear regime disappears and the ion-sputtered surface exhibits ‘kinetic roughening’.

$\lambda_x \lambda_y < 0$: The nonlinear behavior in this case can be separated into two regimes: Regime I and II. In regime I, after t_c , the system enters a long transient regime where w fluctuates within a small range and the ripples disappear. However, in regime II, which occurs after a second crossover time t_{c2} , a new ripple pattern suddenly forms in which the patterns are stable and rotated at an angle θ_c with respect to the x -direction. The angle θ_c has the value $\theta_c = \tan^{-1} \sqrt{-\lambda_x/\lambda_y}$ or $(\theta_c = \tan^{-1} \sqrt{-\lambda_y/\lambda_x})$. In regime II, w is also much larger than that in the regime I.

In the nonlinear regime, the shape of the ripple pattern also changes from symmetric to an asymmetric one due to the slope dependent erosion [14].

D. Carter-Vishnyakov approach

BH theory predicts formation of periodic ripple patterns for any off-normal incidence of the ion-beam. Experimental observations, however, demonstrate formation of ripples beyond a critical angle of incidence varying between 45° - 55° . In addition to the curvature-dependent sputtering theory of ripple formation introduced by BH and MCB, Carter and Vishnyakov (CV) [15] considered the ion induced lateral mass redistribution as the reason behind the formation of a modulated topography. The analysis of CV shows that the impact of an energetic ion at a surface point leads to displacement of the generated recoils, on the average, in a direction parallel to the initial direction of the incident beam. The average displacement of the target atoms have a component parallel to the surface in the direction of projection of the ion-beam onto the surface for off-normal incidence of the beam.

To understand the CV mechanism, a schematic diagram has been presented as Fig. 3.3. In the figure, the incident ion lies in the XZ plane of the laboratory coordinate frame which is parallel to the initially flat surface. The local coordinate system is defined with respect to the incident ion-beam with z' axis parallel to the incident beam direction and x' axis is perpendicular to it.

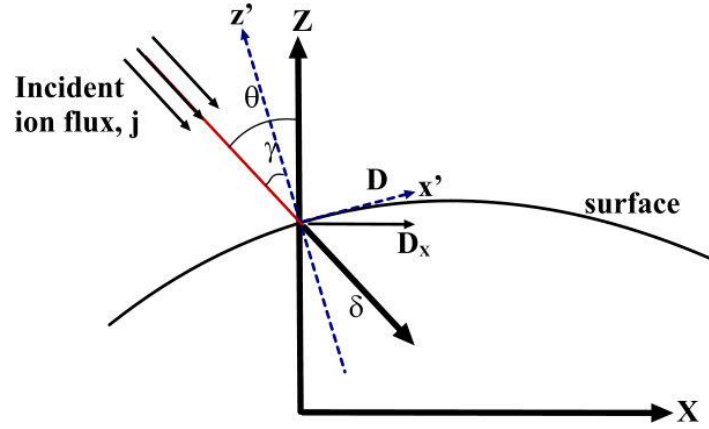


Figure 3.3: Schematic diagram of the laboratory coordinate frame (x, z) along with the local coordinate frame (x', z') to represent the CV mechanism. The local normal to the surface is represented by the unit vector z' which is also one axis of the local coordinate frame.

In Fig. 3.3 the incident ion makes an angle θ and γ with the z axis and z' -axis, respectively. $(\theta - \gamma) = \tan^{-1}(\partial h/\partial x) \approx \partial h/\partial x$ is considered to be the local misorientation of the surface. The quantity δ is the recoil displacement vector defined as $\delta = f(E)d$, where $f(E)$ is the total number of generated recoil atoms and d is the mean recoil displacement distance (the average movement of the recoils parallel to the incident ion-beam direction). D and D_x are the projections of δ on the surface and the x -axis, respectively. $v_n = -\cos(\theta - \gamma) \frac{\partial h}{\partial t}$ is defined as the normal component of the surface velocity in the present geometry. With this information, following identities are obtained [16]:

$$|D| = \delta \sin(\gamma); \quad D_x = \delta \sin(\gamma) \cos(\gamma), \quad (3.33)$$

The projection of the ion flux along the x -axis becomes $J_x = J \cos(\gamma) / \cos(\theta - \gamma)$. Therefore, net generated recoil displacement due to ion flux in the x -direction is $J_x \times D_x$. The equation of motion follows from the continuity equation [17]:

$$\frac{\partial h}{\partial t} = -\frac{1}{N} \frac{\partial}{\partial x} (J_x D_x) = \frac{J \delta a \cos 2\theta}{N} \frac{\partial^2 h}{\partial x^2}, \quad (3.34)$$

The recoil displacement generated by the ion flux, as given by Eq. 3.34 also contributes to the growth of surface height. Eq 3.34 was first introduced by CV [15] and later elaborated by

Madi *et al.* [16]. Hence, the effective surface tension term (coefficient of $\frac{\partial^2 h}{\partial x^2}$ term) which causes sinusoidal perturbations to grow on the surface becomes

$$v_x = \frac{Ja}{N} [\delta \cos 2\theta + Y_0(\theta)\Gamma_1(\theta)], \quad (3.35)$$

Eq. 3.35 includes the contribution of both the recoil displacement and the sputter erosion as given by BH (Eq. 3.23). In Eq. 3.35, N is atomic density of the target where the magnitude of δ exceeds the sputtering yield, $Y(\theta)$, by two orders of magnitude or more due to number of recoils generated, $f(E)$, likewise, the energy deposition depth a exceeds the mean recoil displacement distance d . It is therefore, probable that the coefficients of the angle-dependent terms in Eq. 3.35 will be similar.

For normal ($\theta=0^\circ$) and near-normal incidences, Eq. 3.35 becomes positive and smoothing dominates over roughening at all wavevectors. As θ increases, the roughening term assumes an increasing importance and for some critical angle (θ_c), Eq. 3.35 becomes negative and in that case roughening will dominate at all wave vectors. The above scenarios explain why ripple pattern appears to be suppressed for near-normal ion incidence and drives its own instability at higher angles. So far, the effect of mass transport has been formulated in one-dimension. It can be extended to include the effect of mass transport in the y-direction using the same formulism as above. This gives

$$\frac{\partial h}{\partial t} = \frac{J\delta a(\cos \theta)^2}{N} \frac{\partial^2 h}{\partial y^2}, \quad (3.36)$$

The magnitude of CV effect is difficult to calculate because it involves δ which is the sum of the vector displacements of all recoiled atoms, per incident ion. Madi *et al.* [16] used the Yamamura correction to sputtering yields and ion flux for the large angle of incidence to take into account the reflection of incident ions from the surface. With this correction, the total contribution of sputter erosion and atomic redistribution along x- and y-direction (S_x and S_y , respectively) can be written with the help of Eqs. 3.23, 3.35, 3.36 [16] as

$$S_x = S_{BH_x} + S_{CV_x} = Ja\Omega\Gamma_x Y_\theta + J\delta\Omega \cos 2\theta \exp\left(\frac{-\Sigma}{\cos\theta}\right), \quad (3.37)$$

$$S_y = S_{BH_y} + S_{CV_y} = Ja\Omega\Gamma_y Y_\theta + J\delta\Omega (\cos\theta)^2 \exp\left(\frac{-\Sigma}{\cos\theta}\right), \quad (3.38)$$

Here, S_{BH_x} , S_{CV_x} , and S_{BH_y} , S_{CV_y} , are the coefficients which represent the contributions of sputter erosion and atomic redistribution along x - and y -direction, respectively. θ is the angle of incidence, J is the ion current density, Y_θ is the sputtering yield as described in Eq. 1.17, and $\Omega = 1/N$ is the atomic volume of the target. Γ_x and Γ_y are functions of a , σ , μ , and θ . Σ is a function of ion energy and incident angle θ , as have been discussed in Eq. 1.17.

3.3.2 Relaxation: Process of surface smoothening

Relaxation processes tend to smooth out surface features formed by ion bombardment. A range of relaxation mechanisms have been proposed to explain various experimental observations. Determination of the relaxation mechanisms which are dominant in particular experimental conditions, involving various amorphous or crystalline substrates, surface temperatures, and ion-beam parameters, still remains the subject of extensive research. In this section, we briefly discuss various relaxation processes which may be present during the irradiation.

A. Thermal surface diffusion

This is the only type of diffusion considered in BH theory. Patterns on any amorphous surface are smoothened out due to mass transport driven by the gradient in chemical potential. For a simplified description of the process we consider a surface profile $h(x,y)$ where the variation in the surface profile occurs only in the x -direction. Chemical potential, G , per atom increases with transfer of atom from a point of zero curvature to a point of curvature R and can be expressed as $G = R\gamma\Omega$, where γ is surface free energy per unit area and Ω is atomic volume. Thus, gradient of the surface curvature produces a drift of surface atoms with a surface current [18,19] given by

$$j = \frac{D_s \gamma \Omega v}{kT} \frac{\partial R}{\partial s}, \quad (3.39)$$

where D_s is surface diffusivity, v is number of atoms per unit area, k is Boltzmann constant and s is the arc length along the profile. D_s has an Arrhenius-type behavior with temperature $D_s \sim e^{-\Delta E/kT}$ where ΔE is the activation energy for surface diffusion. The surface divergence of $-j$ gives the increase in number of atoms per unit area per unit time, which can be converted to variation in surface height by multiplying with atomic volume Ω

$$\frac{\partial h}{\partial t} = -\Omega \frac{\partial j}{\partial s} = \frac{D_s \gamma \Omega^2 v}{kT} \frac{\partial^2 R}{\partial s^2}, \quad (3.40)$$

Using small slope approximation $R \sim -\frac{\partial^2 h}{\partial x^2}$ and $\partial s \sim \partial x$, Eq. 3.40 reduces to

$$\frac{\partial h}{\partial t} = -D^T \frac{\partial^4 h}{\partial x^4} = -D^T \nabla^4 h, \quad (3.41)$$

Where, $D^T = \frac{D_s \gamma \Omega v}{kT}$ is the surface diffusion constant. Eq. 3.41 can be readily extended for a two-dimensionally varying surface to give

$$\frac{\partial h}{\partial t} = -D^T \left(\frac{\partial^4 h}{\partial x^4} + \frac{\partial^4 h}{\partial y^4} \right). \quad (3.42)$$

B. Effective surface diffusion (ESD)

As described in the sub-section “non-linear extension to BH theory”, the higher-order expansion of surface height leads to appearance of terms in the evolution equation (Eq. 3.26) which mimics the smoothening of surface due to surface diffusion and therefore, is called ion induced effective surface diffusion (ESD) term. The ESD [20] does not imply real mass transport along the surface but preferential erosion of the surface where surface hills are eroded faster than the valleys. If the system is viewed from a coordinate frame moving together with the average height of the surface, this preferential erosion appears as a re-organization of the surface, corresponding to a surface diffusion like mechanism. As seen from Eq. 3.26, the ESD coefficients D_{xx} and D_{yy} are different along x - and y -direction,

implying anisotropy in diffusion on the surface. The importance of ESD is that it is independent of temperature and thus, can be effective at low temperatures where thermal diffusion is negligible.

C. Ion induced viscous flow

The ion induced viscous flow (IVF), proposed by Umbach, Headrick, and Chang, considers surface-confined viscous flow driven by surface tension as the dominant smoothing mechanism which can occur in case of materials with a disordered surface layer with reduced viscosity [21]. The coefficient of viscous flow is given by

$$D_{xx} = D_{yy} = D_{IVF} = \frac{\gamma d^3}{\eta_s}, \quad (3.43)$$

Here, η_s is ion-enhanced surface viscosity and γ is surface free energy per unit (both are assumed to be constant and isotropic). The parameter d is the depth of the damaged layer, which is taken to be equal to the ion penetration depth d . Although viscous flows can be effective in amorphous materials, the approach of the IVF can be extended to crystalline substrates where a thin damaged surface layer is created by irradiation, such as InP [22]. If IVF is considered as the smoothing mechanism, the evolution equation 3.23 predicts the ripple wavelength to be an increasing function of ion energy and substrate temperature and independent of ion flux, which successfully describes the characteristics of ripple formation on SiO₂. Furthermore, molecular dynamics (MD) simulations by Mayr *et al.* emphasized on important roles of flow of point defects and of thermal-spike induced local melting in ion-induced viscous flow in the energy range of 0.1-1 keV [23].

3.3.3 Hydrodynamic model

In the theoretical models of ion-bombarded surface described so far, effective surface tension (described by the term $\nu_x \frac{\partial^2 h}{\partial x^2}$) which leads to instability of the surface against growth of modulation is caused by sputter erosion (BH theory) or mass redistribution (CV theory and

the carter function model). In the fluence range, where the periodic surface patterns appear, the ion bombardment can also result in amorphization of target materials. Viscous flow of material in the amorphous layer can occur under ion bombardment due to the stress generated by irradiation. Castro *et al.* [24] put forward a model which demonstrates the formation of periodic surface patterns due to this viscous flow in the amorphous layer.

In the low and medium energy ranges, nuclear energy is the dominant energy loss process. Incident ions generate vacancies and interstitials in the subsurface layer, which can diffuse at different rates, annihilate by recombination, or form clusters. As observed from molecular dynamics simulations, the overall effect of these processes is three-fold: Amorphization of target, development of stress, and displacement of the mean position of atoms inside the material. Moreover, experimental studies on Si reveal that thickness and other mechanical properties of the generated amorphous layer, like density, become stationary after a fluence of the order of 10^{14} ions cm^{-2} .

In the model of Castro *et al.*, the amorphous layer is treated as a fluid flowing under stress. A body force, $b \equiv \nabla \cdot T^s$, acting in the bulk of the fluid layer is defined on the basis of the conservation laws of mass and momentum for fluid where, T is the stress tensor. This force can be splitted into amplitude, f_E , and an angular contribution, Ψ , which is a function of the local angle of incidence. Mathematically, $b = f_E \Psi(\theta - \gamma)$ where γ is the local slope of the surface and θ is the angle of incidence of the ion-beam. f_E contains the coarse-grained information about the effect of the residual stress created in the target, due to ion-induced mass redistribution, and has dimensions of a gradient of stress. Using proper boundary conditions, Castro *et al.*, specified the evolution for two important boundaries of the system: the amorphous-vacuum interface (the free surface), $h^{(a)}$, and the amorphous-crystalline interface, $h^{(c)}$. Kinematic condition at each interface leads to evolution equation for both $h^{(a)}$ and $h^{(c)}$ as

$$\frac{Dh^{(c)}}{Dt} - u = j_{am}, \quad (3.44)$$

$$\frac{Dh^{(a)}}{Dt} - u = j_{er}, \quad (3.45)$$

where, u is the vertical component of the velocity field of the fluidized layer. The terms j_{am} and j_{er} stand for the rates of amorphization and erosion, respectively.

With the help of Eq. 3.44 and 3.45, a dispersion relation for this viscous fluid was obtained under the condition of “shallow water” approximation and no erosion. In this approximation, the thickness of an amorphous layer is assumed to be much less than the characteristic wavelength of the ripple pattern. The characteristic wavelength is given by

$$l_c = \frac{2\pi}{q_c} = 2\pi \left(\frac{2\sigma}{-f_E \partial_\theta (\Psi(\theta) \sin \theta)} \right)^{1/2}. \quad (3.46)$$

Here, σ is the surface tension of target and $\Psi(\theta) = \cos(\theta)$ is the angular contribution (namely, that the body force is proportional to the local flux at the surface). Thus, the term $\partial_\theta (\Psi(\theta) \sin \theta)$ in the denominator of Eq. 3.46 becomes $\phi(\theta) = \cos(2\theta)$. It is observed from Eq. 3.46 that for $\theta < 45^\circ$, the denominator is negative. This implies that the periodic ripples should start to appear for an angle of incidence $> 45^\circ$.

The hydrodynamic model is applicable to linear regime only. However, the prediction of this model is an explicit function of incident ion energy. For example, the ripple wavelength is directly related with ion energy [25] in the following fashion:

$$l = E^a \text{ where } a \in [0.93 - 1.08], \quad (3.47)$$

This model also provides the value of crossover time t_c as

$$t_c(E, \theta) \sim 1/JE^{-7/3+2m}\phi^2(\theta), \quad (3.48)$$

J is the incident ion flux and the exponent m depends on ion-solid interaction as described in Chapter 1. The crossover time, t_c , depends on three parameters viz. ion-flux J , -energy E , and

the angle of incidence, θ . The proportionality sign in Eq. 3.48 is omitted by using any reference cross-over time $t_c(E_{ref}, \theta_{ref})$ as follows [26]:

$$t_c(E, \theta) = t_c(E_{ref}, \theta_{ref}) \frac{J_{exp}(E_{ref}, \theta_{ref}) E_{ref}^{-7/3+2m_{ref}} \phi^2(\theta_{ref})}{J_{exp} E^{-7/3+2m} \phi^2(\theta)}, \quad (3.49)$$

It is observed from Eq. 3.49 that if t_c is known for any particular experimental condition, it can be easily estimated for other cases.

3.3.4 Shadowing effect

Under off-normal incidence of ion-beam on a surface, BH theory or linear version of MCB model predicts an exponential increase in amplitude of the developed ripple pattern on surface with sputtering time. The development of surface slope due to the exponential increase in ripple amplitude can result in, apart from the initiation of nonlinear effects, a situation where the ion-beam can be restricted from falling on the upstream face of a ripple by the preceding ripple peak. This phenomenon, called shadowing effect, becomes a factor of utmost importance in determining the evolution of ripple patterns when angle of ion incidence is close to grazing or even at lower angle of ion incidence in case of relatively high amplitude ripple pattern evolution induced by medium energy ion bombardment. The effect of shadowing on ripple pattern evolution can be understood from the geometrical argument introduced by Carter [27].

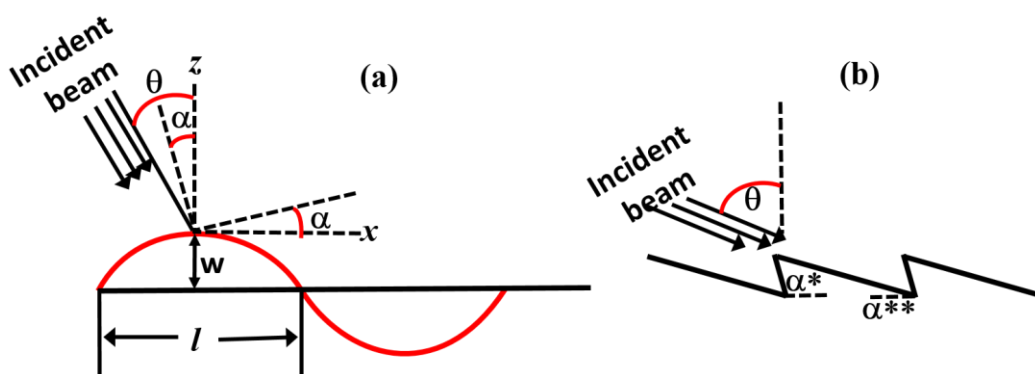


Figure 3.4: Illustration of geometry of ion bombardment on a sinusoidal profile. (a) Total surface is exposed to the ion-beam and (b) faceting fully developed beyond the shadowing condition.

A schematic diagram illustrating Carter's argument is presented in Fig. 3.4. In Carter's model, any fluctuation in regular sinusoidal ripple patterns with wave-vector aligned parallel to the projection of the ion-beam onto the surface is ignored and thus, only a two-dimensional section in the xz plane through the surface can be considered as shown in Fig. 3.4(a). This surface profile can be described by $h=w \cos(2\pi x/l)$ where h is the ripple amplitude, w is the surface width, and l is the ripple wavelength. The ion-beam is incident on the surface at an angle θ to the normal to the mean surface plane (the Oz -axis). Over an incremental surface length ds , at the point O on the surface, the gradient of the surface slope is given by $\tan(\alpha)=\partial h/\partial x$. It is clearly visible that α is also the angle between the local surface normal and the Oz -axis. As the ratio of the ripple amplitude and the ripple wavelength $w:l$ increases, the maximum gradient of the sinusoidal ripple pattern $2\pi w/l$ becomes too large and, as a consequence, the local angle of incidence of the incident ion-beam ($\theta-\alpha$) decreases, ultimately reaching a limiting condition when the incident ion-beam is parallel to the back slope of the ripple pattern. For any further increment in $w:l$ ratio, the upstream face of the ripples is 'blocked' or 'shadowed' from the incident ion-beam by the preceding peak in the waveform. The limiting value of the ratio $w:l$ for shadowing not to occur is given by

$$\tan\left(\frac{\pi}{2} - \theta\right) \geq \frac{2\pi w}{l}, \quad (3.50)$$

which places an upper limit on the ratio $w:l$ for any angle of ion incidence θ . If this ratio exceeds then the valleys will not be eroded but the peaks will be. Although the dynamics of the subsequent changes in surface morphology is difficult to describe theoretically, it is reasonable to expect that a transformation to a sawtooth-like waveform will gradually evolve for prolonged ion sputtering as shown in Fig. 3.4(b), with facets inclined at an angle α^* and α^{**} with respect to the horizontal direction.

Bibliography

1. Y. Zhao, G.-C. Wang, T.-M. Lu, M. De Graef, and T. Lucatorto, *Characterization of Amorphous and Crystalline Rough Surface-Principles and Applications*. Vol. 37. 2000: Access Online via Elsevier.
2. MATLAB, *Version 7.9.0. (R2009a)*. 2009, The Mathworks Inc.: Natick, Massachusetts.
3. W.H. Press, *Numerical recipes 3rd edition: The art of scientific computing*. 2007: Cambridge university press.
4. A. Keller, S. Facsko, and R. Cuerno, *Computational Nanotechnology: Modeling and Applications with MATLAB®* (2011) 189.
5. A.S. Image Metrology. *SPIP Software*. Available from: www.imagemet.com.
6. International Organization of standardization. *ISO 25178*. Available from: www.iso.org.
7. L. Michigan Metrology. *ISO 25178*. Available from: www.michmet.com/Texture_parameters.htm.
8. R.M. Bradley and J.M.E. Harper, *J. Vac. Sci. Technol. A* 6 (1988) 2390.
9. P. Sigmund, *Phys. Rev.* 184 (1969) 383.
10. M.A. Makeev, R. Cuerno, and A.-L. Barabási, *Nucl. Instrum. Methods Phys. Res. B* 197 (2002) 185.
11. Y. Kuramoto and T. Tsuzuki, *Prog. Theor. Phys.* 55 (1976) 356.
12. G.I. Sivashinsky, *Acta Astronaut.* 6 (1979) 569.
13. S. Park, B. Kahng, H. Jeong, and A.L. Barabási, *Phys. Rev. Lett.* 83 (1999) 3486.
14. J. Muñoz-García, R. Cuerno, and M. Castro, *Phys. Rev. B* 78 (2008) 205408.
15. G. Carter and V. Vishnyakov, *Phys. Rev. B* 54 (1996) 17647.

16. C.S. Madi, *Linear stability and instability patterns in ion bombarded silicon surfaces*. 2011.
17. A.-L. Barabási and H.E. Stanley, *Fractal concepts in surface growth*. 1995: Cambridge university press.
18. C. Herring, J. Appl. Phys. 21 (1950) 301.
19. W.W. Mullins, J. Appl. Phys. 30 (1959) 77.
20. M.A. Makeev and A.-L. Barabási, Appl. Phys. Lett. 71 (1997) 2800.
21. C.C. Umbach, R.L. Headrick, and K.-C. Chang, Phys. Rev. Lett. 87 (2001) 246104.
22. F. Frost, A. Schindler, and F. Bigl, Phys. Rev. Lett. 85 (2000) 4116.
23. S. Mayr, Y. Ashkenazy, K. Albe, and R. Averback, Phys. Rev. Lett. 90 (2003) 055505.
24. M. Castro and R. Cuerno, Appl. Surf. Sci. 258 (2012) 4171.
25. M. Castro, R. Gago, L. Vázquez, J. Muñoz-García, and R. Cuerno, AIP Conf. Proc. 1525 (2013) 380.
26. M. Castro, R. Gago, L. Vázquez, J. Muñoz-García, and R. Cuerno, Phys. Rev. B 86 (2012) 214107.
27. G. Carter, J. Appl. Phys. 85 (1999) 455.

CHAPTER 4

4 Morphological evolution under medium energy ion irradiation

4.1 Introduction

As discussed in Chapters 1 and 3, experimental parameters, viz. ion-current density, -fluence, and angle of incidence are crucial parameters to optimize the evolution of ion-induced nanostructures. Especially, the length scales of such patterns are found to be a function of incident ion energy. While the evolution of patterns has been explored both in low (a few hundreds of eV) as well as medium energy (up to hundred keV) regimes, it is not yet clear whether same mechanisms are operative in these two different regimes. For instance, for low energy regime, nuclear energy loss is the dominating ion energy loss process inside a target while at medium energies both nuclear and electronic energy loss values are of comparable order of magnitude.

Most commonly observed irradiation driven nanostructure formation is understood as a competition between surface roughening due to sputter erosion and smoothing of surface by physical processes such as surface diffusion. In this frame work, pattern formation is divided into linear and nonlinear regimes. For low energy case, these two different regimes are well-identified and transition from one regime to the other has also been distinguished [1]. On the other hand, existing reports on medium energy ion induced patterning [2,3] is yet to explicitly demonstrate the distinct evolution of patterns in linear and nonlinear regimes in absence of any coexistent contributing effect such as shadowing. This in turn also lacks proper understanding to explain the mechanisms responsible for pattern formation. In fact, experimental distinction of linear and nonlinear regimes during pattern formation at this

energy regime is important to check the possibility of invoking mechanisms similar to those involved in low energy ion induced patterning. For instance, in case of low energy, comparison of experimental observations with the theoretical understanding of ion-induced pattern formation based upon competition between sputter erosion and surface smoothing mechanisms is performed only in the linear regime. This is because in the nonlinear regime the slope dependent nonlinear effects lead to ripple wavelength coarsening or development of broken ripples. Such modifications in surface topography make it difficult to check the applicability of theoretical models on ripple formation which are linear in nature.

Investigation of ripple patterning by medium energy ion irradiation can also provide further insight into the process of pattern evolution. For example, the early stage of pattern formation has been hard to obtain because of the inherent length scale associated with ripple wavelengths formed at low energies (up to a few keV). For instance, low-energy ions lead to evolution of ripples with wavelengths typically in the range of 30-50 nm.[1,4-7] Thus, measurement of corresponding changes in wavelength due to a small variation in fluence at lower values (i.e. the early stage of ripple formation) becomes limited by the accuracy of the characterization tool. As a result, initial wavelength of ripples (up to certain fluence) was reported to be constant (within the experimental resolution).[1,8] However, higher values of ripple wavelength at intermediate energies should remove the inherent limitation of addressing low energy ion induced pattern formation at low fluences (as discussed above). Therefore, for a better understanding of pattern formation at an early stage, intermediate energy keV ions can be an attractive tool.

In our experimental studies presented in this chapter, we attempted to understand the mechanisms responsible for evolution of surface morphology by using 60 keV Ar⁺-ion irradiation of Si. In addition, 60 keV Xe⁺-ion irradiation of Si has also been carried out to present complementary experimental results. From our experimental results, we have clearly

identified linear and nonlinear regimes of evolution of ripple patterns on Si in this energy regime. Based on the present results and those available in the literature at comparable ion energies, we have constructed a parametric phase diagram. Subsequently, we have identified some striking similarities in patterns formed at these two energy regimes. Based upon the observation of such similarities, we invoked the theoretical models which are invoked to understand the evolution of low energy ion induced surface patterns. Evolution of surface morphology, in the present case, is shown to be an outcome of contributions of sputter erosion and ion-induced prompt atomic redistribution. This agrees well with the recent theoretical predictions on mechanisms responsible for Ar-ion induced pattern formation in the low energy regime. Subsequently, we illustrated the nature of wavelength selection for early stage of ripple formation on Si surface due to 60 keV Ar⁺-ions. Experimentally, a decreasing trend in ripple wavelength up to a certain time is observed. This is understood in terms of linear stability analysis based on the continuum theory.

4.2 Experimental

One-side polished Si(100) substrates (*p*-type; size 5×5 mm²) were exposed to 60 keV Ar⁺ and Xe⁺-ions at room temperature (RT). A bigger piece of sacrificial Si, cut from the same lot, was mounted beside each target to ensure a low-impurity environment [4]. Uniform irradiation was achieved by scanning the beam over the entire sample surface. During Ar⁺-ion irradiation, the angle of incidence of ions (θ) with respect to the sample surface normal was varied from 0°-75°. Ion fluence for all angles was varied from 2×10^{17} to 3×10^{18} ions cm⁻² (at a constant target current density of 20 μ A cm⁻²) whereas it was increased to 8×10^{18} ions cm⁻² for $\theta=60^\circ$. Xe⁺-ion irradiation was carried out for a fixed angle of incidence of 60° using ion current density of 1.5 μ A cm⁻². In this case, ion fluence was varied from 1×10^{16} to 5×10^{17} ions cm⁻².

All irradiations were carried out under the secondary electron suppressed geometry as described in Chapter 2. Surface morphology of the irradiated samples was studied *ex-situ* by atomic force microscopy (AFM) in ACTM mode. A large number of AFM images were acquired for different scan areas (of 1×1 to 40×40 μm²) and from different places in order to achieve high reliability of the extracted parameters. Using SRIM simulation, the projected range of 60 keV Ar-ions in Si was found to be 38 nm (with corresponding lateral straggling of 20 nm) [9].

4.3 Results

4.3.1 Temporal evolution of Si morphology

4.3.1.1 Topography in the low fluence regime: Initial wavelength selection

Figs. 4.1(a)-(d) show AFM images of Si samples before and after exposure to Ar⁺-ions at incidence angle $\theta = 60^\circ$. The arrow marks indicate the projection of ion-beam direction onto the surface (described as *x*-direction hereafter). The corresponding autocorrelation functions and the line profiles (taken along the line shown on the autocorrelation images) are shown in the insets, at the top- and bottom-right corners of AFM images. AFM images of samples implanted below the fluence of 1×10^{18} ions cm⁻² are not presented since they exhibit the uncorrelated rough surfaces. Thus, we may infer that ripples evolving at this fluence (1×10^{18} ions cm⁻²) are at their initial stages of formation. Autocorrelation images, *rms* surface roughness, and ripple height were extracted from AFM images by using the WSxM software [10]. Line profiles extracted from the respective autocorrelation images were used to calculate ripple wavelengths at different fluences. The calculated ripple wavelengths are found to be 900 nm, 850 nm, and 760 nm for fluences of 1×10^{18} , 2×10^{18} , and 3×10^{18} ions cm⁻², respectively. Thus, we observe a clear decreasing trend in ripple wavelength with increasing irradiation time which contradicts the pattern coarsening behavior with increasing fluence [11]. In Fig. 4.1(e) we show 2D power spectral densities (PSD) extracted from the

surface morphologies in Figs. 1(b)-(d) in the radial direction. The observed decreasing trend of ripple wavelength with increasing irradiation time is reflected in the position of the main peak in the PSD (dominant wavelength in the corresponding morphology) which is observed to shift towards higher values of q (here, $q=2\pi/\text{ripple wavelength}$) [indicated by the vertical line in Fig. 4.1(e)]. It is also noted that a similar trend of decreasing ripple wavelength up to a certain fluence (3×10^{18} ions cm^{-2}) is observed at all other angles ($45^\circ \leq \theta \leq 75^\circ$) in the present study [12].

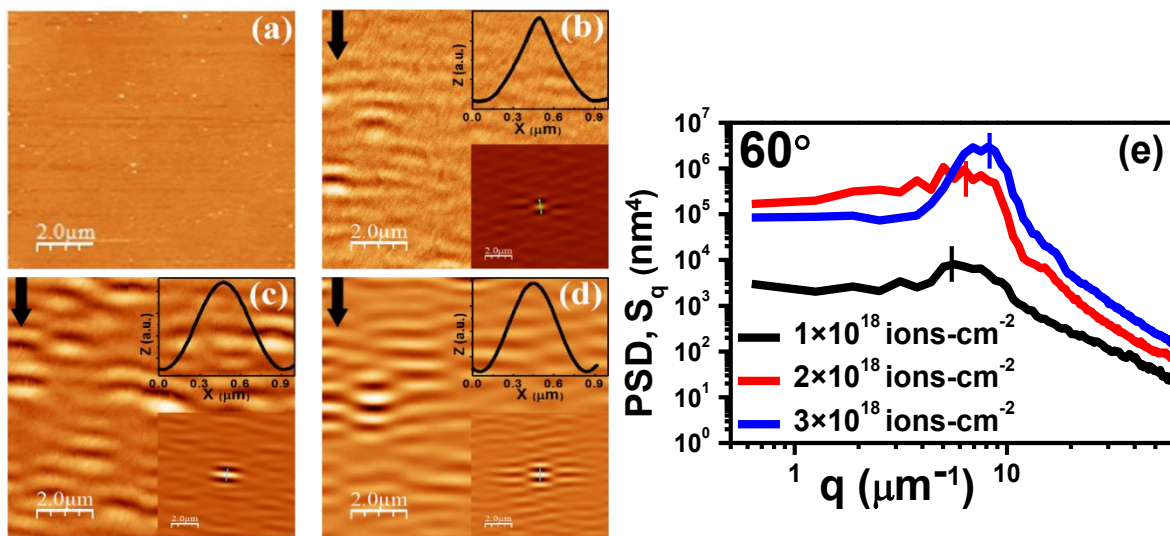


Figure 4.1: AFM images ($10\times 10 \mu\text{m}^2$) of Si samples before and after exposure to Ar^+ -ions at an incident angle 60° : (a) Pristine-Si surface, (b)-(d) implanted Si surfaces at fluences 1×10^{18} , 2×10^{18} , and 3×10^{18} ions cm^{-2} , respectively. The corresponding height scales for (b)–(d) are 4.0, 15.9, and 45.4 nm, respectively. The autocorrelation images of the implanted samples are also shown as insets of the corresponding image. Line profiles (taken along the line shown on the autocorrelation images) are shown on the respective autocorrelation images. Arrows indicate the direction of incident ion-beam on the surfaces. (e) Radial 2D PSD calculated as a function of irradiation time. The vertical short line at the highest data point of each plot represents the characteristic wavelength of ripple pattern.

4.3.1.2 Topography evolution in the high fluence regime: Ripple coarsening

The evolution of ripple pattern beyond the fluence of 3×10^{18} ions cm^{-2} is presented Fig. 4.2. Ripple coarsening starts taking place beyond this fluence which is evident from Figs. 4.2(a) and (b). The plot in Fig. 4.3 summarizes the variation in λ with ion fluence at $\theta = 60^\circ$. The value of λ decreases from 900 nm to 760 nm corresponding to fluences of 1×10^{18} and 3×10^{18}

ions cm^{-2} , respectively whereas it increases up to 1120 nm at the highest fluence of 8×10^{18} ions cm^{-2} .

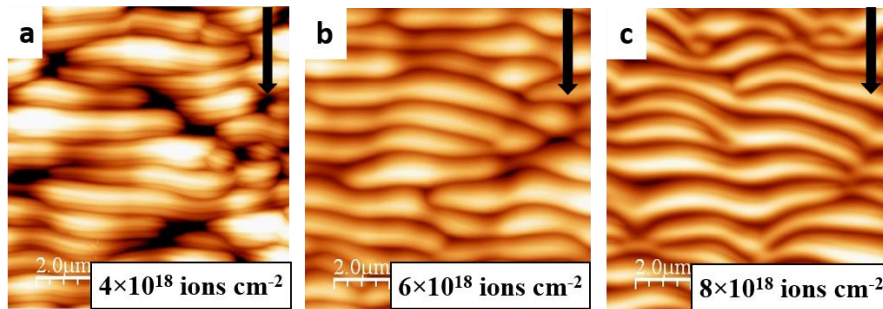


Figure 4.2: AFM image of Si (100) surface irradiated at $\theta=60^\circ$ for fluences: (a) 4×10^{18} ions cm^{-2} , (b) 6×10^{18} ions cm^{-2} , and (c) 8×10^{18} ions cm^{-2} . The corresponding height scales are 294.17, 332.13, and 281.2 nm, respectively. Black arrows on the images show direction of the incident ion-beam.

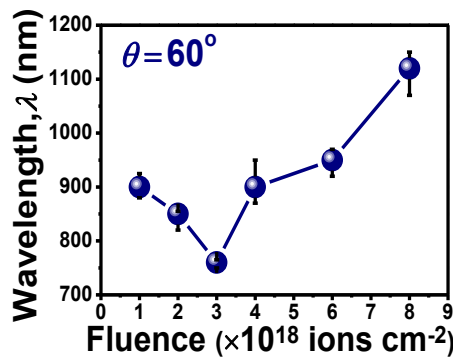


Figure 4.3: Ripple wavelength, λ , determined from the autocorrelation functions of the corresponding AFM images as a function ion fluence for $\theta=60^\circ$.

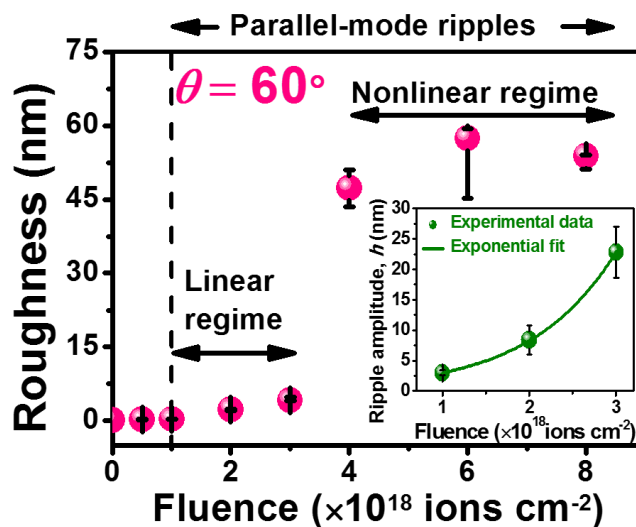


Figure 4.4: *rms* roughness of Si surface irradiated at $\theta=60^\circ$ as a function of ion fluence. The dashed vertical line shows the critical fluence for evolution of ripple patterns. The inset shows growth of ripple amplitude in the linear regime as a function of ion fluence. The solid line indicates an exponential fit to the experimental data.

The variation in the *rms* roughness of silicon samples irradiated at $\theta=60^\circ$ is presented in Fig. 4.4 where the vertical dashed line depicts the threshold ion fluence (1×10^{18} ions cm^{-2}) at which ripples appear. The *rms* roughness demonstrates a rapid growth up to the fluence of 4×10^{18} ions cm^{-2} , while it is almost constant in the fluence range 6 to 8×10^{18} ions cm^{-2} . In addition, the inset shows an exponential increase in ripple amplitude with increasing ion fluence (up to 3×10^{18} ions cm^{-2}).

4.3.1.3 Absence of shadowing effect

Previously, it was observed that ripple evolution beyond the linear regime could be dominated by ion-beam shadowing, i.e., the rear slopes of ripples would not be seen by the incident beam while the front slopes are eroded [2] (discussed in Chapter 3). Moreover, it has been shown both in low [13] as well as medium energy regimes [14] that sinusoidal ripple structure undergoes a transition to faceted structure under the influence of shadowing at the later stage of irradiation. In fact, Carter [15] had shown that the critical condition to avoid shadowing can be described by

$$\tan\left(\frac{\pi}{2} - \theta\right) \geq \frac{2\pi h_0}{\lambda}. \quad (4.1)$$

Here h_0 is the ripple amplitude (calculated from the height-height correlation function) and λ is the ripple wavelength. According to Eq. 4.1, the critical value of h_0/λ for which ripple patterns remain below the shadowing regime is 0.09 (for $\theta=60^\circ$). We have also calculated the fractional sputtering yield, which is defined as the ratio of the difference in sputtering yield of ripple patterned surface from that of a flat surface to sputtering yield of the flat surface. Carter [15] has shown the value of this fractional sputtering yield can be of the order of 1, starting from the initial value of 0. For values of fractional sputtering yield close to 1, shadowing starts to take place and faceted structures develop on ion-sputtered surface. Accordingly, we have calculated the amplitude to wavelength ratio and fractional sputtering yield for Ar-ion induced ripple morphologies on Si at each fluence. The results are shown in

Table 4.1. From these data we see that the amplitude to wavelength ratio remains well below the critical value of 0.9 and the fractional sputtering yield of the order of 0.01 in the entire fluence range of our experiment. Thus, it can be concluded that the shadowing does not play any role in the observed morphological evolution. Therefore, no facet formation is expected in the later stage of surface evolution in our study. This was further verified from the fact that no such saw-tooth structures were observed in the line profiles taken over the AFM images.

Table 4.1

Amplitude to wavelength ratios and fractional sputtering yield calculated from AFM images for 60 keV Ar⁺-ion irradiated Si

Fluence (ions cm ⁻²)	Height, h_0 (nm)	Wavelength or base width, λ (nm)	Shadowing Condition for $\theta=60^\circ$ $2\pi h_0/\lambda > 0.5773$	Fractional sputtering yield
Pristine	-	-	--	--
5E17	0.26	-	--	--
1E18	0.51	900	0.00356	1.01475E-6
2E18	3.12	850	0.02305	4.25729E-5
3E18	5.52	760	0.04561	1.66643E-4
4E18	47	900	0.32796	0.00845
6E18	62	950	0.40985	0.01305
8E18	42	1120	0.2355	0.0044

4.3.1.4 Linear and nonlinear evolutions

In order to achieve more in-depth understanding of ripple evolution with ion fluence, we now analyze other features, namely shape and amplitude of the ripples. For instance, the slope angle or gradient angle [$f(\alpha)$; discussed in Chapter 3] of the ripples are extracted from the histogram of derivatives of the height profiles and are plotted as a function of ion fluence in Fig. 4.5. For the pristine sample, the distribution has a nominal width which is typical of a smooth surface. For argon-ion implanted samples, the peak position of $f(\alpha)$ distribution represents the average slope of the ripples where negative $f(\alpha)$ corresponds to the upstream part (front slope) of ripples facing the ion-beam and positive $f(\alpha)$ refers to the downstream part (rear slope) of ripples. The symmetric distribution [Fig. 4.5(a)] around 0° indicates

similar shapes of the front and the rear slope which remain intact with increasing ion fluence. It is also observed that width of the distributions corresponding to 1×10^{18} , 2×10^{18} , and 3×10^{18} ions cm^{-2} are 0.76° , 1.49° , and 2.67° , respectively which qualitatively indicates that the ripple height increases at higher fluences.

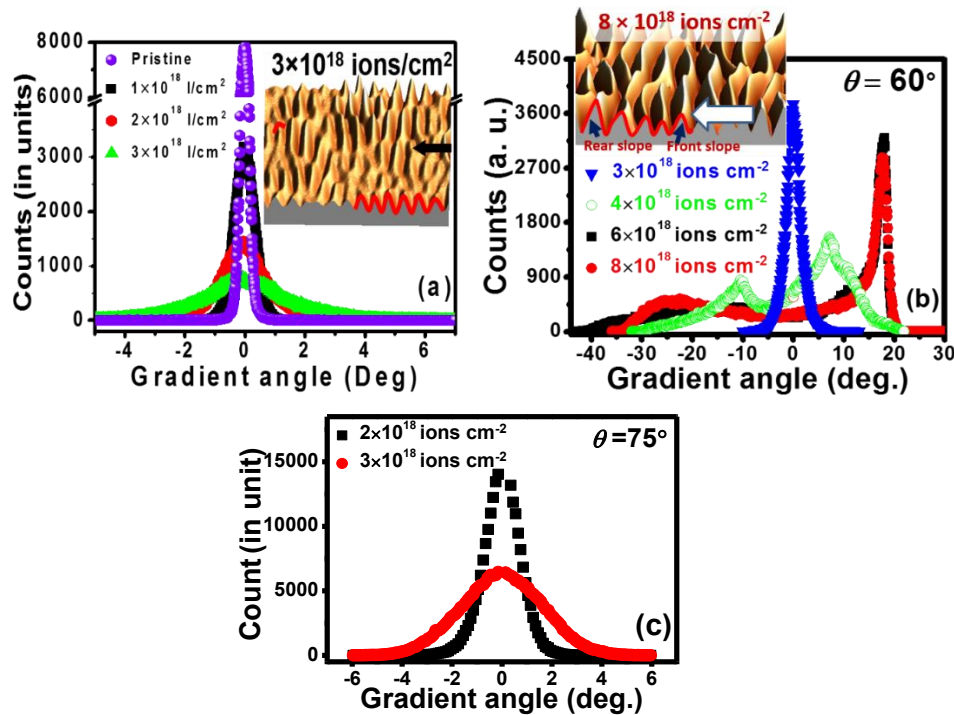


Figure 4.5: Distribution of gradient angle over the ripple patterned surfaces (determined from AFM images) for fluences (a) $1\text{--}3 \times 10^{18}$ ions cm^{-2} at $\theta=60^\circ$, (b) $3\text{--}8 \times 10^{18}$ ions cm^{-2} at $\theta=60^\circ$ and (c) $2\text{--}3 \times 10^{18}$ ions cm^{-2} at $\theta=75^\circ$. The inset shows a 3-dimensional (3D) AFM image corresponding to the ion fluence of 8×10^{18} ions cm^{-2} . The white arrow shows direction of the ion-beam projected onto the surface. The red curved line at the crosssection of 3D image is drawn to emphasize the shape of the ripple pattern.

For direct visualization of the ripple shape, a three-dimensional AFM image of the irradiated sample corresponding to the highest fluence is shown as the inset of Fig. 4.5(a). Here two curved lines are drawn on the image – one line follows the shape of the ripples at one edge of the image while the other one follows the pattern in the middle of the image, showing the symmetric shape of the ripples. In contrast to 3×10^{18} ions cm^{-2} , two peaks observed in Fig. 4.5(b) at higher fluences give the average slope for two sides of a ripple pattern (indicated by the red line on the AFM image shown in the inset). The peaks are situated at 7.15° and -10.15° , 17.5° and -17.65° as well as 17.65° and -22.45° corresponding to fluences of 4×10^{18} ,

6×10^{18} , and 8×10^{18} ions cm^{-2} , respectively. Absence of any peak at 0° and observation of two peaks for all these fluences clearly indicate the asymmetric nature of the ripple patterns unlike the case of 3×10^{18} ions cm^{-2} . For the fluence of 4×10^{18} ions cm^{-2} , peaks seem to be closer to 0° and width of the peak at positive side is little broader compared to the two higher fluences. Peaks at positive gradient angles almost coincide for fluences of 6×10^{18} and 8×10^{18} ions cm^{-2} and the width of the peaks is narrower compared to those at negative gradient angles. Shift in a peak position towards higher gradient angle with increasing ion fluence indicates that both front and rear slopes become steeper with increasing fluence. In addition, the greater distance of the peaks at negative gradient angles from the origin than those at positive gradient angles for different ion fluences indicates that the front slope is steeper than the rear one. A 3D view of the AFM image (showing a crosssectional view of the surface) corresponding to the sample irradiated to the fluence of 8×10^{18} ions cm^{-2} is shown in the inset of Fig. 4.5(b). The arrow on the image shows the projected direction of incident beam onto the surface. A curved line drawn near the left bottom part of the image (which follows the shape of ripple patterns) qualitatively shows the difference in slopes between the front and the rear ones. This direct observation agrees well with the above approach of gradient angle distribution. Similar to the 60° case, Fig. 4.5(c) reveals symmetric distribution of gradient angle (around 0°) at $\theta=75^\circ$, for both the representative fluences, indicating the formation of symmetric ripples corresponding to the oblique ion incidence angle of $\theta=75^\circ$.

We now consider a continuum description of the system discussed in Chapter 3. In a reference frame which is moving with the average surface height, the evolution equation is expected to read [16,17]

$$\frac{\partial h(x,y)}{\partial t} \cong v_x \frac{\partial^2 h}{\partial x^2} + v_y \frac{\partial^2 h}{\partial y^2} - K \nabla^4 h + M[h] + \eta(x,y,t), \quad (4.2)$$

where v_x, v_y are the components of ion-induced “surface tension” (that may incorporate both BH-type erosive and CV-like surface-confined mass transport contributions), $-K \nabla^4 h$

accounts for surface relaxation processes (such as thermal surface diffusion and/or surface-confined viscous flow [18]), $N[h]$ accounts for nonlinear corrections, henceforth assumed to be negligible, and $\eta(x,y,t)$ is Gaussian white noise with zero average and constant variance $2D$. This noise term accounts for the randomness of the microscopic processes going on (ion arrival, sputtering events, surface diffusion attempts, etc.) [19]. At the early stage of evolution, the nonlinear terms can be ignored and the amplitude h_q of ripples (of wavelength $\lambda = 2\pi/q$) should increase exponentially with irradiation time. With increasing irradiation time the influence of the nonlinear effects becomes evident, giving rise to a transition to the nonlinear regime. Thus, it is important to consider whether the time-dependent behavior that we obtain for the ripple wavelength can still be accounted for within the framework of Eq. 4.2. Thus, the exponential growth in average ripple height with irradiation time that we observe in Fig. 4.4 indeed suggests that the temporal evolution of our ripple pattern is within the linear regime. To strengthen this conclusion further we analyze the time-dependent shape evolution of the observed ripples described above, which can help to determine the transition from the linear to the nonlinear regime. In fact, the correlation between the change in the ripple shape from a symmetric to an asymmetric one with the transition to the non-linear regime was put forward by Muñoz-Garcia *et al.*[20], subject to small-slopes condition, $h/\lambda \ll 1$. From Fig. 4.5(a) it is clear that the symmetric shape of the ripples persists up to the fluence of 3×10^{18} ions cm^{-2} , and in addition the condition $h/\lambda \ll 1$ also holds true [see Table 4.1]. These observations establish that the evolution of the ripple pattern up to the fluence of 3×10^{18} ions cm^{-2} belongs to the linear regime. Similarly, the evolution of ripples at $\theta=75^\circ$ is also considered to be in the linear regime from the observation of symmetric ripple shape in Fig. 4.5(c). Thus, asymmetric ripple shapes seen at fluences higher than 3×10^{18} ions cm^{-2} (for $\theta=60^\circ$) can be considered to arise from nonlinear effects (as discussed above). This is in

contrast to ripple evolution due to low energy ions where a faster transition from linear to nonlinear regime takes place at higher incidence angles [1,5].

4.3.1.5 Influence of ion mass on topography surface

Figs. 4.6(a)-(f) show AFM images of Si samples after exposure to Xe⁺-ions for various fluences at a fixed ion incidence angle of 60°. The arrow marks indicate the projection of ion-beam direction onto the surface (described as *x*-direction). The corresponding autocorrelation images are shown in the insets at the right bottom corners of corresponding images. Ripple patterns start to appear from the fluence of 5×10¹⁶ ions cm⁻² and grow with the irradiation time, followed by appearance of broken ripples at the highest fluence of 5×10¹⁷ ions cm⁻². Variation in ripple height and wavelength with fluence is shown in Fig. 4.6(g) where height is found to increase exponentially. In addition, coarsening of wavelength is observed from the fluence of 1×10¹⁷ ions cm⁻². Based on the behavior of the wavelength, the evolution of the ripple patterns can be divided into linear and nonlinear regimes as shown in Fig. 4.6(g). Comparison of ripple wavelengths formed by Ar⁺- and Xe⁺-ion irradiation from Figs. 4.3 and 4.6(g), respectively reveals that the wavelength is much smaller in case of Xe irradiation. The smaller values of ripple wavelength and threshold fluence of ripple formation (5×10¹⁶ ions cm⁻²) compared to those for Ar⁺-ion case could be a result of heavier mass of Xe⁺ ions.

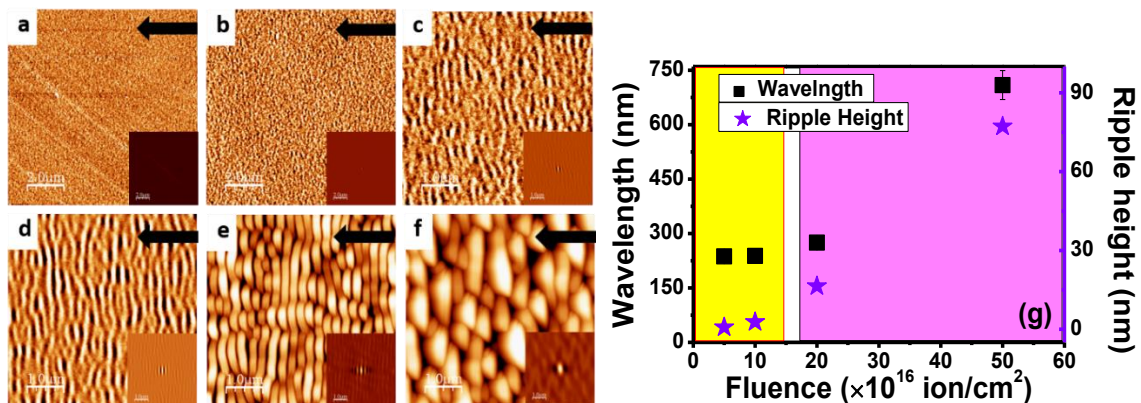


Figure 4.6: AFM image of 60 keV Xe⁺-ion irradiated Si as a function of fluence: (a) 1×10¹⁶ ions cm⁻², (b) 2×10¹⁶ ions cm⁻², (c) 5×10¹⁶ ions cm⁻², (d) 1×10¹⁷ ions cm⁻², (e) 2×10¹⁷ ions cm⁻², and (f) 5×10¹⁷ ions cm⁻². The corresponding height scales for (b)-(f) are 1.6, 1.0, 1.5, 5.5, 30.1, and 178.2 nm, respectively. Corresponding ripple heights and wavelengths are plotted in (g).

4.3.2 Influence of ion angle of incidence on surface topography

The influence of ion angle of incidence on morphological evolution during 60 keV Ar⁺-ion irradiation on Si is illustrated in Fig. 4.7.

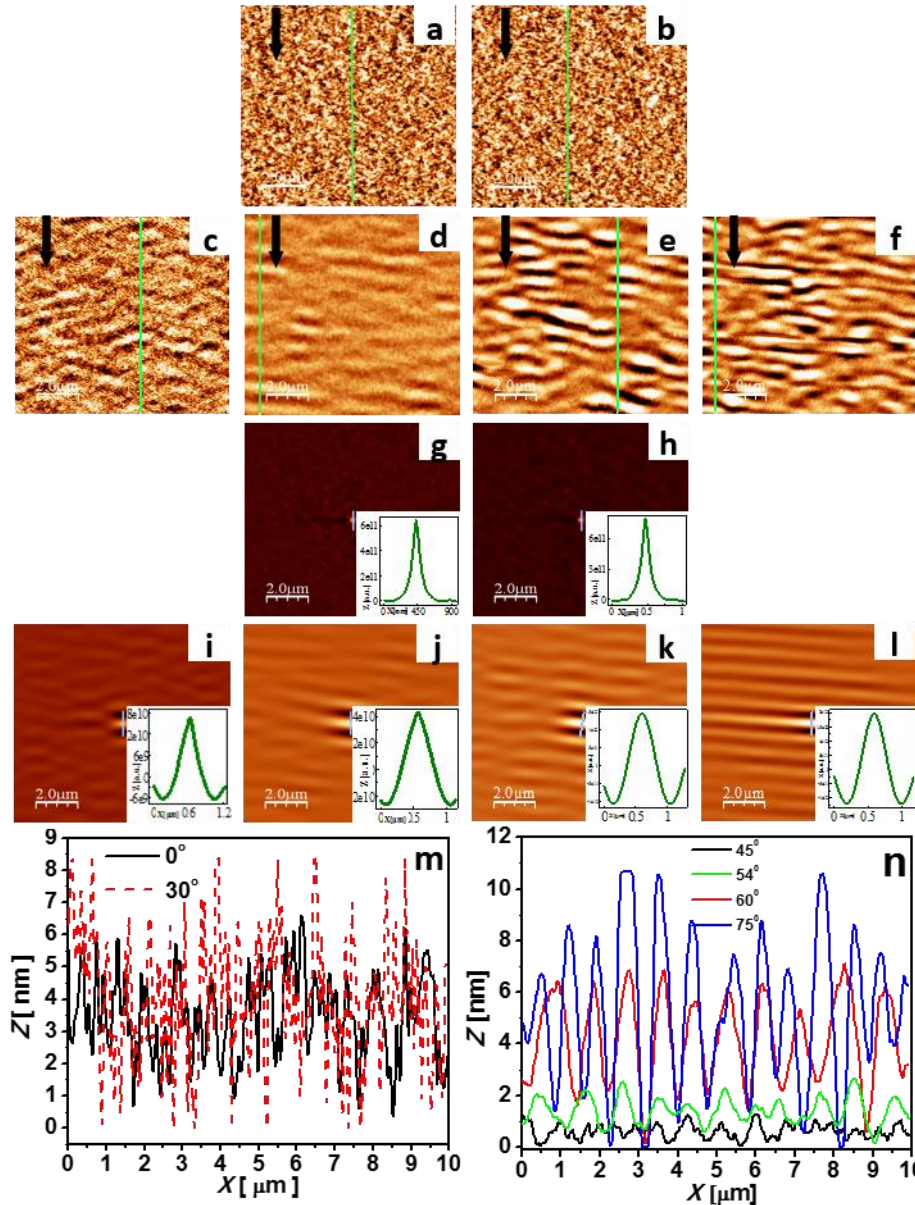


Figure 4.7: AFM images of Si(100): (a) Implanted with 60 keV Ar⁺-ions to the fluence of 2×10^{18} ions cm^{-2} at incident angles of 0°, (b) 30°, (c) 45°, (d) 54°, (e) 60°, (f) 75°, and (g)-(l) are auto correlation image of (a)-(f), respectively. Insets in (g)-(l) show line profiles, taken along the lines shown on the autocorrelation images. Line profiles taken along the line shown on (a) and (b) are numbered by (m), while (n) shows line profile taken along the line shown on (c), (d), (e) and (f).

Figs. 4.7(a)-(f) represent the evolution of morphology of Si surfaces (after irradiation to the fluence of 2×10^{18} ions cm^{-2}) corresponding to incident angles of 0°, 30°, 45°, 54°, 60°, and

75°, respectively. Figs. 4.7(g)-(l) show the two-dimensional (2D) autocorrelation functions of (a)-(f), respectively, where the insets show the line profiles (taken along the lines shown on the images). Fig. 4.7(m) shows the line profiles corresponding to silicon samples exposed to Ar-ions at 0° and 30°. It is found that no ripple morphology evolves up to 30° although roughness increases with increasing incident angle. This is further realized from a more zigzag nature of the line profiles. Fig. 4.7(n) shows the line profiles, corresponding to incident angles of 45°, 54°, 60°, and 75°. From these images, it is clear that ripple formation starts to evolve from an incidence angle of 45° and becomes more prominent at higher angles. Observation of ripple patterns in the angular window of 45°-75° is in contrast to the previous reports where the authors observed evolution of ripple morphology at Si surfaces (for 60 keV argon ions at RT) only over an angular window of 55–70° and reported the absence of ripple beyond the 70° [2,21]. It may be mentioned that ripple height, extracted from the line profiles, shown in Fig. 4.7(n), increases with increasing angle of incidence. Ripple wavelengths, calculated from the autocorrelation functions are in good agreement with the values calculated from AFM line profiles (corresponding to Figs. 4.7(c)-(f)). In Fig. 4.8 we show the variation of λ as a function of angle of incidence θ (for the fixed fluence of 2×10^{18} ions cm^{-2}) where a linear decrease in ripple wavelength with increasing incident beam angle is observed, while the surface roughness increases (once the ripple sets in).

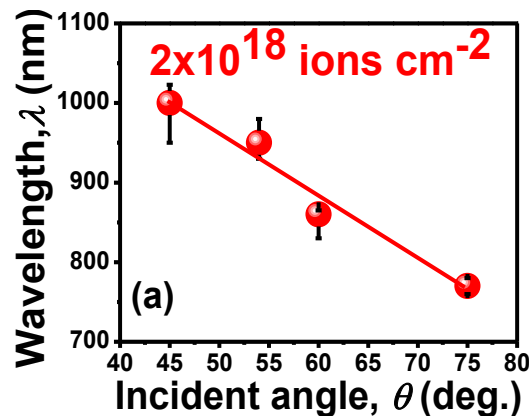


Figure 4.8: Ripple wavelength, λ , determined from the AFM images as a function of angle of incidence θ for a fixed ion fluence of 2×10^{18} ions cm^{-2} .

4.3.2.1 Parametric (E - θ) Phase diagram

To present an overview of medium energy ion induced pattern formation on Si surface and to explore the commonalities with patterns formed at low energy regime, we have used the results of our experiments along with reports available in the literature and constructed a parametric (E - θ) phase diagram which is presented in Fig. 4.9.

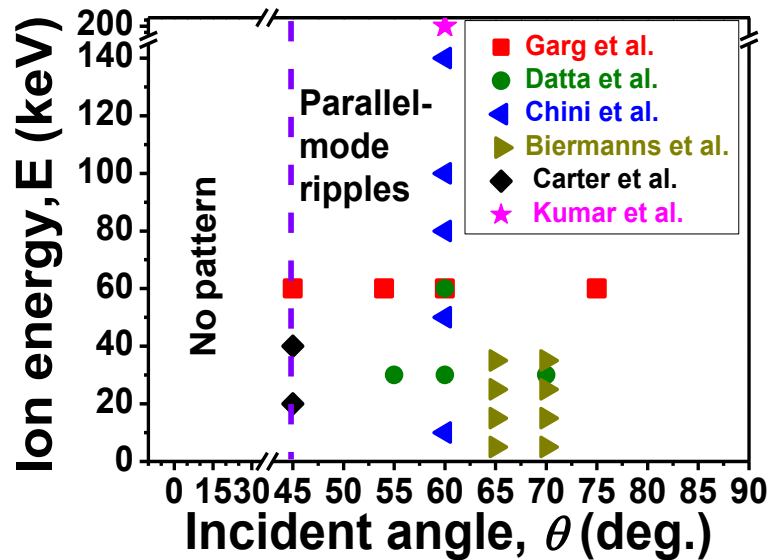


Figure 4.9: Parametric phase diagram showing inert gas ion-induced formation of ripple patterns in the medium energy regime (in the fluence range $\sim 10^{18}$ ions cm^{-2}). ■: Garg *et al.* [12], ●: Datta *et al.* [2], ◀: Chini *et al.* [22], ▶: Biermanns *et al.* [3], ◆: Carter *et al.* [23], and ★: Kumar *et al.* [24].

In the phase diagram, the existence of a sharp boundary is evident at 45° where flat to rippled surface transition takes place. Since no signature of pattern formation is observed for $\theta < 45^\circ$ under the present experimental conditions it may be identified as the critical angle (θ_c) for pattern formation under the present experimental conditions. Observation of rough a surface at $\theta = 0^\circ$ in the present case, agrees well with the previous results [2,12] other than Mohanta *et al.* [25] who reported dot formation due to 50 and 100 keV Ar^+ -ion irradiation of Si. It may be mentioned that observations of dot/hole patterns [26-28] for low energy ions at $\theta = 0^\circ$ were attributed to the presence of impurity [6,29]. In addition, the value of $\theta_c = 45^\circ$ agrees with the results obtained for 40 keV Xe- and Ar-ion irradiation of Si [23], although it differs from that of 55° reported [2] for 30 keV Ar^+ -ion irradiation of Si. Incidentally, the value of $\theta_c = 45^\circ$ is

found to be very close to those observed in case of low energy ion induced surface patterns [4,30]. Moreover, we observe that the ripple wave vector is parallel to the incident ions up to 75° which is also the case for low energy ion irradiation. Further, the energy dependence of ripple wavelength at both low and medium energy regimes can be expressed as $\lambda \propto E^p$ where p follows a decreasing trend [18,22,26,31].

4.4 Discussion

4.4.1 Role of ion angle of incidence

The above discussion, based on the proposed parametric phase diagram and other experimental data, demonstrates some striking similarities related to various features of low and medium energy ion-induced ripple patterns, albeit their wavelengths differ in length scale (by an order of magnitude). Thus, one can infer that ripple formation at medium energy (tens of keV) regime should be possible to be described using the similar mechanisms invoked in low energy (few hundreds of eV) regime.

Theoretical understanding of the ion-induced patterning process has been discussed in Chapter 3. Ripple formation during low energy ion irradiation has been explained in many cases [32-36] within the framework of Bradley-Harper theory [16] based on curvature-dependent sputtering. According to BH theory, ripple formation is expected at any off-normal incidence of the ion-beam [19]. However, the experimental observation of a critical angle of incidence around 45° , for both low and medium energy ion-induced ripple formation (as discussed above) clearly contradicts the prediction of BH theory. This indicates that, similar to the low energy case, the results obtained for medium energy ion irradiation on Si cannot be understood by invoking only the effect of curvature-dependent sputtering based BH theory alone. To explain the absence of ripples and its appearance below and at $\theta_c=45^\circ$, respectively (at comparable ion energies), Carter and Vishnyakov [23] considered ion impact induced prompt atomic redistribution of atoms during ion irradiation. However, these authors did not

extend their study beyond 45° and in absence of any other report on the applicability of CV model in the medium ion energy regime, ripple evolution at angles of incidence higher than 45° is yet to be understood by invoking only the CV model.

In a recent study, Madi *et al.* [30] have shown that low energy (few hundreds of eV) ripple formation can be explained by invoking only the CV model and in doing so they have also shown that the role of sputter erosion becomes essentially irrelevant. However, erosion effects might become non-negligible at higher ion energies and for crystalline materials where anisotropy can influence all the potentially relevant processes [30,37]. Madi *et al.* concluded that it remains to be shown that erosion effects are actually important for stability (absence of pattern) or pattern formation. More recently, Hofsäss [38] has predicted that formation of ion-induced parallel-mode ripples (wave vector perpendicular to the projection of ion-beam) at and above the critical angle, θ_c , (and preceded by absence of the same below) can be explained only if one considers the combined effects of both curvature-dependent sputter erosion (BH mechanism) and atomic redistribution (CV effect). This has been shown to hold true for both low energy (250 eV) Ar-ions and medium energy (40 keV) Xe-ions.

To further investigate the relative contributions of erosion and atomic redistribution to ripple pattern evolution, we have carried out numerical estimations using our experimental parameters. As discussed in chapter 3 in a linear continuum description of the ion irradiated surface where x -direction is assumed to be parallel to the projection of ion-beam onto the surface and y -direction perpendicular to it, the contributions of sputter erosion and atomic redistribution can be expressed separately along x - and y -directions through the coefficients S_{BH_x} , S_{CV_x} , and S_{BH_y} , S_{CV_y} , respectively. The details of these coefficients are described by Eqs. 3.37 and 3.38 in Chapter 3. When S_x and $S_y < 0$, the wavelength of the ripple patterns formed on the surface is given by Eq. 3.28 [$\lambda_i = 2\pi \left(\frac{2\kappa}{|v_i|} \right)^{1/2}$] (where v_i is equivalent to S_i ($i=x$ and y)).

We estimated S_{BH_x} , S_{BH_y} , S_{CV_x} , S_{CV_y} , S_x , and S_y as a function of angle of incidence, θ , By using Eqs. 3.37 and 3.38. The value of the parameters, viz., ion energy deposition depth a , longitudinal and transverse widths of the cascade σ and μ , forward recoil δ , and Y_0 , the sputtering yield at normal incidence, for 60 keV Ar^+ ion irradiation in Si, which are needed for this estimation, have been simulated using the Monte Carlo simulation code SDTrimSP 5.05 [39]. The output file ‘particle_stop_r.dat’ generated by SDTrimSP contains the initial and final locations of all the recoil target atoms (50000 atoms have been considered for the present simulation). A vacancy is assumed to be created in the initial position of recoil atoms and the recoil atom is considered as an interstitial at the final position. The distribution of vacancies in the x -direction is shown in Fig. 4.10(a). The energy deposition depth a and longitudinal straggling σ is obtained from the peak and width of the vacancy distribution by a Gaussian fit to be 42.5 nm and 29 nm, respectively. The distribution of vacancies in the y - and z -directions (transverse to the incident beam direction) is shown in Fig. 4.10(b).

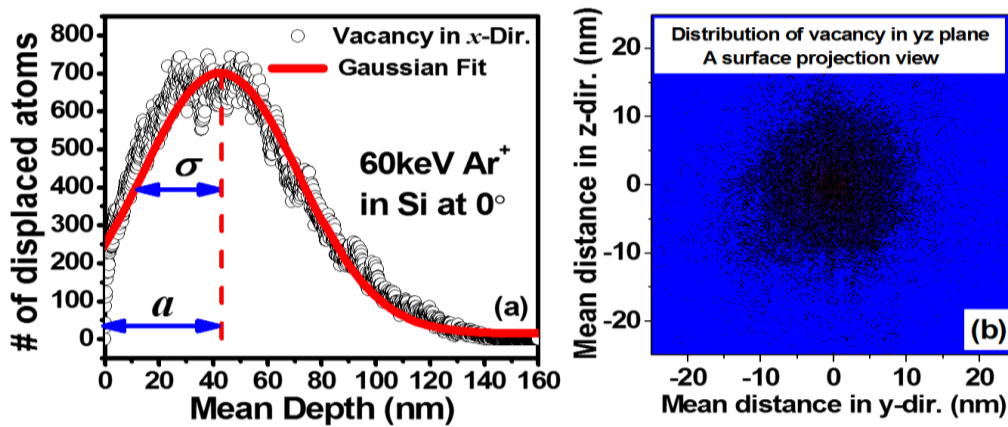


Figure 4.10: Vacancy distribution in Si due to 60 keV Ar^+ -ion irradiation as simulated by SDTrimSP 5.05: (a) in a direction parallel to the incident beam (x -direction), i.e., along depth, (b) along y - z directions (perpendicular to the ion-beam, i.e., parallel to the surface).

The 2D Gaussian fit to the vacancy distribution gives the transverse widths of the distribution as $\mu_x = \mu_y = 8.4$ nm. To calculate δ we estimate the mean depth of vacancies and recoils as

$$\bar{d}_v = \frac{\sum_i V_i \cdot x_i}{\sum_i V_i} \text{ and } \bar{d}_R = \frac{\sum_i R_i \cdot x_i}{\sum_i R_i}, \quad (4.3)$$

The parameter δ is obtained from these mean depths and average number of vacancies per ion N_D as –

$$\delta = N_D(\bar{d}_R - \bar{d}_v), \quad (4.4)$$

The above calculation gives the value of δ to be 184.8 nm.

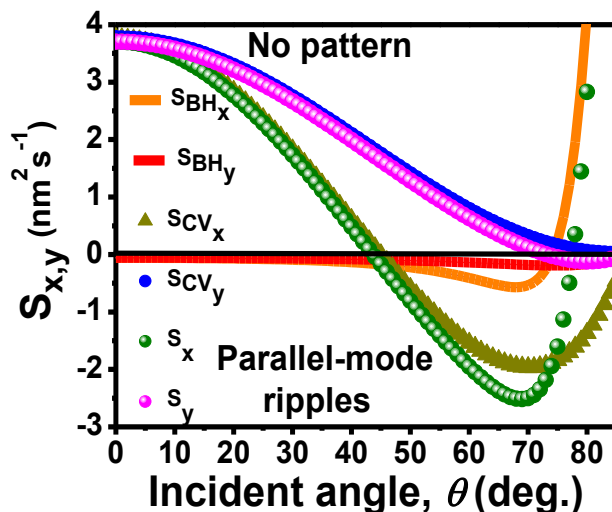


Figure 4.11: Plots of the coefficients S_{BH_x} , S_{BH_y} , S_{CV_x} , and S_{CV_y} (as a function of angle of incidence, θ), expressing the contributions of curvature-dependent sputter erosion (BH mechanism) and ion-induced atomic redistribution (CV effect) along x - (parallel to the incident beam direction) and y -direction (perpendicular to x -direction), respectively. The total contributions of the BH mechanism and the CV effect along x - and y -direction are also shown in the form of S_x and S_y , respectively [40].

In Fig. 4.11, we show variations in S_{BH_x} , S_{BH_y} , S_{CV_x} , S_{CV_y} , and their superposition $S_{x,y} = S_{BH_{x,y}} + S_{CV_{x,y}}$ with incidence angle, θ . It is clearly observed that S_{BH_x} remains negative in the angular range $0^\circ \leq \theta < 74^\circ$ with $|S_{BH_x}| > |S_{BH_y}|$. Thus, if only sputter-erosion contributes to pattern formation, parallel-mode ripples should form over this angular window. On the other hand, it is observed that S_{CV_x} remains negative in the angular range $45^\circ \leq \theta \leq 90^\circ$ while S_{CV_y} is positive for this range. Therefore, if redistribution of target atoms would be the only mechanism leading to ripple formation, parallel-mode ripple patterns would be seen everywhere in the said angular range. In the present case, although the upper limit of our experimental angular window was chosen to be 75° it is quite unlikely that patterns would be

observed at higher grazing incidences ($>80^\circ$) since it is well-known that at those angles most of the ions would be reflected rather than initiating pattern formation. Thus, CV effect may not be the sole responsible factor for the observed pattern formation in the present case. On the other hand, we note that the total contribution of erosive and redistributive contributions, expressed by S_x , is negative in the angular range $45^\circ \leq \theta \leq 77^\circ$ with $|S_x| > |S_y|$ – predicting parallel-mode ripple formation in this angular range. Thus, our experimental observation of parallel-mode ripple formation in the angular range $45^\circ \leq \theta \leq 75^\circ$ can be explained if both sputter erosion and prompt atomic redistribution processes are considered to be operating simultaneously [40].

4.4.2 Initial wavelength selection: Stability analysis

Since the ripple evolution in the early stage is found to be in the linear regime, the nonlinear terms in Eq. 4.2 is ignored in subsequent analysis. The linearized Eq. 4.2 can be readily solved by Fourier transform (discussed in Chapter 3) [16,17]. Assuming a flat initial condition, each Fourier mode of the height evolves independently as $h_{\mathbf{q}} \sim e^{r_{\mathbf{q}} t}$, where $r_{\mathbf{q}} = -(\nu_x q_x^2 + \nu_y q_y^2 + \kappa q^4)$ is the so-called linear dispersion relation and $\mathbf{q} = (q_x, q_y)$ is wave-vector. Under pattern-forming conditions, the “surface-tension” coefficients $\nu_{x,y} < 0$, so that $r_{\mathbf{q}}$ reaches a positive maximum for a given Fourier mode $h_{\mathbf{q}^*}$. Assuming $\nu_x < \nu_y$, $\mathbf{q}^* = (|\nu_x|^{1/2}/(2K)^{-1/2}, 0)$. Thus, the amplitude $h_{\mathbf{q}^*}$ dominates all other Fourier modes, leading to a ripple structure along the x -axis, with wavelength $\lambda = 2\pi/q_x^*$. This is the linear wavelength selection mentioned above. With respect to the time evolution, at very early times $t < t_{c1}$, Eq. (1) leads to a smoothing-like relaxation controlled by noise and the surface-diffusion like term [41]. At larger fluences $t_{c1} < t < t_{c2}$, one expects the development of the linear instability, during which exponential amplification of surface features (ripple amplitude, surface roughness) occurs. Finally, $t = t_{c2}$ signals the onset of nonlinear effects, once surface slopes have become sufficiently large.

In order to fully describe the experimental behavior, we need to take into account the fact that the initial (pristine) surface is not mathematically flat; actually, it generically features non-trivial space correlations [42], which may be particularly noticeable in the early-time evolution. Thus, in what follows we perform numerical simulations of Eq. 4.2 (i.e., we ignore the nonlinear terms), in which the initial condition is the AFM image of the experimental pristine sample. This allows us to compare in detail the experimental observations with the dynamical evolution of the surface height according to the linear model. The values of the parameters ν_x , ν_y , K , and D have been estimated from a fit of the structure factor $|h(\mathbf{q},t)|^2$ for time t , obtained from the AFM images of the irradiated surface, in which its value at time $t = 0$ (corresponding to the pristine surface) has been taken into account. Note that, for a non-flat initial condition with structure factor $|h(\mathbf{q}, 0)|^2$, the exact solution of Eq. 4.2 leads to [30,43]

$$|h(\mathbf{q}, t)|^2 = \exp(2r_{\mathbf{q}}t) \left(|h(\mathbf{q}, 0)|^2 + \frac{(2\pi)^2 D}{r_{\mathbf{q}}} \right) - \frac{(2\pi)^2 D}{r_{\mathbf{q}}}. \quad (4.5)$$

Using this equation, a simple-minded fit of the structure factors of samples irradiated for two different times, $t=6,960$ s and $13,920$ s, provides $\nu_x=-5.18 \times 10^{-5} \mu\text{m}^2\text{s}^{-1}$, $\nu_y=-2.4 \times 10^{-7} \mu\text{m}^2\text{s}^{-1}$, $K=4.16 \times 10^{-7} \mu\text{m}^4\text{s}^{-1}$, and $D=1.4 \times 10^{-12} \mu\text{m}^2\text{s}^{-1}$. In our numerical simulations, we have employed periodic boundary conditions, a centered-differences discretization of Eq. 4.2, and an Euler-Maruyama scheme for the temporal evolution, with steps $\Delta x=\Delta y=10/128 \mu\text{m}$, and $\Delta t=2 \times 10^{-3}$ s, respectively. These choices of Δx and Δt allow direct comparison between simulated and experimentally-observed morphologies. We have confirmed that simulation results do not differ significantly for smaller step sizes. With the values of the parameters described above, the simulated surface morphologies are observed to correspond to the experimentally observed patterns (including consistent values of the ripple wavelength for each fluence) at irradiation times ten times smaller than those of the simulations. Given the uncertainty in estimating the value of t_{c1} (time of onset of the linear instability), and in order to reach a one-to-one correspondence between the simulation and the experimental results,

we have scaled down the values of parameters ν_x , ν_y , and K uniformly by a factor of 10, thus keeping the wavelength of mode h_{q^*} unchanged, and the value of D by a factor of 3.

Surface morphologies, as simulated from Eq. 4.2, are shown in Figs. 4.12(a)-(c) for simulation times 7,000, 14,000, and 21,000 s, respectively. These three simulation times have been selected in order to reach an optimal correspondence between experimental and simulated morphologies. The simulation time of 7,000 s corresponds to an ion fluence of 1×10^{18} ions cm^{-2} , where ripple patterns start to appear and thus, Simulation times 14,000 and 21,000 s are equivalent to ion fluences of 2×10^{18} and 3×10^{18} ions cm^{-2} , respectively.

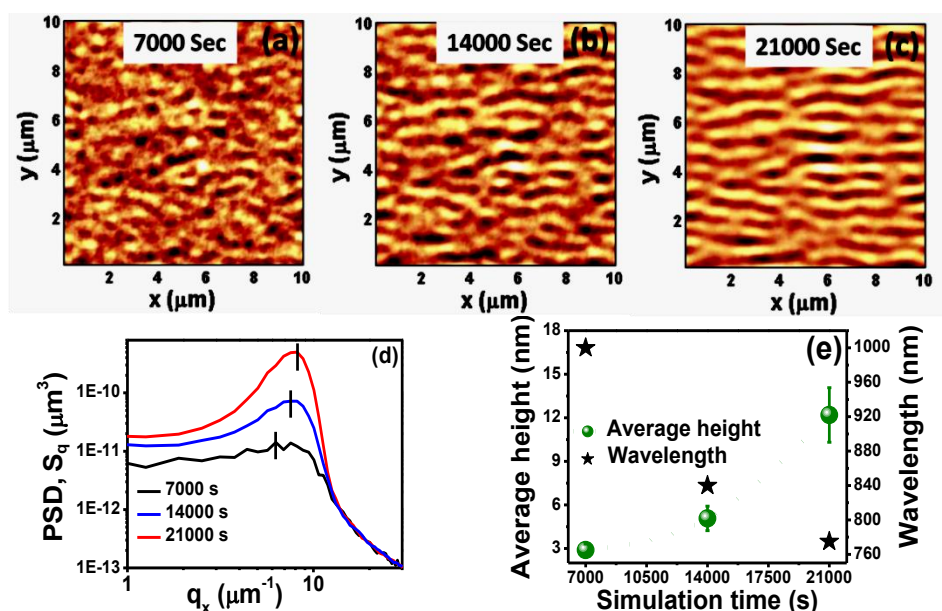


Figure 4.12: Surface morphologies generated by numerical simulations. The images correspond to irradiation times: (a) 7,000, (b) 14,000, and (c) 21,000 s. (d) Corresponding power spectral densities, S_{q_x} . For each curve the position of the absolute maximum is shown by a black line. (e) Average surface height and ripple wavelength as functions of irradiation time. Error bars shown for average heights indicate the corresponding values of the roughness.

In Fig. 4.12(d) we show power spectral densities (PSD) calculated for one-dimensional cuts of the surface morphologies in Figs. 4.12(a)-(c) along the x -direction, parallel to the ripple wave-vector (vertical direction in the snapshots). In order to reduce statistical fluctuations that can mask the position of local maxima, here we choose to plot the 1D PSD instead of the 2D PSD. With increasing simulation time, the position of the main peak in the PSD

(dominant wavelength in the corresponding morphology) is observed to shift towards higher values of q_x [indicated by the black line for each curve in Fig. 4.12(d)]. This implies a decreasing behavior of the ripple wavelength with increasing irradiation time. The average amplitude and wavelength of the simulated ripple patterns are plotted in Fig. 4.12(e). The error bars of the ripple amplitudes correspond to the roughness value (*rms* of the height distribution) for that simulated pattern. The wavelengths of the simulated ripple patterns in Fig. 4.12(e) are comparable with those of the experimentally observed ones described above at the respective sputtering times. Fig. 4.12(e) also shows that ripple amplitude (average height) increases exponentially, similarly to the experimental behavior [see the inset in Fig. 4.4]. Further quantitative differences between the simulated and the experimentally-observed amplitude and roughness might be due to approximations involved in Eq. 4.3. Thus, we have only considered the terms that are most relevant to the evolution of the ripple amplitude and to the selection of the ripple wavelength, and which have been experimentally motivated [1,30]. In order to improve the quantitative description of the surface – and thus account for additional features of the patterns, such as namely in-plane transport – additional terms are possibly required, such as third-order derivatives [20].

We should mention that the decreasing trend of the ripple wavelength with fluence does not occur in simulations when an ideally flat surface is employed as initial condition ($t=0$), keeping the same set of parameter values as above (results not shown). Namely, in such a case the ripple wavelength is found to remain constant with increasing simulation time. However, the ripple amplitude and roughness of the simulated morphology still have quite similar values at each simulation time as obtained for the pristine initial morphology.

Thus, our numerical simulations of Eq. 4.2 indicate that the decreasing behavior of the ripple wavelength with irradiation time, observed in the initial stage of pattern formation, is induced by the morphology of the initial surface. Intuitively, when Fourier-transformed, the form of

the pristine surface turns out to have a relatively large contribution of long-wavelength (small q) modes h_q , which are less unstable than h_{q^*} . This implies that the maximum of the PSD takes place at a value of q_x which is smaller than q_{x^*} . The linear wavelength selection mechanism still holds, but it takes some time for the amplitude h_{q^*} to eventually dominate those of competing Fourier modes. Such a process is seen as a shift in the peak of the PSD towards the value corresponding to q_{x^*} . In real space, it is perceived as a decrease in the ripple wavelength with time. Naturally, different initial (pristine) conditions may lead to different behaviors from this point of view. Moreover, the larger time and length scales associated with medium-energy irradiation as compared with low-energy experiments may justify the lack of reports of a similar behavior in the latter class of systems, for which the effect may be hard to resolve.

4.5 Conclusions

We have carried out extensive studies on 60 keV Ar⁺-ion induced morphological evolution on Si surface as a function of ion angle of incidence as well as ion fluence. Our study revealed hitherto unobserved aspects of ion-beam induced pattern evolution in the medium energy regime. In particular, we detected a decreasing trend in ripple wavelength with ion fluence in the initial stage of morphological evolution for 60 keV Ar⁺-ions at RT. We have also shown a coarsening of ripple wavelength which follows in the later stage of ripple evolution with ion fluence. Moreover, our experiment demonstrated formation of ripple patterns from angle of incidence of 45° showing that this is the critical angle for pattern formation under the present conditions. From a statistical analysis of the surface morphologies, we have clearly distinguished linear and nonlinear regimes for the observed ripple patterns in the present case. In doing so, we have been able to point out that the decrease in ripple wavelength is a phenomenon that takes place in the linear regime. From our experimental results and those available in the literature, we have created a parametric phase diagram

which summarizes an overview of pattern formation on silicon surface under medium energy ion irradiation. On the basis of this phase diagram we have shown some striking similarities between ripple patterns in low and medium energy regimes in order to make an attempt to understand whether similar mechanisms are responsible for pattern formation in both the regimes. Upon comparing the experimental results (in the linear regime) with our theoretical estimations, we have shown that in contrast to the dominance of ion-induced atomic redistribution process in case of low energy ion-induced ripple evolution on Si (as interpreted by Madi *et al.* [30]), both curvature-dependent sputter erosion and atomic redistribution are operative for medium energy ion-induced ripple evolution. Our result agrees well with recent predictions of Hofsäss [38] where he showed the relevance of both sputter erosion and redistribution effects in surface pattern formation under energetic ion irradiation of Si.

To understand decreasing trend in ripple wavelength at the early stage of evolution, we have carried out numerical simulations of a linear continuum model of ion irradiated surface evolution. Such a model has been assessed experimentally for Si irradiation at low ion energies. Comparison between the simulation and experimental results indicates that the time-dependent behavior of the ripple wavelength is due to the influence that the shape of the pristine surface has during the early stages of pattern formation. Although Eq. 4.2 is known to lead a time-independent behavior of the ripple wavelength for the case of ideally flat initial conditions, it is likewise known to lead to time-dependent behavior in the presence of additional effects, such as e.g. conserved noise, which have also been assessed in experiments of interface dynamics at the nanoscale [44]. Thus, the shape of the initial condition appears as an additional ingredient for the design of patterns with desired morphological characteristics. In particular, the length scales associated with ripples formed at medium-energy ion irradiation can aid to obliterate the limitation to probe the variation in pattern dimension which is encountered in low-energy experiments.

Bibliography

1. M. Castro, R. Gago, L. Vázquez, J. Muñoz-García, and R. Cuerno, *Phys. Rev. B* 86 (2012) 214107.
2. D.P. Datta and T.K. Chini, *Phys. Rev. B* 76 (2007) 075323.
3. A. Biermanns, U. Pietsch, J. Grenzer, A. Hanisch, S. Facsko, G. Carbone, and T.H. Metzger, *J. Appl. Phys.* 104 (2008) 044312.
4. T. Basu, J.R. Mohanty, and T. Som, *Appl. Surf. Sci.* 258 (2012) 9944.
5. T. Basu and T. Som, *Appl. Surf. Sci.* 310 (2014) 142.
6. C.S. Madi and M.J. Aziz, *Appl. Surf. Sci.* 258 (2012) 4112.
7. A. Keller, R. Cuerno, S. Facsko, and W. Möller, *Phys. Rev. B* 79 (2009) 115437.
8. J. Erlebacher, M.J. Aziz, E. Chason, M.B. Sinclair, and J.A. Floro, *Phys. Rev. Lett.* 82 (1999) 2330.
9. J.F. Ziegler, J.P. Biersack, and K. Littmark, *The stopping and Range of Ions in Matter*. 1985, Pergamon, New York. p. See also "<http://www.srim.org/>".
10. Nanotec, *WSxM Software The Nanotechnology Research Tool*. p. <http://www.nanotec.es/products/wsxm/>.
11. D.P. Datta and T.K. Chini, *Phys. Rev. B* 69 (2004) 235313.
12. S.K. Garg, V. Venugopal, T. Basu, O.P. Sinha, S. Rath, D. Kanjilal, and T. Som, *Appl. Surf. Sci.* 258 (2012) 4135.
13. T. Basu, D. Datta, and T. Som, *Nanoscale Res. Lett.* 8 (2013) 289.
14. D.P. Datta and T.K. Chini, *Phys. Rev. B* 71 (2005) 235308.
15. G. Carter, *J. Appl. Phys.* 85 (1999) 455.
16. R.M. Bradley and J.M.E. Harper, *J. Vac. Sci. Technol. A* 6 (1988) 2390.
17. R. Cuerno, M. Castro, J. Muñoz-García, R. Gago, and L. Vázquez, *Nucl. Instrum. Methods Phys. Res. B* 269 (2011) 894.

18. C.C. Umbach, R.L. Headrick, and K.-C. Chang, *Phys. Rev. Lett.* 87 (2001) 246104.
19. M.A. Makeev, R. Cuerno, and A.-L. Barabási, *Nucl. Instrum. Methods Phys. Res. B* 197 (2002) 185.
20. J. Muñoz-García, R. Cuerno, and M. Castro, *Phys. Rev. B* 78 (2008) 205408.
21. T.K. Chini, D.P. Datta, and S.R. Bhattacharyya, *J. Phys.: Condens. Matter* 21 (2009) 224004.
22. T.K. Chini, M.K. Sanyal, and S.R. Bhattacharyya, *Phys. Rev. B* 66 (2002) 153404.
23. G. Carter and V. Vishnyakov, *Phys. Rev. B* 54 (1996) 17647.
24. T. Kumar, U.B. Singh, M. Kumar, S. Ojha, and D. Kanjilal, *Curr. Appl. Phys.* 14 (2014) 312.
25. S.K. Mohanta, R.K. Soni, S. Tripathy, C.B. Soh, S.J. Chua, and D. Kanjilal, *Physica E* 35 (2006) 42.
26. C.S. Madi, B. Davidovitch, H.B. George, S.A. Norris, M.P. Brenner, and M.J. Aziz, *Phys. Rev. Lett.* 101 (2008) 246102.
27. R. Gago, L. Vázquez, R. Cuerno, M. Varela, C. Ballesteros, and J.M. Albella, *Appl. Phys. Lett.* 78 (2001) 3316.
28. B. Ziberi, F. Frost, T. Höche, and B. Rauschenbach, *Vacuum* 81 (2006) 155.
29. R. Gago, A.J. García-Sánchez, A. Cubero-Redondo, and L. Vázquez, *Surface Nanopatterns on Si(100) by Normal-Incidence Ion Sputtering with Metal Incorporation*, in *Nanofabrication by Ion-Beam Sputtering: Fundamentals and Applications*, T. Som and D. Kanjilal, Editors. 2012, Pan Stanford: Singapore. p. 163.
30. C.S. Madi, E. Anzenberg, K.F. Ludwig, Jr., and M.J. Aziz, *Phys. Rev. Lett.* 106 (2011) 066101.
31. J. Vajo, R. Doty, and E.-H. Cirlin, *J. Vac. Sci. Technol. A* 14 (1996) 2709.

32. E. Chason, T. Mayer, B. Kellerman, D. McIlroy, and A. Howard, *Phys. Rev. Lett.* 72 (1994) 3040.
33. U. Valbusa, C. Boragno, and F.B.d. Mongeot, *J. Phys.: Condens. Matter* 14 (2002) 8153.
34. D. Flamm, F. Frost, and D. Hirsch, *Appl. Surf. Sci.* 179 (2001) 95.
35. B. Ziberi, F. Frost, T. Höche, and B. Rauschenbach, *Phys. Rev. B* 72 (2005) 235310.
36. A. Toma, F. Buatier de Mongeot, R. Buzio, G. Firpo, S. Bhattacharyya, C. Boragno, and U. Valbusa, *Nucl. Instrum. Methods Phys. Res. B* 230 (2005) 551.
37. W.L. Chan and E. Chason, *J. Appl. Phys.* 101 (2007) 121301.
38. H. Hofsäss, *Appl. Phys. A* 114 (2014) 401.
39. W. Eckstein, R. Dohmen, A. Mutzke, and R. Schneider, *IPP Report* 12 (2007).
40. S.K. Garg, D.P. Datta, M. Kumar, D. Kanjilal, and T. Som, *Appl. Surf. Sci.* 310 (2014) 147.
41. R. Cuerno, H.A. Makse, S. Tomassone, S.T. Harrington, and H.E. Stanley, *Phys. Rev. Lett.* 75 (1995) 4464.
42. J. Muñoz-García, R. Gago, R. Cuerno, J.A. Sánchez-García, A. Redondo-Cubero, M. Castro, and L. Vázquez, *J. Phys.: Condens. Matter* 24 (2012) 375302.
43. T. Da Silva and J. Moreira, *Phys. Rev. E* 56 (1997) 4880.
44. R. Fetzer, M. Rauscher, R. Seemann, K. Jacobs, and K. Mecke, *Phys. Rev. Lett.* 99 (2007) 114503.

CHAPTER 5

5 Microstructural investigation of ripple-patterned surfaces

5.1 Introduction

In Chapter 4, patterns formed on Si surface were understood in terms of energy deposition by the incident ions and related surface processes, e.g. ion-induced effective surface tension, surface diffusion etc. However, the energy loss of incident ions due to collisions with target atoms leads to considerable structural damage, as described in Chapter 1. The accumulation of damage with increasing ion fluence can finally result in transition of a crystalline structure to an amorphous one. The depth up to which ion damage is distributed is dependent upon energy and angle of incidence of the incoming ions. Moreover, incorporation of incident ions into the target matrix leads to significant compositional modifications of the target. Therefore, structural and compositional modification of the target is expected to play an important role in the evolution of surface patterns under ion irradiation. For instance, Castro *et al.* have shown the formation of an amorphous layer to be a prerequisite for pattern formation [1]. Formation of a top amorphous layer with a modulated amorphous/crystalline (*a/c*) interface has been revealed, both for low [2-4] as well as medium energy ion induced ripple patterns on surface, as a function of ion-fluence [5-7] and -energy [8]. Recently, Kumar *et al.* [5-7] have proposed that the ripple formation process actually starts from the (*a/c*) interface. On the other hand, compositional study of 2-10 keV O⁺ ion-induced ripple patterned Si [9] revealed the inhomogeneity of oxygen atoms across the ripple structure and its role on pattern formation. Compositional variation over the ripple patterned Si surface was also demonstrated by Datta *et al.* [10]. In contrast to the mechanism proposed by Kumar *et al.*

[5-7], Madi *et al.* [4] argued that interface has no role over low energy ion induced pattern formation. Investigation of microstructure and composition of ripple patterned surface and their role in pattern evolution is, therefore, highly important for a deeper understanding of the patterning process. Medium energy ion irradiation results in formation of a top amorphous layer which is much thicker than that generated by low-energy ion irradiation and thus, provides an ideal platform to study the effect of ion-damaged layer in patterning. In this chapter we describe our experimental investigations on the microstructure and composition of medium energy Ar⁺-ion irradiated Si as a function of ion-fluence and -angle of incidence. From our experimental results and numerical estimations of damage accumulation by incident ions into the target, we show a correlation of ripple wavelength with the thickness of the amorphous layer. Subsequently, we illustrate that the energy scaling of the layer thickness and ripple wavelength can be qualitatively understood in terms of nuclear energy loss of incident ions.

5.2 Experimental Details

The compositional and microstructural investigations were carried out on Si samples irradiated with 60 keV Ar⁺-ions to fluences of $5\text{-}30 \times 10^{17}$ ions cm⁻² over a wide angular window (0°-75°). The ripple morphology developed on the irradiated samples was described in Chapter 4. This fluence range has been selected for the present studies because the evolution of ripple morphology belongs to the linear regime in this range, as described in Chapter 4, in contrast to studies by Datta *et al.* [10] where the patterns belonged to the nonlinear regime.

Micro-Raman measurements on these samples were performed at room temperature in backscattering geometry by using the setup described in Chapter 2. Excitation wavelengths of 488 nm, 514.5 nm, and 532 nm from an argon ion laser were used for the Raman studies. Crosssectional transmission electron microscopy (XTEM) was employed to study

microstructure of selected patterned surfaces by using a high-resolution JEOL-TEM facility operating at 200 kV. Energy dispersive X-ray spectroscopy (EDS) (attached in the same TEM setup) studies were also performed for the same specimen to study the elemental composition as a function of depth. In addition, Rutherford backscattering spectrometry (RBS) measurement of the ripple patterned Si was carried out using 2 MeV He⁺ ion-beam.

5.3 Results

5.3.1 Micro-Raman spectroscopy

Fig. 5.1 shows the micro-Raman spectra from Si samples obtained using 514.5 nm wavelength of Argon laser before and after Ar-ion irradiation as a function of ion angle of incidence, θ . In the Raman spectrum of the pristine sample, we observe a sharp peak at 521 cm⁻¹ which corresponds to zone-center optical phonon O(*T*) mode of crystalline (*c*-Si) [11]. In case of normally incident argon ions, the Raman signal shows a broad peak at 480 cm⁻¹ which corresponds to transverse optic (TO) mode of amorphous (*a*-Si) [11].

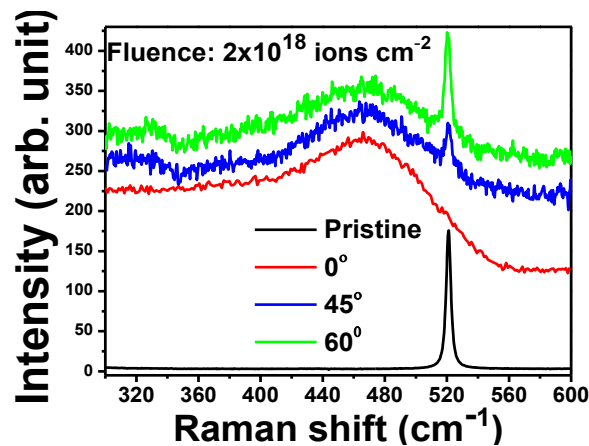


Figure 5.1: Room temperature micro-Raman spectra of pristine and 60 keV Ar-ion irradiated (fluence 2×10^{18} ions cm⁻²) of the silicon samples at different angles of incidence.

It is observed from Fig. 5.1 that while the Raman spectrum of the sample irradiated under normally incident argon ions shows the signature of amorphous silicon, the peak at 521 cm⁻¹ corresponding to crystalline silicon also becomes prominent with increasing incident angle. This can be attributed to the reduced projected range of argon ions at higher incident angles

which leads to the formation of a thinner top amorphous layer such that the laser beam used for excitation probes the underlying crystalline Si, as will be described below.

Fig. 5.2(a) shows the micro-Raman spectra of Ar⁺ irradiated samples at $\theta=60^\circ$ as a function of ion fluence for the two different laser wavelength of 532 nm and 488 nm. For both of the excitation wavelengths, a narrow peak at 521 cm⁻¹ and a broad peak at 480 cm⁻¹ appear for all the ion fluences under consideration. The *c*-Si peaks for excitation wavelength 532 nm is found to be more pronounced compare to the peak for excitation wavelength of 488 nm at all fluences while the intensity of these peaks are found to be constant with ion fluence for both the excitation wavelengths. The quantitative analysis of the amorphous layer depth can be performed by calculating the probing depth of a laser line inside the material. The maximum probing depth of laser inside a material is approximately given by $1/2\alpha(k)$, where $\alpha(k)$ is the optical absorption coefficient for the corresponding laser line wavelength, $2\pi/k$ [12,13]. From the above relation, the maximum probing depth of Ar-ion laser of wavelength 532 nm is found to be 770 nm and 100 nm for *c*-Si and *a*-Si, respectively, whereas for the excitation wavelength of 488 nm, it is found to be 72 nm in *a*-Si [12,13]. Thus, from the presence of *c*-Si peak in the Raman spectrum, corresponding to the excitation wavelength of 532 nm, and absence of the same for excitation wavelength of 488 nm, we infer that the thickness of the top amorphous layer of the irradiated samples is below 100 nm and close to 72 nm. On the other hand, constant *c*-Si peak for all fluences at both the probing laser wavelength, indicates that the thickness of the amorphous layer remains constant with fluence.

For $\theta=75^\circ$, the intensity of the Raman peak corresponding to *c*-Si (at 488 nm laser line) remains constant in the entire fluence range used in our experiment [as observed from Fig. 5.2(b)]. The intensity of the peak is also higher than the same for $\theta=60^\circ$. These observations also suggest that the thickness of the ion-induced amorphous layer decreases at higher angle of incidence. In addition, information about the stress could be extracted by observing the

shift in the *c*-Si peak (at 521 cm⁻¹) of Raman spectra. The fact that no shift in the *c*-Si peak was observed compared to the pristine sample in Fig. 5.2(b) indicates that the residual stress is limited to a maximum value of 190 MPa [14] corresponding to the detection limit (0.4 cm⁻¹) of used Raman spectrometer.

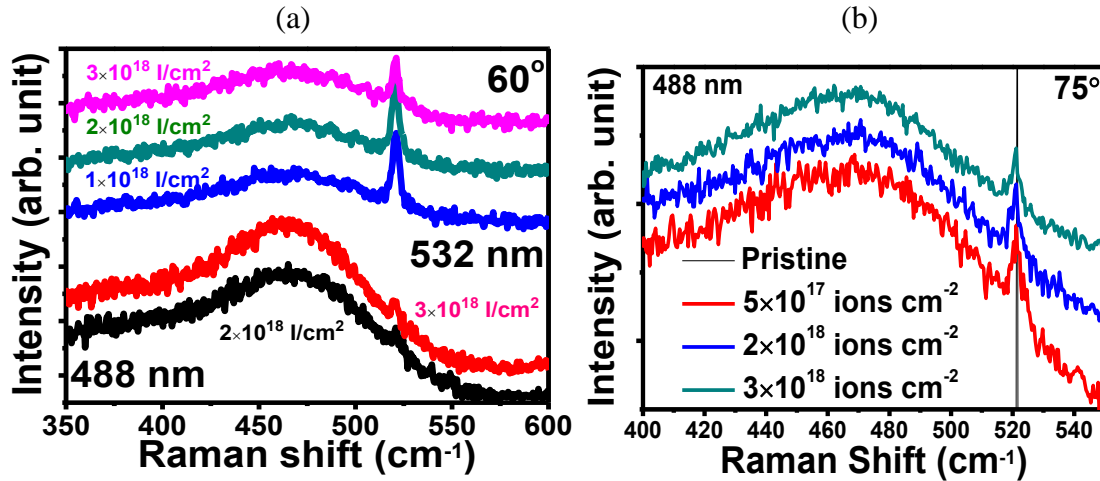


Figure 5.2: The micro-Raman spectra of Ar⁺-ion irradiated Si samples as a function of ion fluence for (a) $\theta=60^\circ$ for excitation lines of 532 and 488 nm and (b) $\theta=75^\circ$ for excitation line of 488 nm.

5.3.2 TEM & EDS study

Figs. 5.3(a) and (b) show the XTEM images of Ar-ion irradiated Si at $\theta=45^\circ$ for fluence 2×10^{18} ions cm⁻². Formation of a top amorphous layer with an (*a/c*) interface modulated parallel to the top surface is clearly visible in Fig. 5.3(a). The thickness of the amorphous layer is measured to be 120 nm and 100 nm for the front and back slope of the ripple patterns, respectively, as indicated on the image. A closer inspection of the XTEM image in Fig. 5.3(b), taken at a higher magnification, reveals the presence of bubbles in the amorphous layer, where the bubble diameter decreases from the top surface towards the interface. In addition, a ~5 nm thick top layer of different contrast is discernible in Fig. 5.3(b), which is, presumably, the native oxide layer formed on Si. To investigate the composition of the bubbles seen in the amorphous layer [Fig. 5.3(b)], EDS spectra were collected across the amorphous layer, at the points shown in Fig. 5.3(b). From the EDS data, we observe that the cavities/bubbles contain Ar and its atomic percentage at different points is plotted in Fig.

5.3(c). From the comparison of Figs. 5.3(b) and (c), we find that an appreciable amount of Ar atoms is present in the amorphous Si layer, extended up to a depth of 60 nm.

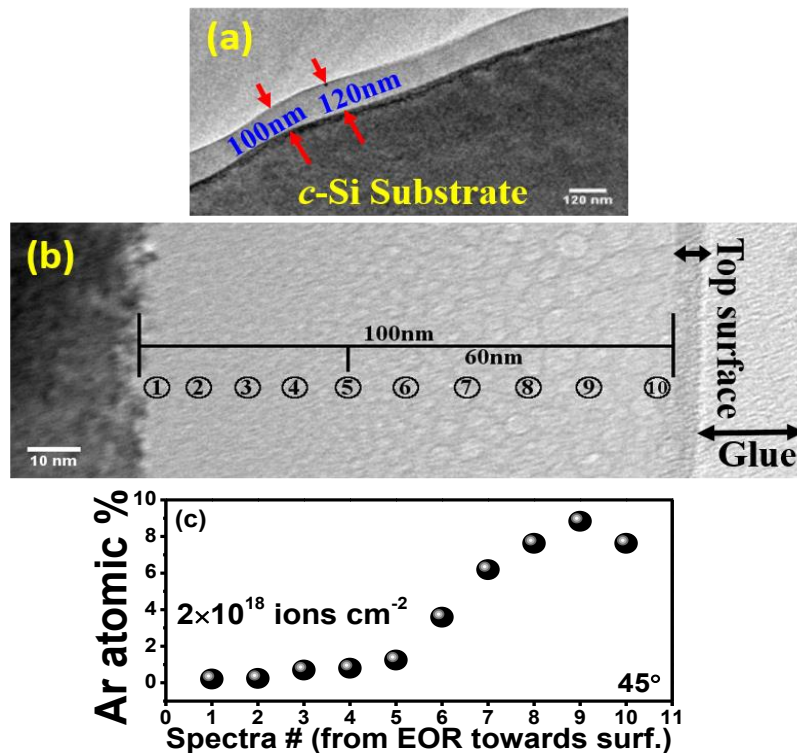


Figure 5.3: (a) and (b): XTEM images of a Si sample irradiated at $\theta=45^\circ$ for fluence $2 \times 10^{18} \text{ ions cm}^{-2}$ but taken at two different magnifications, (c) EDS analysis: Plot of Ar atomic percentage as a function of depth in the amorphous region shown in (b).

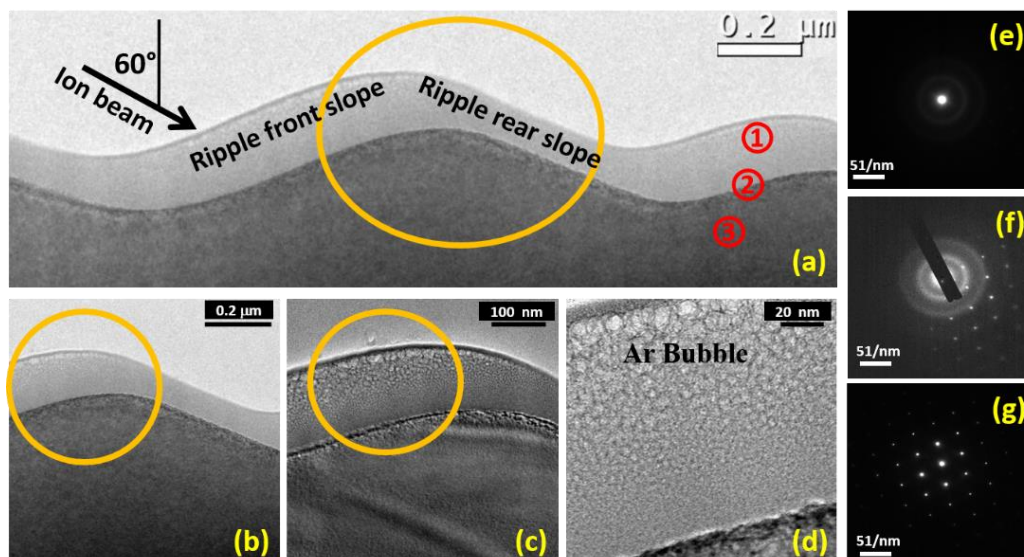


Figure 5.4: (a) XTEM image of an irradiated Si sample at $\theta=60^\circ$ and to the fluence of $3 \times 10^{18} \text{ ions cm}^{-2}$, (b) a zoomed view of the marked region in (a), (c) a zoomed view of the marked region in (b), (d) a zoomed XTEM image of the marked region in (c), (e)-(g) are SAED (selected area electron diffraction) images taken from the regions 1, 2, and 3 shown in (a) respectively.

XTEM images of Si irradiated at $\theta=60^\circ$ to the fluence of 3×10^{18} ions cm^{-2} is shown in Fig. 5.4(a). The existence of parallel modulation at the surface and the (*a/c*) interface is evident here. The front and rear slopes of the ripple pattern are indicated in Fig. 5.4(a). From the XTEM image presented in Fig. 5.4(b), the thickness of the amorphous layer is measured to be 120 nm and 70 nm at the front and rear slope of the ripple, respectively. XTEM images, taken at higher magnification, are shown in Figs. 5.4(c) and (d). While the bubbles are found to be concentrated near the front slope of the ripples, the diameter of these bubbles are found to decrease as one moves towards the *a/c* interface which is similar to the case of $\theta=45^\circ$. The SAED patterns obtained from the regions marked as ‘1’, ‘2’, and ‘3’ on Fig. 5.4(a) are shown in Figs. 5.4(e)-(g). The diffused rings in Fig. 5.4(e) clearly show the amorphous nature of the top layer. On the other hand, SAED pattern in Fig. 5.4(g) shows the presence of ordered spots, which originate from the underlying crystalline Si substrate below the (*a/c*) interface. Fig. 5.4(f) depicts the presence of both amorphous and single crystalline material. This is quite expected for an *a/c* interface.

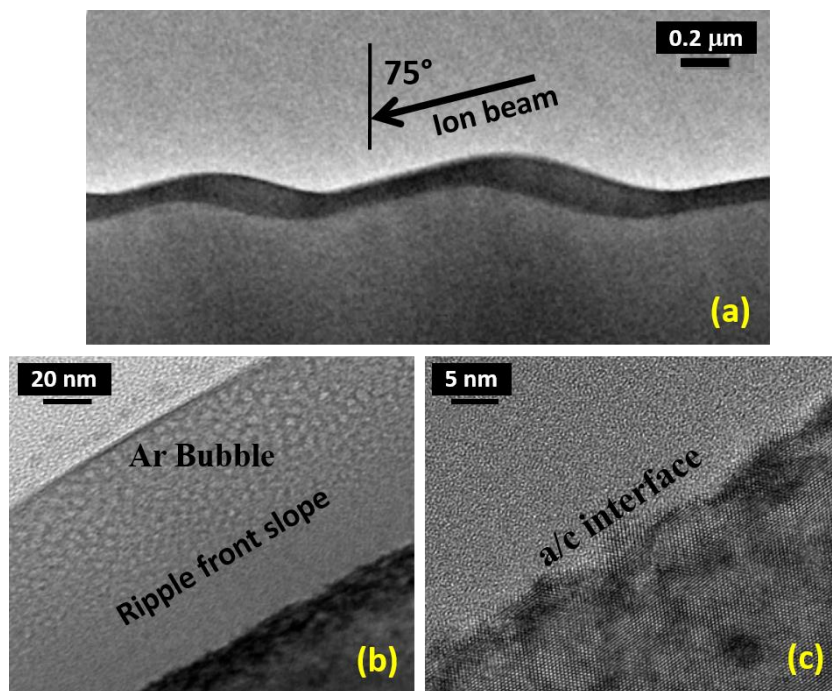


Figure 5.5: (a) XTEM image of irradiated Si irradiated at $\theta=75^\circ$ to the fluence of 3×10^{18} ions cm^{-2} , (b) XTEM image of the front slope of one ripple shows the presence of Ar bubbles, (c) high-magnification image of the (*a/c*) interface.

XTEM images of Si irradiated at $\theta=75^\circ$ to the fluence of 3×10^{18} ions cm^{-2} is shown in Fig. 5.5. Similar to the cases of $\theta=45^\circ$ and 60° , a top amorphous layer with an (*a/c*) interface modulated parallel to the top surface is observed in 5.5(a). The thickness of the amorphous layer is found to be 105 nm and 60 nm for the front and rear slope of the ripple patterns, respectively. In addition, bubble diameters are lower at $\theta=75^\circ$ compared to $\theta=60^\circ$, as is evident from Figs. 5.5(b) and 5.4(d).

5.3.3 RBS study

Fig. 5.6 shows the RBS spectra of irradiated Si samples to the fluence 3×10^{18} ions cm^{-2} at (a) $\theta=60^\circ$ and (b) $\theta=75^\circ$. Depth dependent compositional analysis were performed by fitting the RBS spectra using the XRUMP simulation code [15]. The fit to the data has been shown in the corresponding figures. A good fit to the RBS spectrum in Fig. 5.6(a) could be obtained considering a Si layer where 12% of Ar atoms are present up to a depth of 60 nm.

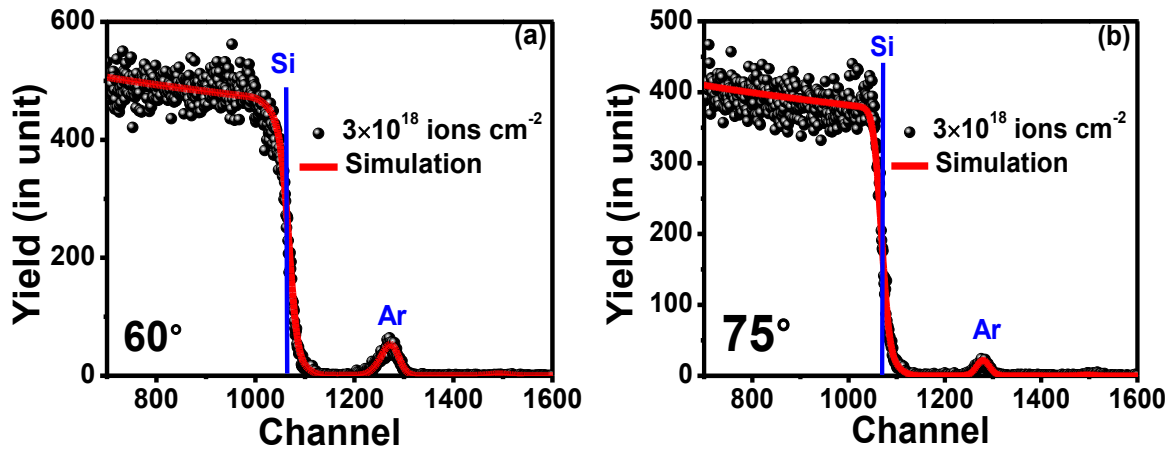


Figure 5.6: Experimental and simulated RBS spectra of irradiated Si samples to the fluence 3×10^{18} ions cm^{-2} at incident angles (a) 60° and (b) 75° .

A good fit to the observed RBS spectrum in Fig. 5.6(b) is obtained considering a single layer of Si where 11% of Ar atoms are present up to a depth of 25 nm. Integration of the simulated Ar atom peaks in the RBS spectra [Figs. 5.6(a) and (b)] reveals the areal density of Ar atoms to be 3×10^{16} atom cm^{-2} , and 1×10^{16} atom cm^{-2} at $\theta=60^\circ$ and 75° , respectively.

5.4 Discussion

The absence of any peak at 501 cm^{-1} in Figs. 5.1 and 5.2, rules out the possibility of the presence of Si nanocrystallites in the amorphous layer generated by Ar-ion irradiation, as found by XTEM analysis. This is in contrast to the results reported by Mohanta *et al.* [16]. In addition, the observed limiting stress value of 190 MPa, obtained from Raman data under the present experimental conditions is found to be much less compared to low energy ion-induced residual stress in an amorphous layer (1.6 GPa) [17]. One order of less residual stress value observed in our experimental condition could be very useful to govern the wavelength of ripple pattern as was discussed earlier (in Eq. 3.46). On the other hand, variation in thickness of the amorphous layer can be understood in terms of change in local incidence angle (as described by Chini *et al.*) [8].

It is evident from the RBS analysis that thickness of the layer containing Ar atom and the areal density of implanted Ar atom decrease with increasing angle of incidence. Moreover, areal density of Ar is found to be almost two orders of less compared to the applied fluence. This could be the outcome of two processes. Firstly, range of incident ions decreases with increasing angle, which may leave more Ar atom in the vicinity of the surface. Secondly, these implanted Ar atoms may diffuse to the ambient through the surface. Further, appearance of only Ar peak in both the RBS spectra rule out the possible presence of any metal impurity in our irradiated Si sample.

5.4.1 Correlation of the amorphous layer with ripple wavelength

Experimentally, it is found that ripple wavelength strongly depends on energy of the incident ions. At very low energies, namely 250-400 eV, ripple wavelength, λ , is reported to be constant although fluctuation in its value increases with ion energy [4]. In the energy range higher than this, it has been observed experimentally that the ripple wavelength varies with incident ion energy E as [18-21]:

$$\lambda \propto E^p, \quad (5.1)$$

In order to investigate the correlation of ripple wavelength with depth distribution of ion energy deposition and resulting formation of an amorphous layer, we estimated damage deposition depth a (peak position of ion energy distribution in the target), corresponding straggling of the distribution σ , and projected range R_p for Ar^+ -ion irradiation in Si as a function of energy, using SRIM simulation [22]. The parameters a , σ , and R_p are plotted in Fig. 5.7 where all the parameters are found to increase with incident ion energy. According to the basic mechanism of ion-solid interaction discussed in chapter 1, the parameters a , σ , and R_p are expected to follow a power law behavior $\propto E^{2m}$ (Eq. 1.13). Two different values of the exponent $2m$, namely 0.66 and 1.0 are expected (Eq. 1.10) at the low energy regime (where nuclear energy loss is dominant) and the medium energy regime (where both nuclear and electronic energy losses are comparable), respectively. It is thus, clear that all the parameters a , σ , R_p , and ripple wavelength λ of ion induced ripple pattern [23] varies with increasing ion energy following a power law.

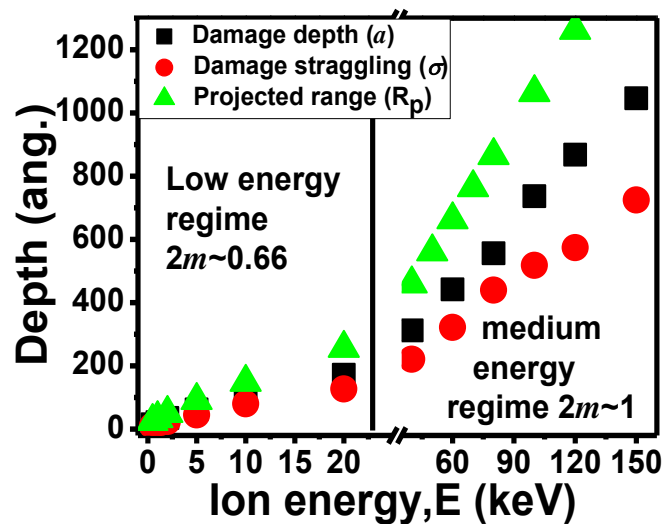


Figure 5.7: SRIM simulated depth of energy deposition a , straggling of deposited energy distribution σ , and projected ion range R_p at 0° incidence angle, as a function of ion energy. The black vertical line separates low and medium energy regimes.

We have shown in Chapter 4 that ripple wavelength λ decreases with increasing ion angle of incidence θ . Our experimental results described in this chapter show that the depth of the amorphous layer also decreases with ion angle of incidence. On the other hand, both the

ripple wavelength λ , damage deposition depth a , and projected range R_p increases with ion energy, as described above. In fact, in the present analysis we have found that the ratio of the ripple wavelength and projected range, λ/R_p is constant. This indicates a direct relationship of ripple wavelength with the depth of amorphous layer. However, the magnitude of a or R_p does not agree well with the observed thickness of the ion-generated amorphous layer, especially in case of rippled surface where amorphous depth varies from the front to the rear slope [8]. Therefore, for our subsequent analysis, we estimate the average thickness of the amorphous layer, under the assumption of symmetric ripple morphology [24], i.e., the amorphous layer is assumed to be of uniform thickness [10]. The validity of this assumption in understanding ripple evolution was supported by recent experimental findings of Kumar *et al.* [7]. In this assumption, the average thickness of the amorphous layer is given by

$$d = (\text{thickness in front slope} + \text{thickness in rear slope})/2, \quad (5.2)$$

From our XTEM studies (Fig. 5.4), the average thickness of the amorphous layer is calculated to be $\frac{120+70}{2} = 95$ nm for 60 keV Ar⁺-ion irradiation in Si at $\theta=60^\circ$. Likewise, the average thicknesses of the amorphous layers (extracted from XTEM analysis of Figs. 5.3 and 5.5.) are found to be 110 nm and 83 nm for ion incidence angle 45° and 75° , respectively.

To estimate the average depth, d , of the amorphous layer at different ion energies, we use the method adopted by Chini *et al.* [8] to calculate the thickness of ion-induced amorphous layer at the front and rear slopes of ripple patterns by using SRIM simulation. According to their formalism, thickness of the amorphous layers is given by $R_p+3\Delta R_p$ and $R_r+3\Delta R_r$ at the front and the back slope of a ripple pattern, respectively. Here, R_p and R_r are the projected ion range and radial range, respectively where ΔR_p and ΔR_r are straggling in R_p and R_r . We estimated the average thickness of the amorphous layer, as a function of ion energy from Eq. 5.2 where the values of R_p , ΔR_p , R_r , and ΔR_r at each energy are determined from SRIM simulation. The average thickness of the amorphous layer for 60 keV Ar⁺-ions incident on Si

at 60° angle of incidence turns out to be 101 nm, which is close to the value of 95 nm, as estimated from the experimental data by using Eq. 5.2 (described above). It can be mentioned that average depth of the amorphous layer estimated by this method agrees with experimentally obtained data for ion energy $E = 50$ and 120 keV as well [8]. In the following, we further illustrate the correlation of energy scaling of ripple wavelength with average depth of amorphous layer d .

5.4.2 Energy scaling of ripple wavelength: Role of nuclear energy loss

Experimentally, the value of p in Eq. 5.1 is found to be 0.5-1 for 0.25-2 keV Ar⁺-ion bombardment on SiO₂ [19]. For O⁺-ion bombardment of Si in the energy range 1.5-10 keV, p was found to be ≈ 0.8 [20]. On the other hand, Biermanns *et al.* [21] reported the value of p to be ≈ 1 and 0.5 at ion incidence angle of 65° and 70°, respectively, for 5-40 keV Xe⁺-ion bombardment on Si. It appears from these experimental results that the value of p decreases with increasing ion energy. Theoretically, solid flow model predicts a power-law relationship between ripple wavelength and ion energy, $\lambda \propto E^p$ [18], where the value of p is given by

$$p = 7/12 + m, \quad (5.3)$$

When we put the theoretical value of m (obtained from Eq. 1.10 or Fig. 5.7) in Eq. 5.3, values of $p \sim [0.93, 1.08]$ estimated from solid flow model deviates from the experimentally observed ones ($p < 0.93$) [23] for the medium energy range, although better agreement is found with experimental value ($p \sim 1$) in the low energy regime.

We have shown in Chapter 4 that ripple pattern formed on Si under medium energy Ar⁺-ion irradiation is an outcome of both curvature-dependent sputtering and prompt atomic redistribution. Therefore, we attempt to understand the experimentally observed energy scaling of ripple wavelength in the medium energy regime considering the contributions of sputtering and atomic redistribution, where wavelength of ripple pattern is given by [25,26]

$$\lambda = 2\pi \left(\frac{2\kappa}{|v|} \right)^{1/2}, \quad (5.4)$$

Here, ν and κ are ion induced effective surface tension and relaxation term, respectively. The relaxation processes include ion induced viscous flow, D_{IVF} , [19] and ion induced effective surface diffusion, D_{EDS} , [27] which are dependent upon d and a , respectively. Specifically, ion induced viscous flow $D_{IVF} \sim d^3$ [19] and effective surface diffusion, $D_{ESD} \sim a^3$ [27,28]. On the other hand, ion induced surface tension is constituted by two terms [29]

$$\nu = Jan\Gamma Y_{\theta} + J\delta n \cos 2\theta, \quad (5.5)$$

In Eq. 5.5, a and δ (forward mass distribution parameter) [26,29] are the main parameters which vary with energy, while other parameters (ion flux j , target atomic density n , angle of incidence θ , and curvature-dependent sputtering yield, ΓY_{θ}) either weakly depend on energy or remain constant. Thus, by using Eq. 5.5 and the dependence of κ on d and a , we can write Eq. 5.4 in the following manner

$$\lambda = 2\pi \left(\frac{a^3}{|Jan\Gamma Y_{\theta} + J\delta n \cos 2\theta|} \right)^{1/2}, \quad (5.6)$$

To understand the behavior of ripple wavelength with energy, one must know the energy dependence of a and δ . We have estimated δ [26,29] as a function of ion energy by using SRIM simulation.

Energy dependence of a is shown in Fig. 5.7 along with other parameters. As discussed above, wavelength of ion induced ripples is found to depend on the thickness of ion-induced amorphized top layer, which does not match well with a and we consider the average depth of amorphous layer, d , as defined above. Since d is defined in terms of R_p , it must scale with ion energy similar to that of R_p . Our estimated values of δ and d are plotted as a function ion energy in Fig. 5.8(a) along with the ripple wavelength (λ) reported in Ref. [30]. From a power law fit of the parameters ($\delta, d, \lambda \sim E^{2m}$) in Fig. 5.8(a), we have estimated the values of the exponent $2m$ for δ and d to be 0.72 and 0.62 for low energy regime (0.5-20 keV), and 0.63 and 0.78 for medium energy regime (20-150 keV), respectively. It is clear that the exponent values for δ and d deviate from theoretically expected value of 1.0 for medium energy regime

while they are close to theoretically predicted value of 0.66 in the low energy regime. Moreover, since both δ and d follow the power law behavior with ion energy, Eq. 5.6 can be written as

$$\lambda \sim \left(\frac{a^3}{a+\delta} \right)^{1/2} \sim \left(\frac{E^{6m}}{E^{2m}+E^{2m}} \right)^{1/2} \sim E^{2m}, \quad (5.7)$$

This relation further asserts that the ripple wavelength varies as a power law with incident ion energy. In the medium energy regime, wavelength should vary with ion energy $\lambda \sim E$ ($2m=1$), which contradicts our SRIM simulation based estimation $\lambda \sim E^{0.79}$ (shown in Fig. 5.8(a)). However, the fact that the value of the exponent 0.79 is very close to the exponents found for d further strengthens the relation between ripple wavelength and depth of the amorphous layer.

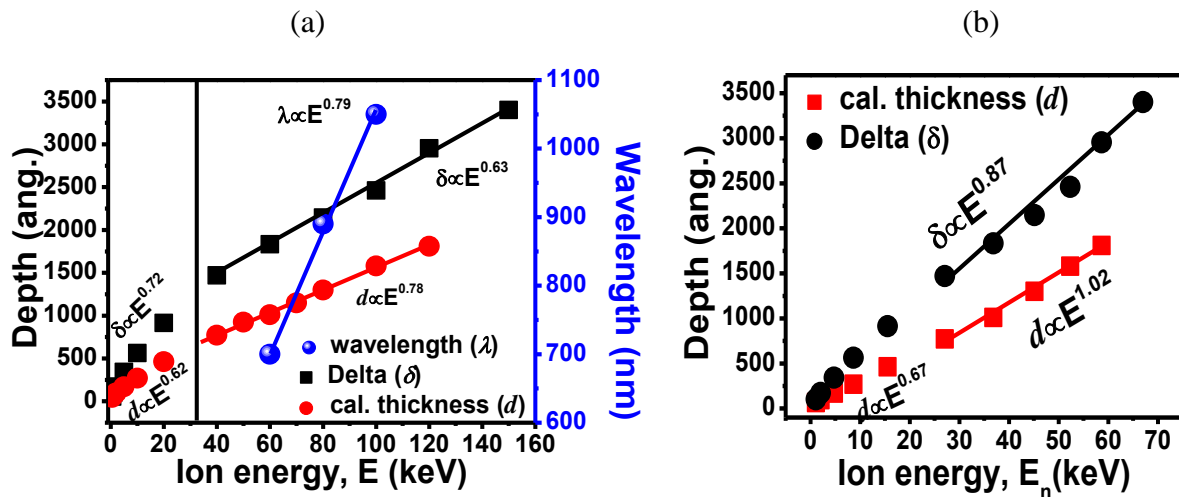


Figure 5.8: Forward mass distribution parameter δ and average depth of amorphous layer d , as simulated using SRIM, as a function of (a) Ar-ion incident energy E and (b) nuclear energy loss, E_n , of Ar-ions in Si. The black vertical line separates low and medium energy regime. Ripple wavelength is also plotted as a function of ion energy where the right Y-axis shows the value of wavelength [30].

Now we consider the fact that the formation of a top amorphous layer in this energy regime is predominantly caused by nuclear energy loss of incident ions. Thus, we calculated the energy dissipated in nuclear collision (nuclear energy loss) for different incident ion energies by using SRIM. In Fig. 5.8(b), δ and d values are plotted against this effective energy loss (i.e.,

nuclear energy loss). From power-law fits of δ and d , the values of the exponents ($2m$) are found to be 0.87 and 1.02, respectively, in the energy range of 20-150 keV. These observed values are close to theoretically estimated value of 1 in this energy regime [31]. It indicates that instead of total incident ion energy only the effective energy loss should be considered in theoretical calculation as far as energy scaling of the parameters is concerned.

As mentioned above for solid flow model [18] (In Eq. 5.3), the value of p (~ 1.08) deviates from the experimentally observed ones (~ 0.45) [23] for the medium energy regime, although a better agreement is found with experimental value [$p \sim 0.93 \sim 1$] in the low energy regime. At this point, we again consider the nuclear energy loss of incident ions to be effective for ripple formation, instead of total energy of the incident ions and analyze the consequences of this assumption on the value of p as predicted by solid flow model. For example, we consider our experimental conditions of 60 keV Ar-ion irradiation on Si where we use only nuclear energy loss ($E_n = 35$ keV) instead of ion incident energy ($E = 60$ keV). The value of p was estimated from Eqs. 5.1 and 5.3, in the following manner:

$$\lambda_{60 \text{ keV}} \propto E_n^{7/12+m} \propto E^p \Rightarrow p = \frac{(7/12 + m) \log E_n}{\log E}$$

$$p = \frac{(7/12+0.5) \log 35}{\log 60} = 0.93 < 1.08 \quad (5.8)$$

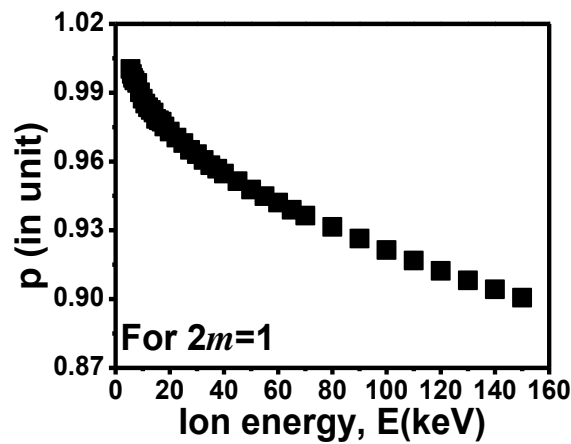


Figure 5.9: Value of the parameter p as predicted by solid flow model (Eq. 5.8) when only the nuclear energy loss of ions is considered to be effective behind ripple formation.

In Fig. 5.9 we have plotted p values obtained by this method as a function of incident ion energy. It is confirmed from Fig. 5.9 that p values show a decreasing trend towards higher energy. Although the value of p calculated for 60 keV Ar⁺-ion in Si by using only nuclear energy loss does not quantitatively agree with the observed experimental value (0.79 from Fig. 5.8(a)), it provides the exact trend of the experimentally observed variation of wavelength with energy.

5.5 Conclusion

We have carried out structural and compositional analyses of 60 keV Ar⁺-ion generated ripple patterns on Si surface in detail. Our investigations reveal the formation of a fully amorphous top-Si layer where the average thickness of the layer decreases with increasing angle of incidence. Moreover, the residual stress in the medium energy ion-induced amorphous layer is found to be an order of magnitude lower than that found for low energy ion-induced amorphous layer. Using our experimental data and SRIM-simulation-based numerical estimations, we have shown that ripple wavelength is correlated to the thickness of the amorphous layer. Further, we have shown that the experimentally observed scaling of the amorphous layer thickness can be qualitatively interpreted by assuming the nuclear energy loss as the predominant process, instead of the total energy of the ions, leading to amorphization of the top surface. We have further demonstrated the consistency of this assumption by showing qualitative agreement between our numerical estimation of the scaling of ripple wavelength with ion energy in the medium energy regime and the experimentally observed scaling.

Bibliography

1. M. Castro and R. Cuerno, *Appl. Surf. Sci.* 258 (2012) 4171.
2. S. Facsko, T. Dekorsy, C. Koerdt, C. Trappe, H. Kurz, A. Vogt, and H.L. Hartnagel, *Science* 285 (1999) 1551.
3. A. Kanjilal, S. Prucnal, M. Minniti, W. Skorupa, M. Helm, and S. Facsko, *J. Appl. Phys.* 107 (2010) 073513.
4. C.S. Madi, B. Davidovitch, H.B. George, S.A. Norris, M.P. Brenner, and M.J. Aziz, *Phys. Rev. Lett.* 101 (2008) 246102.
5. T. Kumar, A. Kumar, D. Agarwal, N. Lalla, and D. Kanjilal, *Nanoscale Res. Lett.* 8 (2013) 336.
6. T. Kumar, A. Kumar, and D. Kanjilal, *Appl. Phys. Lett.* 103 (2013) 131604.
7. T. Kumar, A. Kumar, N. Lalla, S. Hooda, S. Ojha, S. Verma, and D. Kanjilal, *Appl. Surf. Sci.* 283 (2013) 417.
8. T.K. Chini, F. Okuyama, M. Tanemura, and K. Nordlund, *Phys. Rev. B* 67 (2003) 205403.
9. Y. Homma, A. Takano, and Y. Higashi, *Appl. Surf. Sci.* 203 (2003) 35.
10. D.P. Datta and T.K. Chini, *Phys. Rev. B* 71 (2005) 235308.
11. A.T. Voutsas, M.K. Hatalis, J. Boyce, and A. Chiang, *J. Appl. Phys.* 78 (1995) 6999.
12. S.M. Sze and N.N. Ng, *Physics of semiconductor devices*. 2006: Wiley-interscience.
13. R. Braunstein, A.R. Moore, and F. Herman, *Phys. Rev.* 109 (1958) 695.
14. I. De Wolf, *Semiconductor Science and Technology* 11 (1996) 139.
15. CGS, *RUMP: A simulation package for backscattering spectra for ion beam analysis with MeV ions*, J.W. Mayer, et al., Editors.: Cornell University.
16. S.K. Mohanta, R.K. Soni, S. Tripathy, C.B. Soh, S.J. Chua, and D. Kanjilal, *Physica E* 35 (2006) 42.

17. N. Kalyanasundaram, M. Wood, J.B. Freund, and H.T. Johnson, *Mech. Res. Commun.* 35 (2008) 50.
18. M. Castro, R. Gago, L. Vázquez, J. Muñoz-García, and R. Cuerno, *Phys. Rev. B* 86 (2012) 214107.
19. C.C. Umbach, R.L. Headrick, and K.-C. Chang, *Phys. Rev. Lett.* 87 (2001) 246104.
20. J. Vajo, R. Doty, and E.-H. Cirlin, *J. Vac. Sci. Technol. A* 14 (1996) 2709.
21. A. Biermanns, U. Pietsch, J. Grenzer, A. Hanisch, S. Facsko, G. Carbone, and T.H. Metzger, *J. Appl. Phys.* 104 (2008) 044312.
22. J.F. Ziegler, J.P. Biersack, and K. Littmark, *The stopping and Range of Ions in Matter*. 1985, Pergamon, New York. p. See also "<http://www.srim.org/>".
23. T.K. Chini, M.K. Sanyal, and S.R. Bhattacharyya, *Phys. Rev. B* 66 (2002) 153404.
24. S.K. Garg, D.P. Datta, M. Kumar, D. Kanjilal, and T. Som, *Appl. Surf. Sci.* 310 (2014) 147.
25. R.M. Bradley and J.M.E. Harper, *J. Vac. Sci. Technol. A* 6 (1988) 2390.
26. G. Carter and V. Vishnyakov, *Phys. Rev. B* 54 (1996) 17647.
27. M.A. Makeev and A.-L. Barabási, *Appl. Phys. Lett.* 71 (1997) 2800.
28. M.A. Makeev, R. Cuerno, and A.-L. Barabási, *Nucl. Instrum. Methods Phys. Res. B* 197 (2002) 185.
29. O. Bobes, K. Zhang, and H. Hofsäss, *Phys. Rev. B* 86 (2012) 235414.
30. S. Hazra, T.K. Chini, M.K. Sanyal, J. Grenzer, and U. Pietsch, *Phys. Rev. B* 70 (2004) 121307.
31. M. Nastasi, J.W. Mayer, and J.K. Hirvonen, *Ion-solid interactions: Fundamentals and applications*. 1996: Cambridge University Press.

CHAPTER 6

6 Statistical analysis of ripple morphology formed on Si surfaces

6.1 Introduction

Synthesis of patterned surfaces allows us to modify the material properties as well as the interaction of the surface with external excitations without changing the chemical composition of the surface. For instance, larger surface area become available with textured surfaces, which is suitable for solar cell application [1,2]. Specific type of nanostructured surfaces, such as pyramidally textured, nanoporous, grass-like surfaces etc., efficiently trap light and enhance the photovoltaic properties [3-6]. Wettability of surface is dependent upon surface morphology [7,8], periodic nanoscale dot and wire-like structures are promising for microelectronic application, surface reflectance can be effectively reduced by using submicron Si surface gratings with appropriate aspect ratio [9]. Moreover, the properties of thin films deposited on patterned surfaces are highly influenced by the surface textures. It is therefore, imperative to characterize and tune surface textures in order to effectively control materials properties.

Studies of morphological features of surfaces almost always considered the roughness aspect of surface textures, for example, in the context of tribology or in coatings, or in engineering applications [10]. However, recent studies revealed that other surface parameters, like correlation length [11], should also be considered towards assigning the applicability of surface properties for any technological application [12]. Moreover, it is also important to understand the temporal evolution of the parameters to realize the controllability of the surface processing technique. In such studies, three possible changes in parameters, which

characterize the surface, can be expected: parameters will (i) grow (highly rough surface), (ii) decay (smooth surface), and (iii) remain constant with time. These three possibilities have further significance in the context of applications. For instance, rough surfaces can be used for photovoltaic application etc. [13], smooth surfaces can be used for thin film transistors, reflectors etc. [14]. As described above, morphological parameter apart from roughness, such as roughness exponent and structural anisotropy are found to be important in understanding the evolution of surfaces [15,16] and, at the same time, provide more information on the morphology.

It has been shown both theoretically [17,18] and experimentally [19] that the textures generated by ion-beam on solid surfaces can be tuned by varying the experimental parameters. We have described the dependence of surface morphology on experimental parameters, in the medium energy regime, in Chapter 4. In this chapter, we examine the features of ripple-patterned Si surfaces generated by 60 keV Ar⁺-ions at different angles of incidence and ion fluences. We characterize the patterned surfaces in terms of areal ratio, ripple directionality, and aspect ratio, through the statistical parameters extracted from AFM images of the surfaces. The statistical parameters used for surface characterization have been determined by using the software package SPIP [20]. This image analysis software package offers the facility of extracting of quantitative information from the AFM images of irradiation surfaces, as described in the following. We also describe the correlation lengths and quality of ordering to address the anisotropy issue of the ripple patterned surfaces generated under ion irradiation.

6.2 Experimental Details

The morphological studies were carried out on Si samples irradiated by 60 keV Ar⁺-ions at $\theta = 0^\circ, 30^\circ, 45^\circ, 54^\circ, 60^\circ,$ and 75° , using an ion current density of $\sim 20 \mu\text{A}/\text{cm}^2$. As described in Chapter 4, AFM studies show that ripple patterns form from ion angle of incidence $\theta=45^\circ$

to $\theta=75^\circ$. Analysis of surface morphology was carried out as a function of ion angle of incidence in the angular range $45^\circ \leq \theta \leq 75^\circ$, for a fixed ion fluence of 2×10^{18} ions cm^{-2} . In addition, the ripple morphology has been studied as a function of irradiation time (fluence) at incident angle $\theta=60^\circ$.

6.3 Results

Fig. 6.1 shows a representative 3D AFM image (area $10 \times 10 \mu\text{m}^2$) of rippled-Si surface formed by 60 keV Ar^+ -ion irradiation at $\theta=60^\circ$ to fluence of 3×10^{18} ions cm^{-2} . The black arrow on the image shows the direction of projection of the obliquely incident ion-beam over the surface, which is designated as the x -direction, as shown.

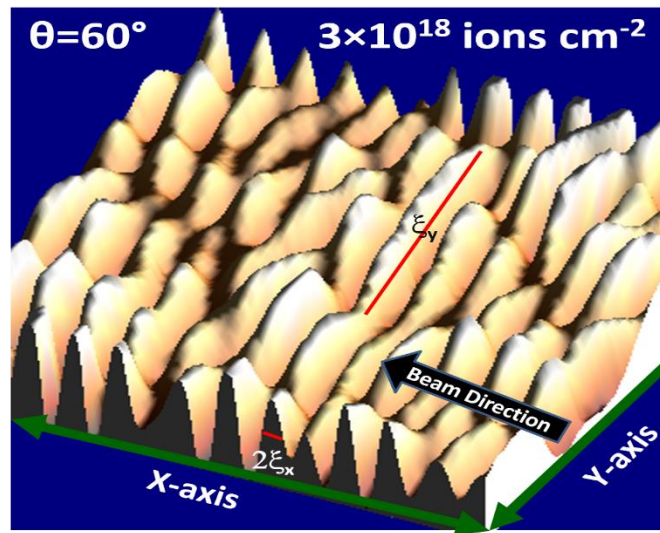


Figure 6.1: 3D image of ripple patterns on Si surface irradiated by 60 keV Ar^+ ions at $\theta=60^\circ$ to the fluence of 3×10^{18} ions cm^{-2} .

For quantitative understanding of the observed morphology, we determine the parameters Surface textured aspect ratio “ Str ”, Surface textured direction index “ $Stdi$ ”, and surface developed interfacial area ratio “ Sdr ”, which have been described in Chapter 3.

Str is the ratio of the lengths of two red straight lines shown in Fig. 6.1: half of the short straight line shown within the crosssection of one ripple pattern (which is a measure of the width of the ripple), $2\zeta_x$, and the long straight line drawn over one ripple, of length, ζ_y . These

ξ_x and ξ_y are defined as the slow and fast varying modes of the ripple structure. Length of both the straight lines are extended in their respective directions over the image where the surface height falls to $1/e$ of the maximum value. Thus, these two lines can also be understood as the lateral correlation lengths of the rippled surface in x and y -directions, respectively, where ripple patterns are aligned in the y -direction. It can be mentioned here that ripple patterns formed on the irradiated surfaces in our present experiment were seen to be perpendicular to the ion-beam direction (parallel to y -axis).

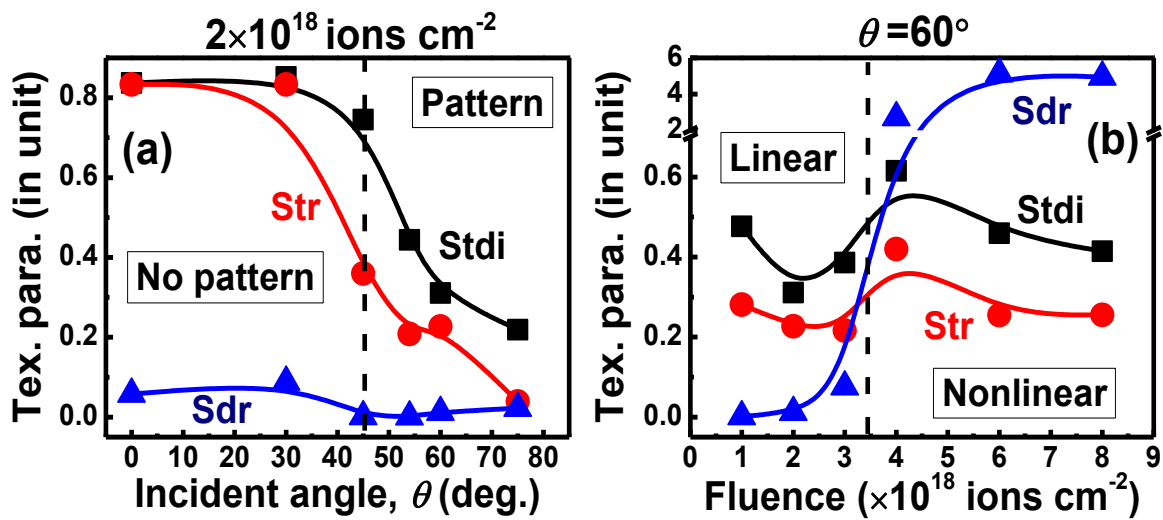


Figure 6.2: Different texture parameters extracted from irradiated Si surface and plotted as a function of (a) angle of incidence, θ at a fixed fluence of 2×10^{18} ions cm^{-2} , (b) ion fluence, at fixed incidence angle $\theta = 60^\circ$.

The parameters “*Str*” and “*Stdi*” stay more or less constants in the angular regime $\theta < 45^\circ$ as shown in Fig. 6.2(a). The angular range $0^\circ - 45^\circ$ is defined as ‘no pattern’ regime [left side of dotted black line in Fig 6.2 (a)] as the surface remains smooth under ion irradiation in this regime. The ‘no pattern’ regime is followed by a decreasing trend in “*Str*” and “*Stdi*” for $\theta \geq 45^\circ$, which is called the ‘Pattern’ regime [right side of dotted black line in Fig 6.2 (a)] as evolution of ripple patterns is observed here. Higher values of *Str* (~ 0.8) and *Stdi* (~ 0.8) in the regime of $\theta < 45^\circ$, compared to the regime of $\theta \geq 45^\circ$ reveal the uniformity in surface texture and isotropy of the surface in the ‘no pattern’ regime. On the other hand, the decreasing trend in “*Str*” and “*Stdi*” with θ in the “pattern” regime suggests deviation from the isotropy due to

extension of the structures (ripples) in one preferred direction. The magnitude of the parameter “*Sdr*”, which measures the % increment in the surface area, is found to be higher in “No pattern” regime compared to the “Pattern” regime. This is associated with the roughness of the surface developed under irradiation. In fact, observed difference in *Sdr* value in two regimes suggests that the ripple patterned surfaces are smooth compared to the rough surfaces in the “No pattern” regime. Therefore, increasing roughness (as have been shown in Chapter 4) as a function of θ in the “Pattern” regime seems to be due to the dominating nature of the textured structure.

It has been shown in Chapter 4 that the evolution of ripple patterns with ion fluence (irradiation time) can be divided into linear and nonlinear regimes. For 60 keV Ar⁺-ion irradiation of Si at 60°, the linear regime is extended from the fluence 1×10^{18} ions cm⁻² to 3×10^{18} ions cm⁻², and the nonlinear regime is realized from the 4×10^{18} ions cm⁻² to the highest fluence in our study, namely 8×10^{18} ions cm⁻². These two regimes are shown in Fig. 6.2(b), where we present the variation in *Str*, *Stdi*, and *Sdr* with ion fluence. The variation in *Str* and *Stdi* with ion fluence appears similar to each other. In the linear regime, both the parameters initially decrease with fluence followed by an increment, and decreases again in the nonlinear regime. In contrast, the parameter *Sdr* shows an increasing trend in both linear and nonlinear regimes. It is also observed from 6.2(b) that the values of *Str* and *Stdi* are lowest at fluences of 2×10^{18} and 3×10^{18} ions cm⁻², respectively. Therefore, the ion-irradiated surfaces observed at these two fluences can be described as most dominant (due to the lowest *Str*) and directional (due to the lowest *Stdi*) textured surfaces in the linear regime. Similarly, the surface corresponding to the fluence of 8×10^{18} ions cm⁻² is the most dominant and directional surface (within our experimental range) of the non-linear regime. At this highest fluence of 8×10^{18} ions cm⁻², the value of *Sdr* is 35 times higher than that of the lowest fluence. Thus, it can be said that the surface developed at the fluence of 8×10^{18} ions cm⁻² has

the highest interfacial surface area and most dominant ripple pattern. On the other hand, most directional surface texture develops at the fluence of 2×10^{18} ions cm^{-2} (as mentioned above).

In Figs. 6.3 (a) and (b), we demonstrate the evolution of lateral correlation lengths ξ_x , ξ_y [shown in Fig. 6.1], the system correlation length in the x -direction, ζ_x , and ζ_x/λ ratio, as functions of ion angle of incidence and ion fluence, respectively (λ is ripple wavelength).

These parameters were extracted from the auto-correlation functions of AFM images of patterned Si surfaces at respective angles of incidence and ion fluences. Here x -direction is the direction of projection of ion-beam onto the surface (i.e. perpendicular to the ripples) and y -direction is perpendicular to it (i.e. along the ripples), as shown in Fig. 6.1. It is observed from Fig. 6.3(a) that ξ_x slowly decreases with increasing θ , while ξ_y increases sharply. Such variations in correlation lengths clearly indicate that ripple width decreases while length of ripples increases with increasing angle of incidence. Significantly, the system correlation length (ζ_x) which contains the information about length of ripple patterns, i.e., spatial ordering of patterns, is found to be nearly constant in Fig. 6.3(a). However, the increment in the ζ_x/λ ratio with angle of incidence demonstrates improvement in ordering of ripple patterns.

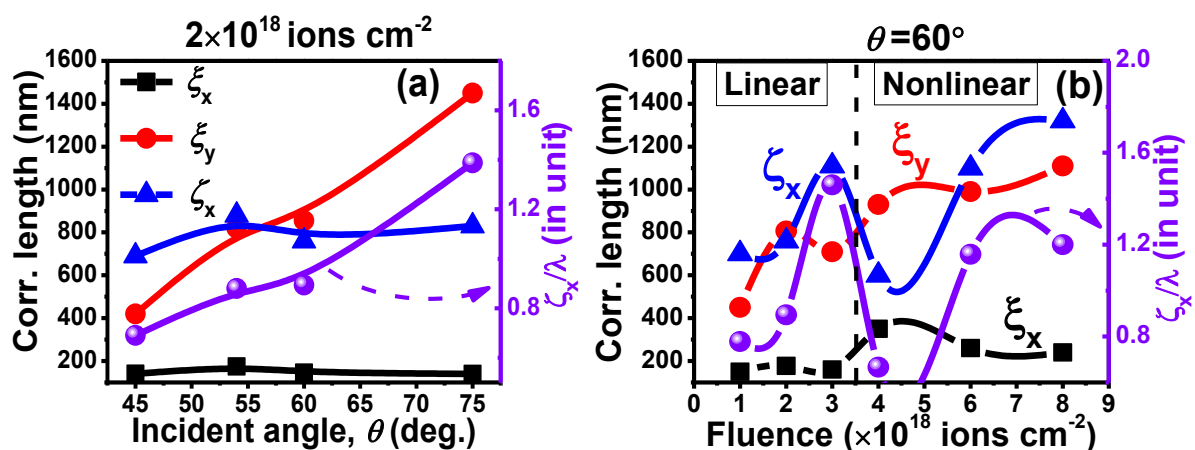


Figure 6.3: Lateral correlation lengths in x and y -direction, $\xi_{x,y}$, system correlation length in the x -direction, ζ_x , ratio of ζ_x to ripple wavelength λ as a function of (a) incidence angle, θ at a fixed fluence of 2×10^{18} ions cm^{-2} , (b) ion fluence at a fixed incidence angle $\theta=60^\circ$. The dotted black line distinguishes linear and nonlinear regimes.

On the other hand, ζ_x stays more or less constant with respect to ion fluence in the linear regime, whereas ζ_y shows an increasing trend, as is seen from fig. 6.3(b). As the system goes from linear to the nonlinear regime, ζ_x shows an increment, followed by a decreasing trend, while ζ_y still increases. Further, the system correlation length, ζ_x , and ζ_x/λ ratio (ordering parameter of pattern) shows the similar trend. Both the parameters increase with increasing ion fluence in the linear regime whereas a sharp decrease in their values is observed with further increase in the fluence from 3×10^{18} to 4×10^{18} ions cm^{-2} , i.e., with the transition from linear to nonlinear regime. Further increasing the fluence, ζ_x continues to increase while ζ_x/λ becomes constant for fluences $> 6 \times 10^{18}$ ions cm^{-2} . Datta *et al.* [21] reported a decrease in ζ_x/λ ratio in the nonlinear regime (starting from fluence 8×10^{17} ions cm^{-2}). This regime was identified based on the shadowing condition in their experiment for 60 keV Ar^+ in Si at a fixed ion current density of $175 \mu\text{A}/\text{cm}^2$ [22]. However, we have shown in Chapter 4 that shadowing is absent in the fluence range considered in our experiment. Comparing our results with that of Datta *et al.*, one can infer that influence of shadowing may lead to reduction in the ordering of ripple patterns, as expresses by (ζ_x/λ) ratio.

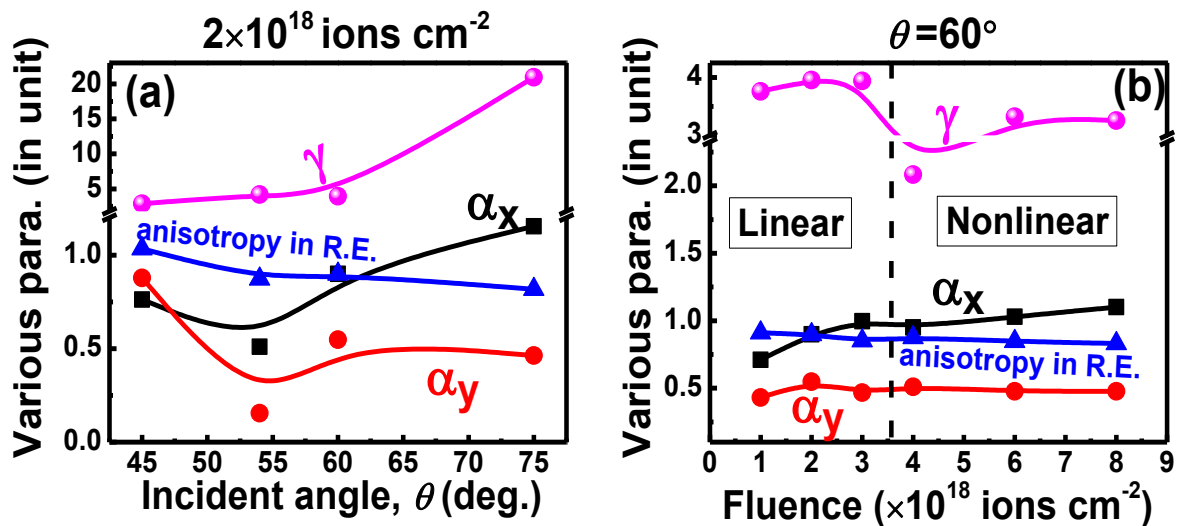


Figure 6.4: 1-dimensional roughness exponent (α_x , α_y where, x - and y -directions are parallel and perpendicular to the direction of incident ion-beam, respectively), anisotropy in roughness exponent (R.E.) and scaling anisotropy, γ are plotted as functions of (a) incident angle, θ , at a fixed fluence and (b) ion fluence at a fixed incident angle of 60° while the dashed vertical line was drawn to distinguish the linear and nonlinear regimes.

The roughness exponents α_x and α_y of ion-irradiated Si surfaces, along x - and y -directions are presented in Fig. 6.4, as a function of ion angle of incidence and fluence. These parameters have been extracted from the one-dimensional power spectral density (1D-PSD, not shown here) of the AFM images calculated along the respective directions. These exponents can also be obtained from height-height correlation functions [22]. However, Vivo *et al.* [16] showed that the value of α_x and α_y extracted from PSD in Fourier space [as done here] is more reliable than those extracted from the height-height correlation functions in the real space. The difference in their values is found to increase with θ , as can be seen from the figure. The observed surface can be associated with an universality class depending upon the values of α_x and α_y [23]. Since the roughness exponent α_y in the direction of ripple length is seen to remain < 1 throughout the range of angles of incidence, the irradiated surface in this case may be associated with Family-Vicsek or intrinsic universality class. On the other hand, α_x undergoes a transition from < 1 to > 1 in the range $60^\circ < \theta < 75^\circ$, which indicates a transition to super-rough or new class of universality from Family-Vicsek or intrinsic class [23]. This classification further helps to assign the theoretical model by which the ion induced pattern formation on Si surfaces can be understood.

With the help of these values of α_x and α_y , we have calculated the scaling anisotropy, γ , defined as [24]:

$$\gamma = \frac{\xi_y}{\xi_x} \left(\frac{2^{\frac{2}{2^{1+2\alpha_x}-1}}}{2^{\frac{2}{2^{1+2\alpha_y}-1}}} \right)^{1/2}, \quad (6.1)$$

where $\left(\frac{2^{\frac{2}{2^{1+2\alpha_x}-1}}}{2^{\frac{2}{2^{1+2\alpha_y}-1}}} \right)^{1/2}$ = anisotropy in the roughness exponent (R.E.) and $\frac{\xi_y}{\xi_x}$ = correlation length anisotropy. Here, the value of $\frac{\xi_y}{\xi_x}$ is obtained from the corresponding *Str* values [shown in Fig. 6.2]. In Fig. 6.4(a), scaling anisotropy γ is found to increase with angle of incidence

which indicates an increase in the anisotropy with formation of ripples at higher angles of incidence. The increment in γ may be linked with the correlation length anisotropy.

From Fig 6.4(b), it follows that α_y remains < 1 for the entire fluence range and hence, belongs to the Family-Vicsek or intrinsic universality class. The value of α_x changes from < 1 to > 1 with transition to the nonlinear regime, which indicates a transition from Family-Vicsek or intrinsic class to super-rough or new class of universality. Values of α_x observed in our case are close to the value reported by Datta *et al.* [22]. To follow the scaling anisotropy under increasing ion fluence, we followed the same method as for the case of variation in angle of incidence. In Fig. 6.4(b), the scaling anisotropy, γ , is found to increase slowly with fluence in the linear regime and then it undergoes a reduction in magnitude due to linear to nonlinear transition, and increases again in the nonlinear regime. The increasing nature of γ may be related to the correlation length anisotropy, similar to the case of variation in angle of incidence. However, the value of γ at higher fluences in both the regimes is found to be lower than that observed in case of $\theta=75^\circ$ for the fluence of 2×10^{18} ions cm^{-2} . Based on this observation, we can infer that surface anisotropy increases faster due to a variation in the angle of incidence compared to that of ion fluence.

6.4 Summary

We have analyzed medium energy ion-irradiated patterned surfaces in detail in terms of statistical parameters which characterize the quality of surface textures. These parameters clearly show the different stages of surface texturing as the surface evolves under ion irradiation at different angles of incidence and ion fluences. Texture parameters show that most directional and dominant surface patterns are developed at angle of incidence $\theta=75^\circ$, whereas interfacial area increases towards higher fluences of 8×10^{18} ions cm^{-2} at $\theta=60^\circ$. At the same time, ordering of ripple patterns was observed to be maximum at $\theta=75^\circ$. On the other hand from our fluence-dependent study at $\theta=60^\circ$, ordering of ripple is found to be the

highest near the end of the linear regime (i.e. fluence: 3×10^{18} ions cm^{-2}). We have also showed that the anisotropy of these ordered ripple patterned surfaces increases as a function of ion angle of incidence and irradiation time (fluence). Moreover, depending on the value of directional roughness exponent, ripple patterned surfaces can be associated with one of the universality classes of scaling. The observed surface features in our experiments may be utilized for suitable applications which need specific texture-dependent functionalities.

Bibliography

1. T. Makris, K. Tsevas, L. Kadylis, L. Mprechas, and E. Skuras, *J. Sol. Energy* 135 (2013) 034503.
2. Y. Inomata, K. Fukui, and K. Shirasawa, *Sol. Energy Mat. Sol. C.* 48 (1997) 237.
3. P. Campbell and M.A. Green, *J. Appl. Phys.* 62 (1987) 243.
4. K. Bum Sung, L. Don Hee, K. Sun Hee, A. Guk-Hwan, L. Kun-Jae, V.M. Nosang, and C. Yong-Ho, *J. Am. Ceram. Soc.* 92 (2009) 2415.
5. J.S. Yoo, I.O. Parm, U. Gangopadhyay, K. Kim, S.K. Dhungel, D. Mangalaraj, and J. Yi, *Sol. Energy Mat. Sol. C.* 90 (2006) 3085.
6. J. Zhao, A. Wang, M.A. Green, and F. Ferrazza, *Appl. Phys. Lett.* 73 (1998) 1991.
7. J. Bico, U. Thiele, and D. Quéré, *Colloid Surface A* 206 (2002) 41.
8. J.B. Taylor, A.L. Carrano, and S.G. Kandlikar, *Int. J. Therm. Sci.* 45 (2006) 962.
9. H. Sai, Y. Kanamori, K. Arafune, Y. Ohshita, and M. Yamaguchi, *Prog. Photovoltaics* 15 (2007) 415.
10. Y. Zhang and S. Sundararajan, *Langmuir* 23 (2007) 8347.
11. Y. Zhang and S. Sundararajan, *J. Appl. Phys.* 97 (2005) 103526.
12. V. Safonov, A. Zykova, J. Smolik, R. Rogovska, N. Donkov, and V. Georgieva. *The surface parameters modifications at nano scale for biomedical applications.* in *J. Phys.: Conf. Ser.* 2010. IOP Publishing.
13. H. Takagi, R. Maeda, T.R. Chung, N. Hosoda, and T. Suga, *Jpn. J. Appl. Phys.* 37 (1998) 4197.
14. F. Frost, R. Fechner, B. Ziberi, J. Völlner, D. Flamm, and A. Schindler, *J. Phys.: Condens. Matter* 21 (2009) 224026.
15. E. Vivo, M. Nicoli, and R. Cuerno, *Phys. Rev. E* 86 (2012) 051611.

16. E. Vivo, M. Nicoli, M. Engler, T. Michely, L. Vázquez, and R. Cuerno, *Phys. Rev. B* 86 (2012) 245427.
17. S. Vogel and S.J. Linz, *EPL (Europhysics Letters)* 76 (2006) 884.
18. E.O. Yewande, R. Kree, and A.K. Hartmann, *Phys. Rev. B* 73 (2006) 115434.
19. B. Ziberi, F. Frost, M. Tartz, H. Neumann, and B. Rauschenbach, *Appl. Phys. Lett.* 92 (2008) 063102.
20. A.S. Image Metrology. *SPIP Software*. Available from: www.imagemet.com.
21. D.P. Datta, *Modification of Silicon Surface under medium energy heavy ion bombardment*. 2008, Saha Institute of Nuclear Physics: Kolkata.
22. D.P. Datta and T.K. Chini, *Phys. Rev. B* 69 (2004) 235313.
23. J.J. Ramasco, J.M. López, and M.A. Rodríguez, *Phys. Rev. Lett.* 84 (2000) 2199.
24. Y. Zhao, G.-C. Wang, T.-M. Lu, M. De Graef, and T. Lucatorto, *Characterization of Amorphous and Crystalline Rough Surface-Principles and Applications*. Vol. 37. 2000: Access Online via Elsevier.

CHAPTER 7

7 Wettability of 60 keV Ar-ion irradiated rippled-Si surfaces

7.1 Introduction

In Chapters 4, 5, and 6, we have presented our experimental studies on ion-beam induced modification of Si surfaces. These textured surfaces have started drawing attention because they show promising applications in electronic, optoelectronic, magnetic or biochemical devices as well as in solar cells [1-5]. It is, however, necessary to investigate specific physiochemical properties of such patterned surfaces in order to functionalize them for specific potential applications. For instance, it is important to explore the wettability of ion-patterned surfaces because engineering the behavior of liquid on solid surface has wide applications ranging from the design of water-repelling surfaces [6] to fluid flow manipulation in lab-on-chip devices (i.e. micro-fluidic devices [7] and microelectronics [8]) and better surfaces to inhibit corrosion and prevent fouling (self-cleaning surfaces [9]).

Wettability of surfaces is being investigated for decades in terms of contact angle [10]. It was thought to be a function of surface energy [9] and dependent upon the chemical composition of the surface and the liquid. Wenzel [11] introduced a connection of the contact angle with the roughness of the surface. Recent theoretical studies [12] still probe the effect of surface roughness on the change in wettability behavior. Apart from the roughness, [13] other surface topological parameter (like pattern wavelength) is also found to govern the wettability of textured surfaces [14]. In fact, effect of anisotropic ripple-like morphology on wettability of the surface has already been investigated theoretically [8]. Thus, it becomes important to investigate the wettability issues of ion-induced rippled surfaces for possible applications.

Wettability study on ion induced patterned surfaces exist (in very few reports to the best of our knowledge) at two different levels of incident ion energy (say 200 keV and 500 eV) [13,15].

In this chapter, we describe our studies on wettability of patterned Si surface developed by medium energy Ar⁺-ion bombardment. A sessile drop method is used to measure the contact angle of water droplets on the ion sputtered surfaces. Change in the contact angle with ion fluence is understood in terms of its physicochemical and topological parameters.

7.2 Experimental

The wettability studies were carried out on 60 keV Ar⁺-ion bombarded Si(100) surfaces. Ion bombardment was carried out at two angles of incidence, viz. $\theta=0^\circ$ and 60° and for different ion fluences. The details of the irradiation experiments is described in Chapter 4. The surface topography of the bombarded Si was studied by AFM. The measurement of contact angles of water drops on the bombarded surfaces were done by sessile drop method using a setup from Dataphysics (Model: OCA15EC) having an accuracy of 0.1° . This instrument uses a computer-controlled syringe to dispose 0.5 μL deionized Milli-Q water droplet on a Si surface. All the contact angles were measured on a number of different places to check the uniformity of measurements. During measurements, the ambient temperature and relative humidity were maintained in the range 23-25°C and 42-47%, respectively.

7.3 Results and discussion

Fig. 7.1 shows the contact angles measured for the pristine as well as Ar⁺-ion irradiated Si samples for different fluence values. In all images of Fig. 7.1, a small drop of liquid with a spherical cap shape is resting on a horizontal solid surface. The contact angles of liquid-to-solid surface (extracted by the control software) are written at the top left corner of each image. In our subsequent calculations we have taken the average of the contact angles

measured for the left and right sides of the water drops. However, difference in the contact angles measured from both sides of the water droplet in each case is nominal.

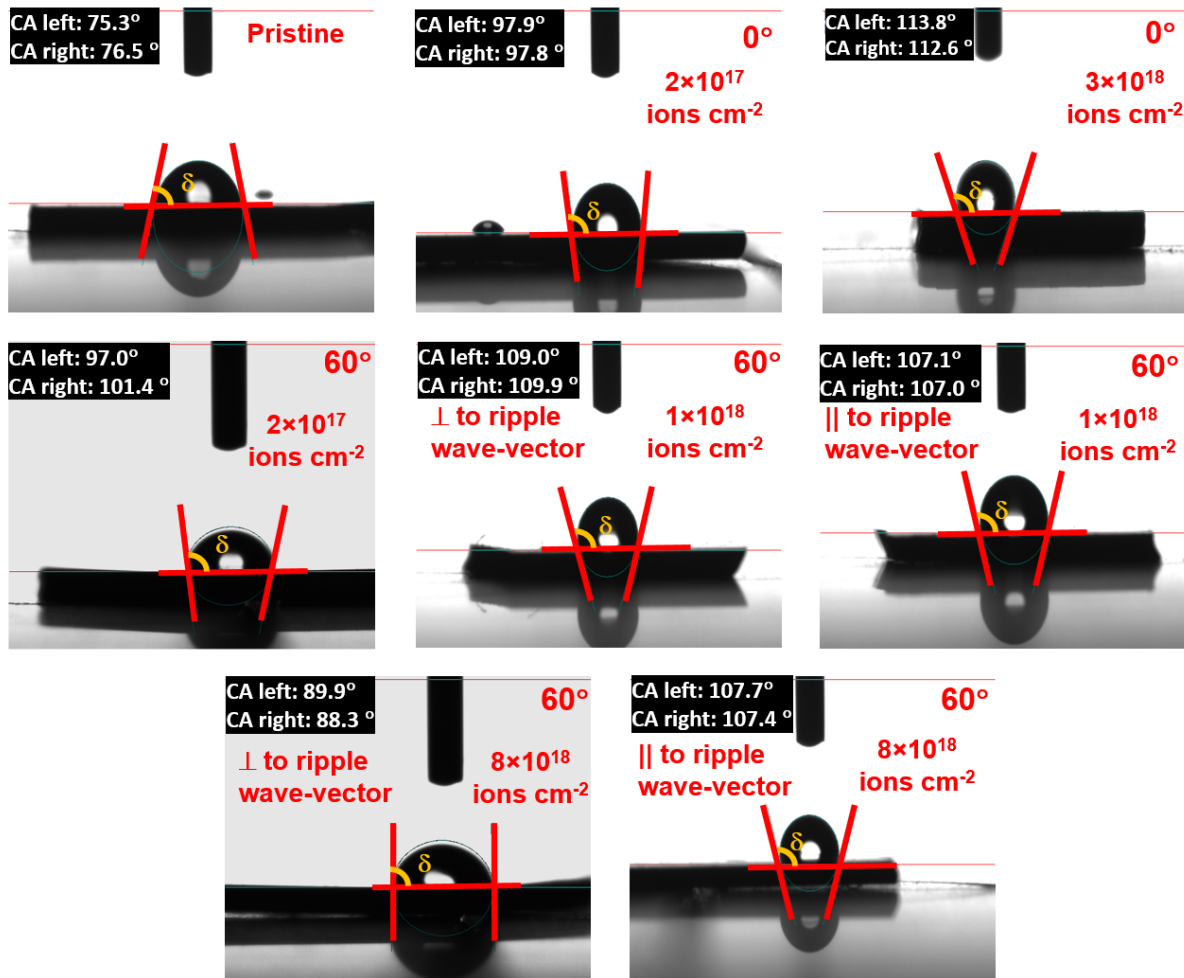


Figure 7.1: A typical sessile drop with the spherical cap on the pristine and 60 keV Ar^+ -ion irradiated Si surfaces at incident angles $\theta=0^\circ$ and 60° . Contact angles (δ) were measured for pristine and irradiated surfaces as a function of ion fluence. For ripple patterned surfaces, δ values were measured in two directions: (1) parallel and (2) perpendicular to the ripple wave-vector.

(a) Angle of incidence, $\theta=0^\circ$

The contact angles (δ) measured on Si irradiated at 0° are shown in Fig. 7.2. Our AFM studies reveal that rough surfaces develop under ion irradiation at this angle of incidence. The contact angle, δ , of pristine Si surface is found to be 75.8° ($< 90^\circ$), which shows the hydrophilic nature of the surface which is typically the case for pristine Si surface [16,17]. The contact angle, however, becomes $>90^\circ$ for irradiated Si, showing a transition of the irradiated surface to a hydrophobic one. In the fluence range of our experiment, δ increases

with increasing ion fluence, reaching a maximum of 113.2° at the highest fluence of 3×10^{18} ions cm^{-2} . We first attempt to understand the observed behavior in terms of physical changes of the surface.

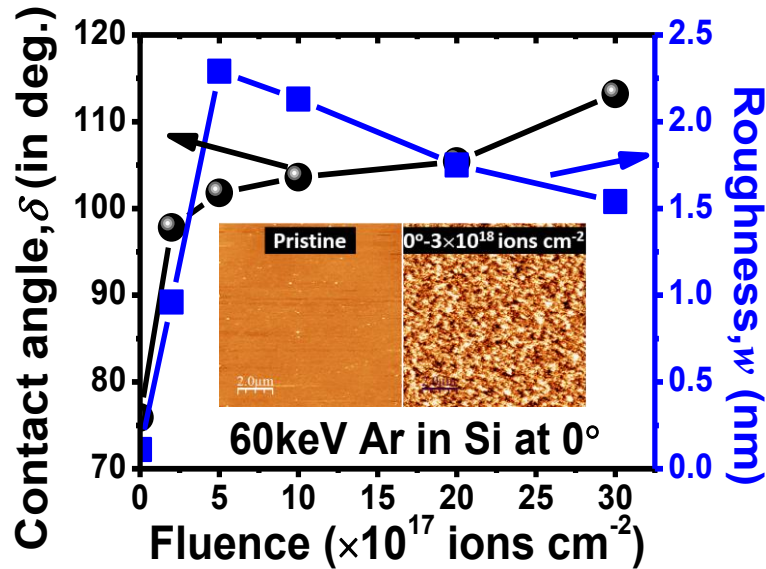


Figure 7.2: Variation in δ and w versus ion fluence for 60 keV Ar^+ -ion irradiation of Si surface at $\theta=0^\circ$. The inset show AFM images of pristine and normally implanted Si (to the fluence of 3×10^{18} ions cm^{-2}) samples.

The contact angle between a liquid and a solid surface depends on the interface tensions at three different interfaces, namely, solid-liquid, solid-air, and liquid-air interfaces. Thus, a contact angle measurement is found to be a tool to determine the interfacial surface tension of a solid surface which is numerically equal to the characteristic interfacial free energy. In other words, contact angle depends on the interfacial surface energy [18]. Wenzel [11] introduced the contribution of surface roughness in contact angle of a liquid drop put on the solid surface as:

$$\cos \delta_r = r \cos \delta_f, \quad (7.1)$$

where r is known as the roughness factor and is defined as the ratio of total and projected rough areas. δ_r and δ_f are contact angles of liquid droplet on rough surface and flat surface, respectively. Thus, Eq. 7.1 implies that for increasing r if $\delta_f \geq 90^\circ$ then the contact angle for rough surface (δ_r) increases, whereas the contact angle for rough surface (δ_r) decreases if δ_f

$\leq 90^\circ$. In other words, a hydrophilic surface becomes more hydrophilic and a hydrophobic surface becomes more hydrophobic with increase in r . In this way, Wenzel's law does support the transition from a hydrophilic to the hydrophobic surface due to an increase in the surface roughness.

In the present case, at least one order of larger roughness value of irradiated Si, compared to pristine Si, would not help us to understand the observed transition at 0° . Raman study (not presented here) of irradiated Si revealed the formation of a top amorphous layer for the entire fluence range shown in Fig. 7.2. In addition, RBS studies (not shown here) carried out on the irradiated samples showed the presence of Ar atoms in the near-surface regions. Based on these findings, we can infer that chemical composition of the top layer of irradiated Si is modified. In this study, we used p -Si(100) wafers for which the surface free energy is known to be 2512 mJ m^{-2} [19], while surface free energy for amorphous Si is known to be 1050 mJ m^{-2} [20]. The ion fluence used in the present experiment is much higher than the critical fluence ($\sim 5 \times 10^{15} \text{ ions cm}^{-2}$) for amorphization of Si [21] and thus, the surface free energy is due to reduce by more than half after amorphization. It is worth to mention here that with reduction in the surface free energy, hydrophobicity of surface is expected to increase and in turn δ should increase accordingly [18]. Therefore, transition from the hydrophilic pristine Si to hydrophobic irradiated Si (for the fluence of $2 \times 10^{17} \text{ ions cm}^{-2}$) may be an outcome of this reduction in the surface free energy. However, for the fluence of $2 \times 10^{17} \text{ ions cm}^{-2}$, where irradiated surface becomes hydrophobic, further increment in roughness is expected to result an increase in δ according to Wenzel's law [11]. In contrast, the roughness of irradiated Si at $\theta=0^\circ$ remains of the same order. Therefore, variation in roughness alone may not be enough to explain the increase in δ with fluence. Alternatively, it may be noted that the presence of Ar atoms, present in the near-surface region as observed from EDS and RBS studies, may also contribute to reduce the available surface free energy due to their inert nature. Therefore,

further increase in δ at higher fluences of Ar, can be attributed to be an outcome of the presence of Ar atoms near the top of the amorphous Si layer.

(b) Angle of incidence, $\theta=60^\circ$

For irradiation at $\theta=60^\circ$, the contact angle, δ , is found to increase from $\delta=99^\circ$ for the fluence of 2×10^{17} ions cm^{-2} to $\delta=117.1^\circ$ for the fluence of 5×10^{17} ions cm^{-2} . So far this analysis has been done for the surface which is rough in nature like the case of 0° as described above. It has been shown in Chapter 4 that ripple patterns start to appear from the fluence of 1×10^{18} ions cm^{-2} and gets prominent towards higher fluences, which leads to higher surface anisotropy as well (described in Chapter 6). Theoretical models [10,22] and experiment [23] show that the wettability, specifically for rippled patterned surfaces, depends on the morphological parameters other than r [in Eq. 7.1]. For instance, Chung *et al.* [23] have shown that anisotropic surface (viz. the ripple patterns) introduces the anisotropy in contact angles. To understand it better, we show a schematic diagram in Fig. 7.3. Fig. 7.3(a) is a top-view of system which has a water drop on an isotropic surface. Fig. 7.3(b) represents the 3D side-view of a system having water drop on a rippled patterned surface. Here the patterned surface is the 3D AFM image corresponding to the fluence of 3×10^{18} ions cm^{-2} generated at $\theta=60^\circ$. It is clear from Fig. 7.3(a) that contact interface of water droplet with a solid surface finds the same morphology at all places around its (liquid to solid interface) boundary whereas the same contact interface of a water droplet with a rippled surface [in Fig. 7.3(b)] finds different morphology at the place of its (liquid to solid interface) boundary. For instance, liquid-to-solid interface at the points shown by the red line '1' in Fig. 7.3(b), will exist either on the groove between the two ripples or on a particular ripple. On the other hand, liquid-to-solid interface of the same water droplet at the points shown by the red line '2' in Fig. 7.3(b), will exist on the several ripples, where this interface will have the same height amplitude and periodicity as the surface patterns. Therefore, one can measure the contact

angle for ripple patterned surface at two different orientations: (i) parallel [along the points existing at the set of red line ‘2’ in Fig. 7.3(b)] and (ii) perpendicular [along the points existing at the set of red line ‘1’ in Fig. 7.3(b)] to the direction of the ripple wave-vector.

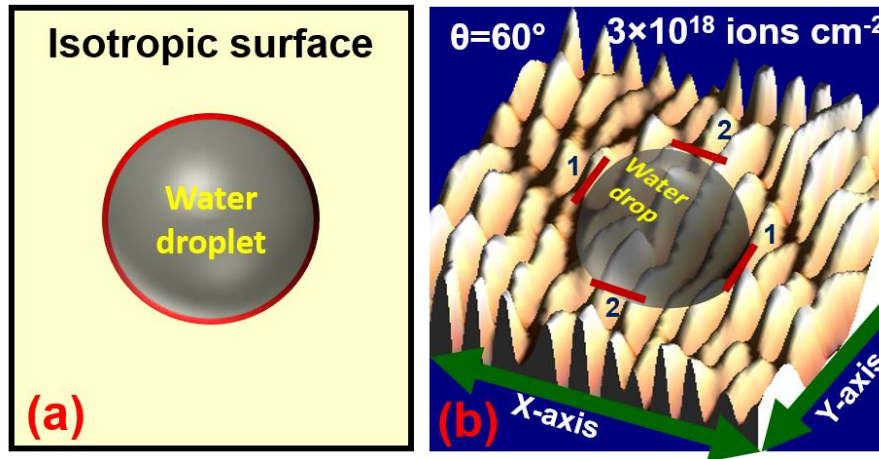


Figure 7.3: Schematic diagram of water droplet on (a) an isotropic surface (2D top view) and (b) an anisotropic (rippled) surface generated at $\theta=60^\circ$ for fluence $3 \times 10^{18} \text{ ions cm}^{-2}$ (3D side view). Set of red lines ‘1’ and ‘2’ show the different contact positions (orthogonal to each other) of the water droplet with the surface.

We have measured δ in both these directions and the results are shown in Fig. 7.4. In the perpendicular direction [along the red line ‘1’ in Fig. 7.3(b)], contact angles are found to decrease with fluence from the highest value of $\delta=109.5^\circ$ (corresponding to the fluence of $1 \times 10^{18} \text{ ions cm}^{-2}$) to $\sim 89^\circ$ (correspond to fluence $8 \times 10^{18} \text{ ions cm}^{-2}$) (shown in Fig. 7.2). In contrast, along the parallel direction [along the red line ‘2’ in Fig. 7.3(b)], δ values were found to remain constant with fluence. Thus, contact angle measurements reveal the decreasing nature of hydrophobicity with temporal evolution of ripple morphology in one direction whereas it remains constant along the other direction. This decreasing nature of hydrophobicity with fluence is similar to the one seen by Kumar *et al.* [13], who reported increasing hydrophilicity with irradiation time for ripple morphology on Si generated by using 200 keV Ar^+ -ion irradiation.

For $\theta=60^\circ$, the observed transition from the hydrophilic nature of the pristine surface to the hydrophobic nature of irradiated surfaces can be assigned to a reduction in the surface energy

for amorphous Si, similar to the case of 0° (as discussed above). Existence of this amorphous layer in irradiated Si was confirmed by micro-Raman, RBS, and TEM analyses [as discussed in Chapter 5 (data for 2×10^{17} ions cm^{-2} was not shown there)]. Further increase in δ value (in case of 5×10^{17} ions cm^{-2}) could be due to the increasing roughness in accordance with Wenzel's law. However, prominent change in δ cannot be explained by the observed nominal change in roughness (w) value. Thus, further increase in δ seems to be due to the presence of Ar atoms in the near-surface region of irradiated samples like the one for normally incident ions. The presence of Ar atoms is clearly realized from RBS analysis (discussed in Chapter 5). In fact, the presence of Ar atoms at higher fluences was shown in TEM images as well (depicted in Chapter 5). The decrease in δ in the perpendicular direction of the ripple wave-vector or constant value of δ in the direction parallel to the ripple wave-vector are in contrast to our findings corresponding to $\theta = 0^\circ$, where it increases for the same fluence range. It is thus, clear that ripple morphology is able to make significant changes in δ .

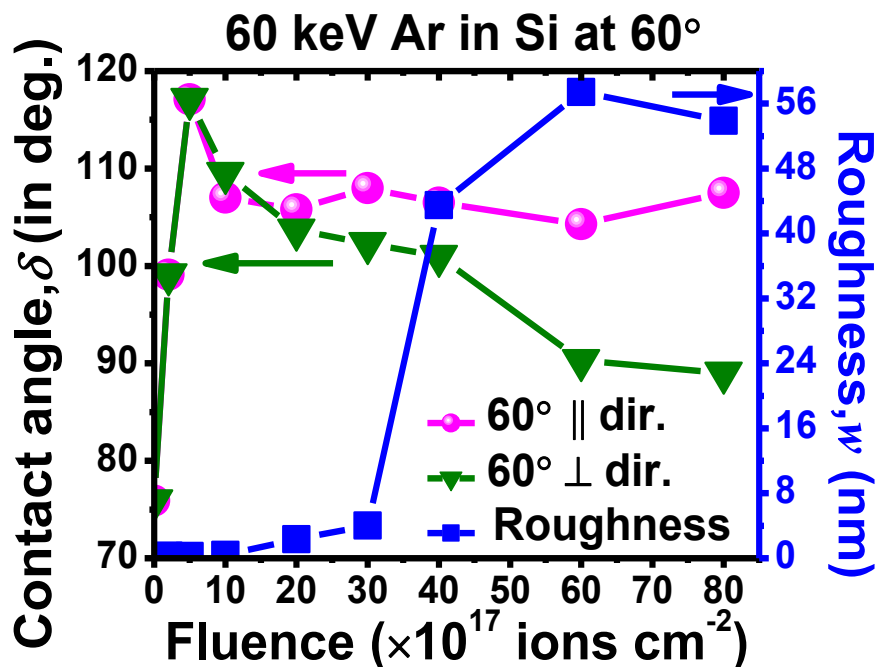


Figure 7.4: Variations in the measured δ and w values as a function of ion fluence for 60 keV Ar-ion irradiated Si at an incident angle of 60° . For ripple patterned surface, δ were plotted for two directions [as described in Fig. 7.3]: (i) parallel and (ii) perpendicular to the direction of the ripple wave-vector.

A decreasing trend in δ in the direction perpendicular to the ripple wave-vector contradicts Wenzel's law, which predicts an enhancement δ with increasing roughness (with fluence). Thus, to understand this decreasing behavior in δ with fluence, we consider two possibilities:

(1) For ripple patterned surface, Chung *et al.* [23] showed that the variation in contact angle with increasing roughness follows Wenzel's law when measured along the parallel direction of the ripple wave-vector, whereas it follows the opposite trend when measured along the perpendicular direction (due to the presence of a height barrier). In the present case, the observed decreasing trend in contact angle, with increasing fluence and roughness, could be due to pinning the droplet boundary in the presence of height barrier at that place.

(2) Presence of Ar atoms in the near-surface region of the amorphous layer can lead to change in δ as found in case of 0° and rough surfaces at 60° . XTEM (Fig. 7.5) analysis reveals that the front slope of ripples which face the beam directly is densely populated with Ar atoms whereas amount of Ar atoms is negligible in the rear slope of ripples. This is well corroborated by the EDS analysis described in Chapter 5. Thus, in case of 60 keV Ar-ion induced ripple patterned surface, the presence of Ar atoms in the near-surface region of the top amorphous layer is found to be inhomogeneous unlike the case of 0° where no pattern formation takes place.

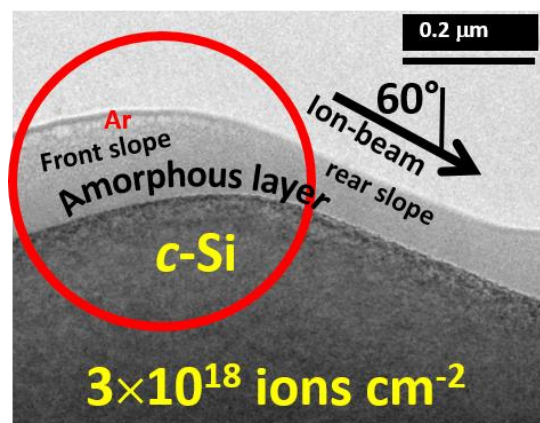


Figure 7.5: XTEM image of ion-induced ripple pattern on Si surface, formed at an incident angle of 60° and fluence of 3×10^{18} ions cm^{-2} . Front slope of ripple has been encircled whereas white patches in the near-surface region of the amorphous layer indicate Ar-bubbles.

Due to this inhomogeneous composition of ripple patterned surface, surface area containing the Ar atoms becomes smaller compared to the rough surface. It has been mentioned above that the presence of Ar atoms, close to the surface of the top amorphous layer, leads to a decrease in the surface energy and leads to an increase in δ . In case of inhomogeneous surface composition, this reduction in surface free energy would be affected as the surface area which contains Ar atoms gets reduced. In this manner, surface energy would be high for an inhomogeneous Ar distribution. Now, for the same volume of a liquid drop, more surface area would be required to reach the equilibrium condition compared to the surface area having a homogeneous distribution of Ar atoms [18]. As a result, for heterogeneous distribution of Ar atoms, δ will decrease to compensate for the higher surface energy. The lowering in δ values (109.5° and 107°) in both directions at the onset fluence of ripple pattern formation, i.e. 1×10^{18} ions cm^{-2} compared to that at the fluence of 5×10^{17} ions cm^{-2} (117°), confirms the influence of inhomogeneous Ar distribution. The inhomogeneous Ar atom distribution is expected to increase with increasing ripple height and hence with increasing ion fluence, since ripple height (and corresponding roughness) increases with ion fluence [Fig. 7.4]. Therefore, this increasing inhomogeneity with fluence, is found to have a definite effect on decreasing δ (in a direction perpendicular to the ripple wave-vector) towards higher fluences.

If inhomogeneity in Ar atom distribution over the irradiated surface would have been the only reason for decreasing δ in the perpendicular direction (of the ripple wave-vector), then δ should also decrease along the parallel direction (of the ripple wave-vector) as well. However, it remains constant with fluence. Therefore, at this stage, we expect that both the possible mechanisms: (i) of pinning the drop boundary described by Chung *et al.* [23] and (ii) inhomogeneous distribution of Ar atoms in the near-surface region of the top amorphous layer are operative in determining the contact angle δ on ripple patterned Si surfaces.

7.4 Conclusion

Contact angle measurements reveal the transition of Si surfaces from hydrophilic to hydrophobic nature due to ion irradiation at $\theta=0^\circ$ and 60° . This transition in the wetting nature of Si surfaces for both $\theta=0^\circ$ and 60° is associated with reduction in surface free energy due to amorphization of Si surface by ion irradiation. Increasing nature of δ with fluence at $\theta=0^\circ$ is understood as due to the presence of Ar atoms at the top surface of irradiated Si, instead of variation in surface roughness. Wettability of Si surface irradiated at $\theta=60^\circ$, follows the same trend as that of $\theta=0^\circ$ until the onset of ripple formation. However, once the ripple patterns are formed on the surface, introducing surface anisotropy, the hydrophobicity of Si surface is found to decrease with fluence in the direction perpendicular to the ripple wave-vector, while it remains constant in the direction parallel to the same. A decrease in hydrophobicity is presumable due to the observed inhomogeneity in Ar atom distribution over the ripple patterned top surface. However, constant δ with fluence in a direction parallel to the ripple wave-vector suggests that the effect of pinning the drop boundary at the rippled interface may also be active in determining the contact angle.

Bibliography

1. T. Makris, K. Tsevas, L. Kadylis, L. Mprechas, and E. Skuras, *J. Sol. Energy* 135 (2013) 034503.
2. Y. Inomata, K. Fukui, and K. Shirasawa, *Sol. Energy Mat. Sol. C.* 48 (1997) 237.
3. A.M. Bowen, M.J. Motala, J.M. Lucas, S. Gupta, A.J. Baca, A. Mihi, A.P. Alivisatos, P.V. Braun, and R.G. Nuzzo, *Adv. Funct. Mater.* 22 (2012) 2927.
4. Y.C. Tseng, A.U. Mane, J.W. Elam, and S.B. Darling, *Adv. Mater.* 24 (2012) 2608.
5. P. Campbell and M.A. Green, *J. Appl. Phys.* 62 (1987) 243.
6. W. Barthlott and C. Neinhuis, *Planta* 202 (1997) 1.
7. H. Gau, S. Herminghaus, P. Lenz, and R. Lipowsky, *Science* 283 (1999) 46.
8. M.T. Spuller and D.W. Hess, *J. Electrochem. Soc.* 150 (2003) G476.
9. R. Blossey, *Nature materials* 2 (2003) 301.
10. P.-G. De Gennes, *Rev. Mod. Phys.* 57 (1985) 827.
11. R.N. Wenzel, *Industrial & Engineering Chemistry* 28 (1936) 988.
12. P.R. Pandey and S. Roy, *J. Phys. Chem. Lett.* 4 (2013) 3692.
13. T. Kumar, U.B. Singh, M. Kumar, S. Ojha, and D. Kanjilal, *Curr. Appl. Phys.* 14 (2014) 312.
14. B. Bhushan and Y. Chae Jung, *Ultramicroscopy* 107 (2007) 1033.
15. A. Metya, D. Ghose, and N.R. Ray, *Appl. Surf. Sci.* 293 (2014) 18.
16. B.S. Kim, S. Shin, S.J. Shin, K.M. Kim, and H.H. Cho, *Nanoscale Res. Lett.* 6 (2011) 1.
17. L. Cao, T.P. Price, M. Weiss, and D. Gao, *Langmuir* 24 (2008) 1640.
18. T. Young, *Philos. Trans. R. Soc. London* 95 (1805) 65.
19. A. Zdyb, J. Olchowik, and M. Mucha, *Mater. Sci.* 24 (2006) 1109.
20. S. Hara, S. Izumi, T. Kumagai, and S. Sakai, *Surf Sci.* 585 (2005) 17.

21. W. Möller and W. Eckstein, Nucl. Instrum. Methods Phys. Res. B 2 (1984) 814.
22. R. Cox, J. Fluid Mech. 131 (1983) 1.
23. J.Y. Chung, J.P. Youngblood, and C.M. Stafford, Soft Matter 3 (2007) 1163.

CHAPTER 8

8 Summary and future scope

In summary, we have carried out extensive experimental investigations on the evolution of self-organized nanoscale periodic patterns on silicon surface during medium energy ion irradiation, related structural and compositional modifications of the samples, and ion-fluence-dependent wettability of irradiated surfaces, which may have useful applications in electronic, optoelectronic, magnetic or biochemical devices as well as in solar cells.

In this thesis, in the introduction, we have outlined the field of ion-solid interaction and the scope of the process in synthesis and modification of materials, with a special emphasis on ion-beam induced spontaneous evolution of periodic surface nanopatterns, as pertinent to this thesis. The experimental techniques used to perform the studies presented in this thesis were described. Subsequently, the statistical methods of characterization of surfaces were briefly introduced and the theoretical models of ion-induced surface evolution were outlined.

Our in-depth study reveals hitherto unobserved aspects of medium energy ion-beam induced pattern evolution. In particular, we detected a decreasing trend in ripple wavelength with ion fluence in the initial stage of morphological evolution for 60 keV argon ion irradiation on silicon at room temperature. Numerical simulations of the continuum model of ion-sputtered surfaces suggest that this behavior is due to the relaxation of the surface features of the experimental pristine surface during the initial stages of the pattern formation. The observation of this hitherto unobserved behavior of the ripple wavelength seems to have been enabled by the use of medium energy ions, for which ripple wavelengths are order(s) of magnitude larger than at lower ion energies. We have also shown a coarsening of ripple wavelength which follows in the later stage of ripple evolution. Our experiments further

demonstrated formation of ripple patterns from angle of incidence $\theta = 45^\circ$, indicating 45° to be the critical angle for pattern formation. We carried out statistical analyses of the surface morphologies and clearly distinguished linear and nonlinear regimes of the observed ripple patterns. In doing so, we have been able to point out that the decrease in ripple wavelength is a phenomenon that takes place in the linear regime. From our experimental results and those available in the literature, we have created a parametric phase diagram which summarizes an overview of pattern formation on silicon surface under medium energy ion irradiation. On the basis of this phase diagram, we have shown some striking similarities between ripple patterns in low and medium energy regimes in order to make an attempt to understand whether similar mechanisms are responsible for pattern formation in both the regimes. A comparison of the experimental results (in the linear regime) with our theoretical estimations shows that in contrast to the dominance of ion-induced atomic redistribution process in case of low energy ion-induced ripple evolution on Si), both curvature-dependent sputter erosion and atomic redistribution are operative for medium energy ion-induced ripple evolution.

From our structural analysis of ripple patterned Si surfaces, we confirmed the amorphization of the top layer and showed that the thickness of this amorphous layer decreases with ion angle of incidence. Compositional analysis revealed retention of argon atoms in the near-surface region of the top amorphous layer. We have also found that dimension of the ripples depends on the thickness of the amorphous layer. We have demonstrated that the experimentally observed scaling of thickness of the amorphous layer can be qualitatively understood by assuming that the nuclear energy loss of incident ions is the predominant process behind amorphization, instead of the total energy of the ions. Based on the experimental finding of energy dependence of ripple wavelength, we have shown that the pattern induced in Silicon by medium energy Argon ions is driven by the nuclear energy loss instead of total ion energy.

Within the range of our experimental parameters, we have also have also characterized the patterned surface in terms of areal ratio, ripple directionality, and aspect ratio through the statistical parameters extracted from AFM images of the patterned surfaces. Statistical analyses of morphological parameters show that ripples which are most directional and of dominant structures, having larger interface area, develop for the angle of incidence $\theta=75^\circ$. While interfacial area of the textured surface is improved towards higher fluences viz. 8×10^{18} ions cm^{-2} at $\theta=60^\circ$. Further, the ordering of the ripple patterns increases with ion fluence and incident angle. Moreover, the roughness exponent values of ion induced ripple patterned surfaces are found to belong to two universality classes of scaling of pattern, where the transition from one to another occurs with increase in ion fluence.

Regarding the physiochemical properties of argon irradiated patterned silicon surfaces, we have shown that a transition from hydrophilic to hydrophobic surface taken place due to irradiation. This has been primarily understood as due to a reduction in surface free energy with amorphization of crystalline silicon. Also, the presence of argon atoms in the top layer is seen to influence the hydrophobicity, especially for normally irradiated silicon surfaces. Further, the anisotropic nature of ripple patterns also introduces the anisotropy in contact angle, measured in two directions, viz. parallel and perpendicular to the ripple wave-vector.

Thus, a comprehensive study of medium energy ion-induced ripple pattern evolution on silicon surface and their prospective application have been presented in this thesis. The physical processes leading to ripple formation have also been pointed out. Based on our results, further experimental investigations can be taken up which will lead to a much deeper understanding of this self-organized patterning process, needed for optimization of features for particular applications. For instance, the pattern formation for angle of incidence $\theta > 75^\circ$ needs to be checked which will help to understand the contribution of sputtering in ripple formation in greater detail. It is also imperative to carry out medium energy ion irradiation on

materials other than silicon, for instance on germanium, to obtain a general understanding of ion-induced pattern formation in the medium energy regime. It is also important to elucidate the relevance of recently proposed solid flow model in understanding the pattern formation mechanism. From the structural point of view, the difference in the thickness of the amorphous layer between the two slopes of the ripples along with the presence of the cavities/voids in the ion-beam-facing side of the ripple slope offers a possibility of decorating it with metal particles having unique electronic, optoelectronic, or magnetic properties. Statistical analysis of ripple patterns, as described in this thesis, will help to develop patterned surfaces for particular applications by varying the fluence and angle of incidence. A strong effect of morphology on wetting property of the surface has been found in our experiment. Thus, there is a room to study the morphological parameters at higher fluences and subsequently tune the wettability of patterned surfaces.